Study on Tidal Current Distribution in the Bali Strait Using Coastal Acoustic Tomography

(沿岸音響トモグラフィーを用いたバリ海峡の潮流分布に関する研究)

学位取得年月 **2021年09月**

ARUNI DINAN HANIFA

ABSTRACT

On March 4th, 2016, KMP. Rafelia 2, a ferry boat that operated as a sea-transportation between Ketapang Port (Java Island) and Gilimanuk Port (Bali Island), was tilted and sinking before arrived at Ketapang Port from Gilimanuk port. This accident made the Indonesian government want to study tidal current distribution in the Bali Strait to prevent another accident. The ferry route of the Bali Strait is categorized as a heavy shipping traffic area. The conventional current measurement, such as shipboard ADCP, moored ADCP, and many other acoustic technologies, are not supported and prohibited by many countries from measuring ocean properties around heavy shipping traffic areas. Coastal acoustic tomography (CAT) is proposed to apply OAT technology in shallow water and coastal seas. CAT is an observational method suited to use in the Bali Strait with strong and highly variable currents.

A CAT experiment was conducted around the ferry route at the northern part of the Bali Strait during June 1-3, 2016 in local time 8 hours ahead of UTC. Four land-based CAT systems (S1, S3, S5, S7) were deployed on both sides of the strait. One-minute interval data resampled at 10-min interval data were decomposed into two period-ranges, > 6h using a 6-hour low pas filter (LPF) to retrieve M2-tide which has 12-h period, and 10min-6h using a 10min-6h band pass filter (BPF). The range-average current results for every transmission line showed the characteristic of a tidal wave in Bali Strait is mix semidiurnal tides. The M2 and M8 oscillations peaked at the low water of SSH data and diminished around the high water. And the phase relation between SSH and current showed that potential energy from SSH variation served to generate not only M2 current, but also M8 current. Furthermore, the M8 oscillation is embedded in the envelope oscillation of the semidiurnal period. It provides a big possibility that the nonlinear interaction of semidiurnal and diurnal tides generated the M8 oscillation. However, the reason why the M8 component rather than M3, M4, and M6 was dominated is not found yet. The strong and highly variable 3-h oscillation, which occurs in the northern part of the Bali Strait and causes problems with ferry operation, was measured for the first time using a CAT array.

The spatiotemporal tidal current fields were reconstructed by the inverse method of CAT data. The accuracy of the spatiotemporal current fields, based on RMSD between the observed RACs and the inverted RACs is 40% underestimation. The results showed the characteristic of strong current in the tomography site is dominant by the northward current for both bands. The clockwise and counter-clockwise vortex were formed at the lateral side of Java Island, while the central current strong.

The more comprehensive inverse method of CAT that could be done for further works is three-dimensional inversion. This inversion is combining horizontal-slice inversion with vertical-slice inversion and the result could explain the generation of the 3-hour oscillation in the tomography domain better. The following future work is data assimilation using the ensemble Kalman Filter method. This method could do forecasting the tidal current distribution in the ferry route of the Bali Strait. This forecasting model is useful for better ferry routes and schedules to avoid the disastrous current.

CONTENTS

LIST OF FIGURES

LIST OF TABLES

CHAPTER 1 INTRODUCTION

1.1 Oceanographic Measurement

The ocean is vast, nonlinear, turbulent, and inaccessible to electromagnetic radiation. The movement of oceanic waters has consequences for a confounding variety of applications such as climate change, biological productivity, sea-level change, weather forecasting, fisheries prosperity, the chemical history of the earth, the dynamics of the earth-moon system, the movement of pollutants, sea transportation, aquacultures, and so forth [1, 2]. For these reasons, oceanographic measurement is most needed and rapidly changing to prevent the worst effect for humanity [3].

The oceanographic measurement and the exploration of the sea can be divided arbitrarily into various eras [4]. Those are the era of surface oceanography (until 1873); deep-sea exploration (1873-1914), the era of national systematic surveys (1925-1940), new methods era (1947-1956), the era of International Cooperation (1957-1978), satellite era (1978-1995), and the era of earth system science (1995~) [5]. The latest era is characterized by global studies of the interaction of biological, chemical, and physical processes in the ocean and atmosphere and on land using in-situ (measurement in the water) and space data in numerical models [5].

In situ observations of the ocean are hard and rather expansive, especially observations on circulation and currents [3]. Measurement of ocean current is fundamental to a general understanding of the ocean [6]. Ocean circulation transports heat and affects climate and weather. Ocean currents transport marine life and sediments, which affect the passage of ships and also the oceanographic instruments themselves.

There are different basic ways of measuring a current, these are:

1. A moored current meter (as shown in **Fig. 1.1**) in the sea produces speed and direction measurements at fixed time intervals.

2. The current meter attached to a moving platform such as a ship and measure the relative current. The absolute current is then determined by such a vector subtracting the motion of the ships over the ground determined by navigation. This method is used with the Acoustic Doppler Current Profiler (ADCP). An ADCP may also be moored at a fixed location on the sea-bed (as shown in **Fig. 1.2**).

3. Let an object flow or float with the current and observe its motion i.e the change of position at fixed time intervals. For example, a drifting buoy (as shown in **Fig. 1.3**).

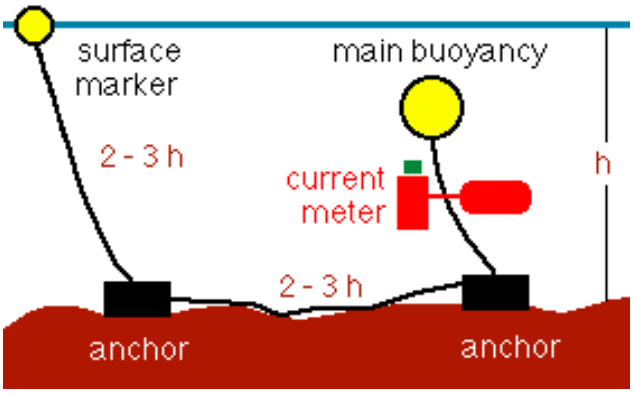

Fig. 1.1 A moored current meter [7]

Fig. 1.2 Acoustic doppler current profiles (ADCPs) [7]

Fig. 1.3 A drifting buoy [8]

The moorings, ADCP, and buoys are suitable for current measurements around offshore areas [3]. The moorings are subject to heavy loads by ocean currents and waves and interference by commercial shipping and fishing activities, and hence losses of instruments and data are quite common. The rotors are also subject to biofouling by

marine organisms such as barnacles. Long-term observations, therefore, require frequent redeployments. It is particularly difficult to make measurements in the upper 30 m or so, not only because of the interference and biofouling but also because of the possibility of contamination by surface waves. In a surface wave field, the vertical motion of the mooring or rotor-pumping of Savonious rotor-type instruments leads to an erroneous overestimation of currents.

1.2 Ocean Acoustic Tomography

Ocean acoustic tomography (OAT) was introduced by Walter Munk and Carl Wunsch in 1979. The tomographic method initially used in seismological [9] and medical problems was applied in the ocean to measure precise travel time or other acoustic propagation properties and the state of the sea traversed by the sound speed field [10]. As the acoustic parameters are the function of ocean properties, OAT could provide information about the intervening ocean by using an inverse method. Moreover, OAT signals could be transmitted over distances of many thousands of kilometers at the low-frequency sound [10, 11].

The first OAT experiment was a direct response to the demonstration in the 1970s that about 99% of the kinetic energy of the ocean circulation is associated with features in a mesoscale [10, 11]. The result of the experiment was a temperature map of mesoscale eddies with 100-300 km scales, which confined from the Gulf Stream and drifted to the Bermuda Sea, as shown in **Fig. 1.4** [12]. The thermal structures of mesoscale eddies were reconstructed by the inverse analysis of one-way travel time data between the arrayed sources to receivers. It was validated and showed great consistent results using

conductivity-temperature-depth (CTD) and airborne expendable bathythermograph (AXBT) data [12].

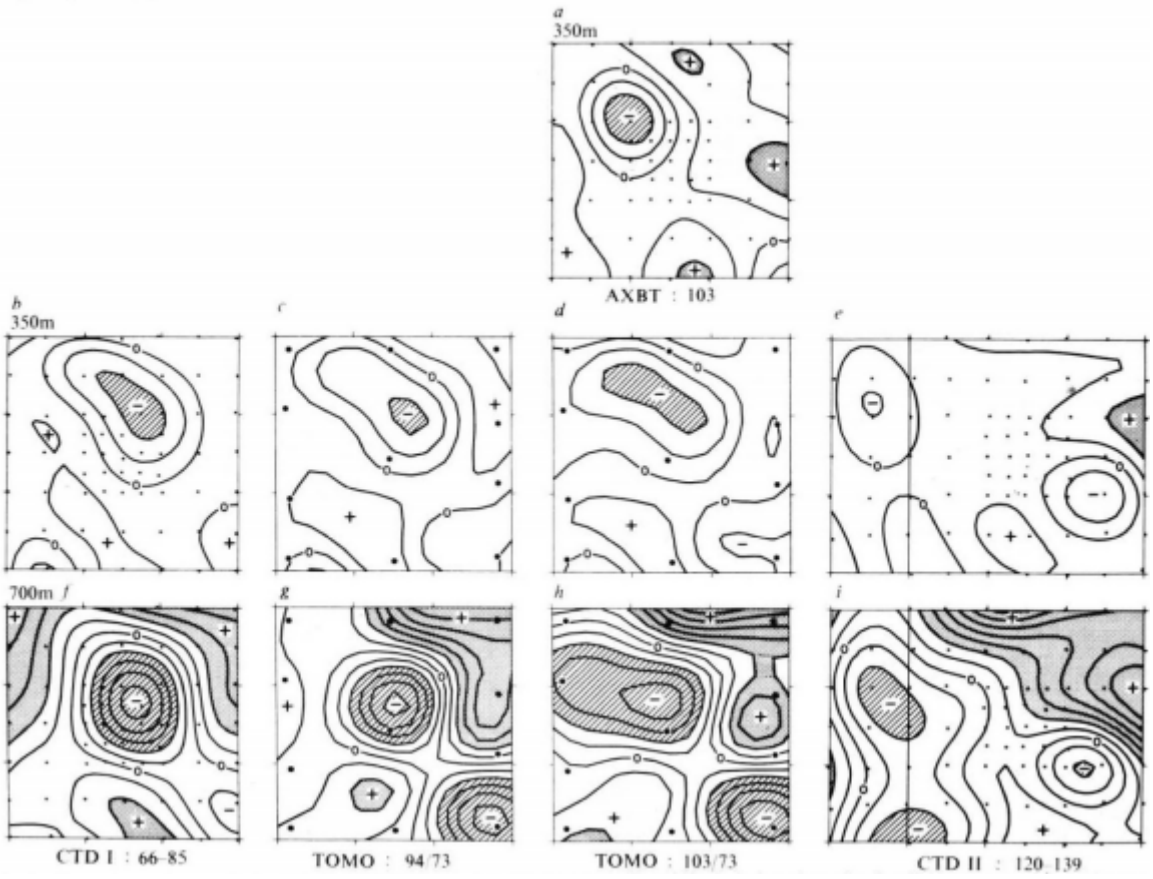

Fig. 1.4 Mesoscale eddies from OAT, CTD, and AXBT [12]

Several intensive OAT experiments were succeeded in the North Atlantic Ocean and the Mediterranean Sea in collaboration of the US and European OAT groups [13]. However, due to high instrumentation cost, the OAT studies was remarkably weakened in the oceanographic community. After a long vacuum period, a deep-sea OAT experiment was conducted in the Fram Strait [14, 15, 16] and Canary Basin [17]. The experiment targeted long-term monitoring of strait throughflow for the warming phenomenon in the Arctic Sea and tracking of meddies wandering the North Atlantic

Ocean around the exit of the Mediterranean Sea (the Gibraltar Sea). At the end, compared to the ADCP moorings, argo floats, high-frequency ocean radars, and inverted echo sounders, OAT could not reach a good operational phase [13]. Improvement of the tomographic instrument is needed to reduce the instrumentation cost.

1.3 Coastal Acoustic Tomography

1.3.1 Importance of CAT Technology in the Oceanographic Problems

Coastal Acoustic Tomography (CAT) is proposed to apply OAT technology in the shallow water and coastal seas. With the reduction of instrumentation cost and more compactness system, making onboard-easy handling system is the advantages of the CAT system design [13], as you could see in **Fig 1.5**.

As well as OAT, CAT technology has several advantages. First, the travel time and other measurable acoustic parameters are functions of oceanographic interest, and the information about the intervening ocean can be interpreted using inverse methods. Second, signals can be transmitted over many kilometers as the virtue of the ocean [13]. Moreover, simultaneous mapping (snapshot) of time-varying subsurface structures of current velocity and sound speed (mainly temperature) with a speed of about 1.5 kms^{-1} using underwater sound could be made using OAT technology. Using multi-acoustic stations that surrounded the observation domain, each station has pair to perform reciprocal transmission (**Fig. 1.6**). Travel time data will be acquired along acoustic ray paths of the reciprocal transmission and converted to path-average current velocity and sound speed through the sound speed empiric standard equations. The accuracy is remarkably improved through a path-integral along the ray. And in comparison with one-point sensors such as current meters and the profiling data by ADCP, it is well understood [13].

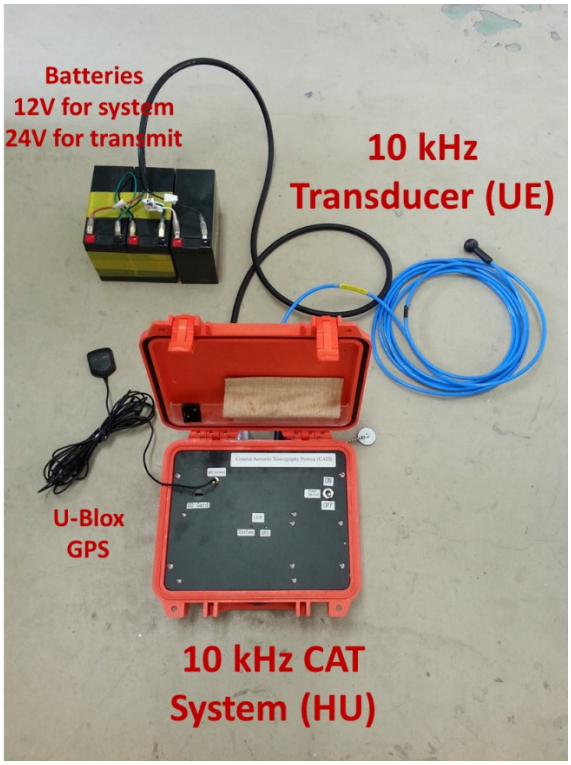

Fig. 1.5 The CAT system land-based design

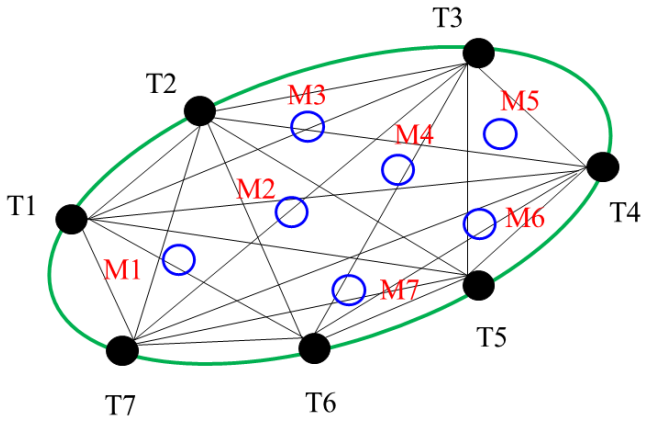

Fig. 1.6 Sketch of the CAT array composed of seven acoustic stations and CTDs [13]

The CAT fundamental is a reciprocal sound transmission composed of two stations located on the opposite sides of the coastal channel to be measured [18], as shown in **Fig. 1.7**. A global positioning system (GPS) is installed in the CAT system makes a correct reconstructed current velocity by synchronizing the clock of multi-acoustic stations with GPS clock signals. Furthermore, the GPS also provides the positioning of stations. However, the positioning accuracy about 10 m, was insufficient for mapping the accurate temperature fields owing to the limited distances of sound transmission. The combination of the travel time data from CAT with sound speed determined from one-point CTD lying between acoustic pairs improved the positioning accuracy [13]. The accuracy of CAT data has already been well validated in comparison to ADCP and CTD data which were attempted in coastal seas around Japan [19, 20, 21], China [22], and Indonesia seas [23, 24, 25].

Heavy fishing activities and shipping traffic generally occur in the coastal seas. Environmental monitoring demands of the coastal seas with intense fish resources, especially around East Asian countries, face severe difficulties. The other technologies, such as shipboard ADCP, moored ADCP, and many other acoustic technologies, are not supported and prohibited by many countries from measuring ocean properties around heavy marine activities. CAT technology is an optimum method to observe and measure continuously tidal currents and other ocean properties around ports, bays, straits, and inland seas without disturbing shipping activities, ferry boat transportation, fisheries activities, or marine aquaculture industries [26, 27]. In comparison to OAT technology which requires heavy, expensive instrumentation to measure a mesoscale to a largescale oceanographic problem with scales 100-1000 km in open-deep seas, CAT can be executed on a small boat and easy handling instrumentations encourage operation by a number of coastal-sea researchers,

engineers and environmentalists, supported by common-sized funds [13]. Various coastal-sea phenomena such as coastal currents, tidal currents, tidal vortices, residual currents, estuary circulation, port/harbor circulation, and onshore-offshore water exchange, inner-outer bay water exchange, frontal circulation, coastal upwelling, coastal jets, the spreading of river plume and so on are targets of mapping by CAT.

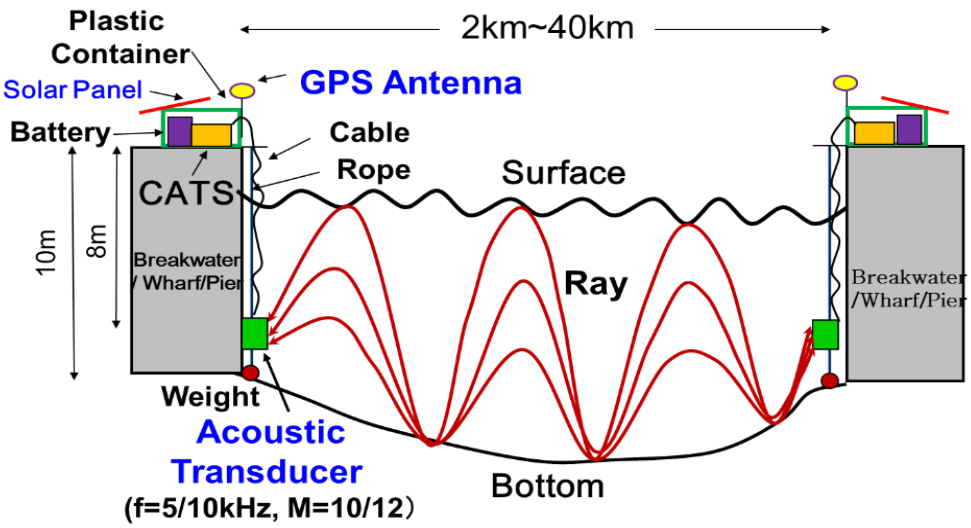

Fig. 1.7 CAT design in the vertical section between two acoustic stations [28]

The simultaneous mapping of time-varying currents in the coastal seas is difficult for shipboard observation because of the rapidly varying deformation of current fields during the shipboard survey. The repeat ADCP survey synchronized with tidal phases sometimes makes it possible to measure residual current. However, a simultaneous mapping (snapshot) of vortex-embedded current fields is too difficult to be performed by a shipboard survey. CAT may be a unique technology for mapping coastal-sea environments varying rapidly with time. Real-time monitoring of coastal sea environments is realized by multi-station CAT arrays located at the periphery of

bays, ports, or any other artificial coastal construction and data telemetry using a mobile phone network (**Fig. 1.8**). The present state of coastal-sea environments is measured by CAT array and the real-time data are broadcasted to public society. Predicting coastal sea environment variations is possible by assimilating tomography data into a coastal sea circulation model as done in daily weather prediction by radar [13].

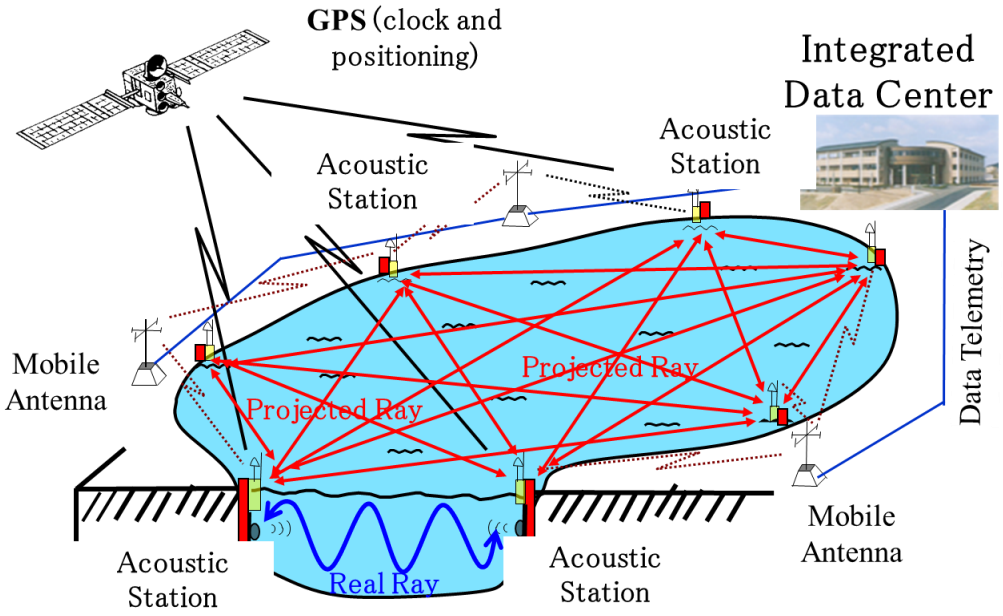

Fig. 1.8 Multi-station CAT arrays distributed at the periphery of a bay [13]

1.3.2 The difficulty of CAT Application to the Coastal Seas

Although the CAT technology is more costless and compact systems than OAT technology, because of the application of CAT to the coastal seas, which most is shallow water, the observation range (distance-to-distance) was restricted up to 50 km by multi reflections of transmission sound at the surface and seafloor. The ambiguity of bottom topography may be a factor in producing biases in the reconstructed current

velocity and sound speed structures. The restricted observation range could be handled by using artificial coastal constructions as a temporal platform to set the CAT system. Artificial coastal constructions such as wharves, piers, jetties, pontoons, and breakwaters have been helpful as a temporal platform to set the CAT system. Especially in Japanese coastal seas where moored observation is strictly prohibited by fisheries activity and shipping traffic, those kinds of constructions made to set CAT system possible (**Fig. 1.9**). An array of anchored boats surrounding a tomography domain has also been used as a short-term platform suitable in the coastal seas around China due to less expensive rental charges. Attractive experiments were carried out with station numbers of four to eleven in the Nekoseto Strait, Tokyo Bay, the Kanmon Strait and Hiroshima Bay of Japan, Zhitouyang Bay, Qiongzhou Strait, Sanmen Bay and Darien Bay of China, and the Bali Strait and Lombok Strait of Indonesia. Especially, the Darien Bay experiment in March 2015 was carried out with 11 CAT stations and detailed structures of tidal current and residual current were reconstructed by the standard inverse method. Application to the terrestrial waters was also attempted using higher frequency sound up to 50 kHz [29].

Fig. 1.9 The CAT system set on a pier

1.4 Previous Research

1.4.1 Tide and Tidal Current in the Bali Strait using a COHERENS

In 2010, by using a Coupled Hydrodynamical-Ecological Model for Regional and Shelf Seas (COHERENS), a tide and tidal current model of the Bali Strait was produced as mentioned in Berlianty and Yanagi (2011) [30]. This model was verified using a point measurement of ADCP at Bangsring port (shown as a triangle point in **Fig. 1.10**) and a tide-gauge observation at Pengambengan port (shown as a rectangle point in **Fig. 1.10**).

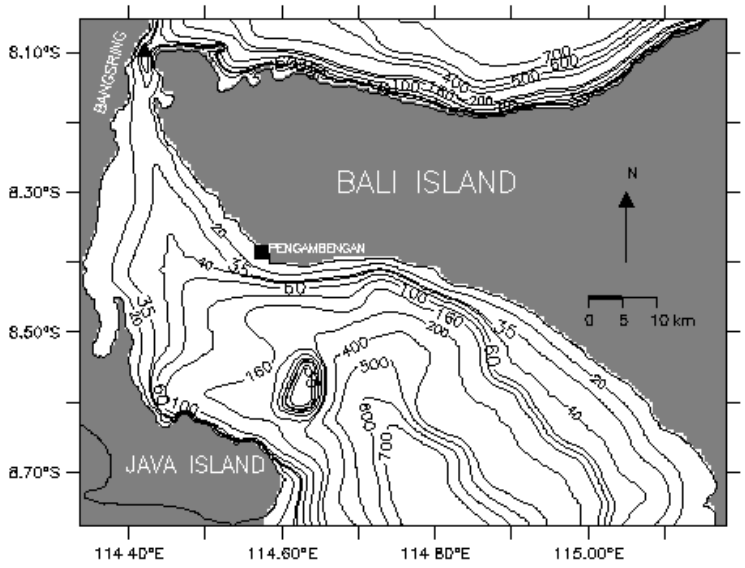

Fig. 1.10 Bathymetry map of Bali Strait [30]

The COHERENS modeled tide and tidal current for spring tide and neap tide of May 2010. The maximum velocity of 2 ms^{-1} tidal currents was found when spring tide at a maximum flood at high water flows northward (as shown in **Fig. 1.11a**). During maximum ebb, the current flows to the south with velocity about 0.5 ms^{-1}. Meanwhile in the neap condition, the maximum velocity of 1.5 ms^{-1} tidal currents was found during maximum ebb at low water flows southward (as shown in **Fig. 1.12c**). During the maximum flood, the current flows to the north with velocity about 0.7 ms^{-1}.

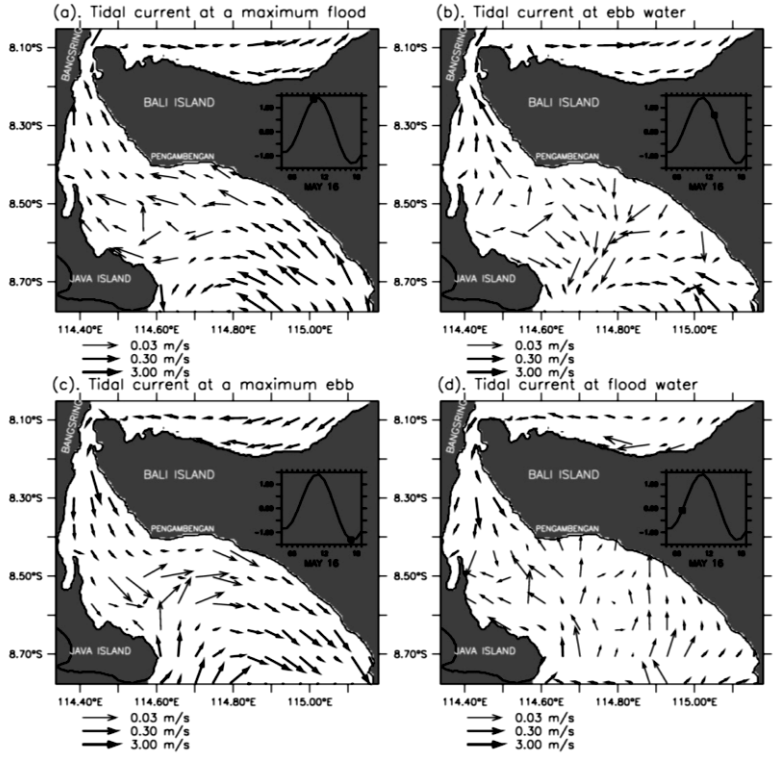

Fig. 1.11 Tidal current at the spring tide (May 16th, 2010) [30]

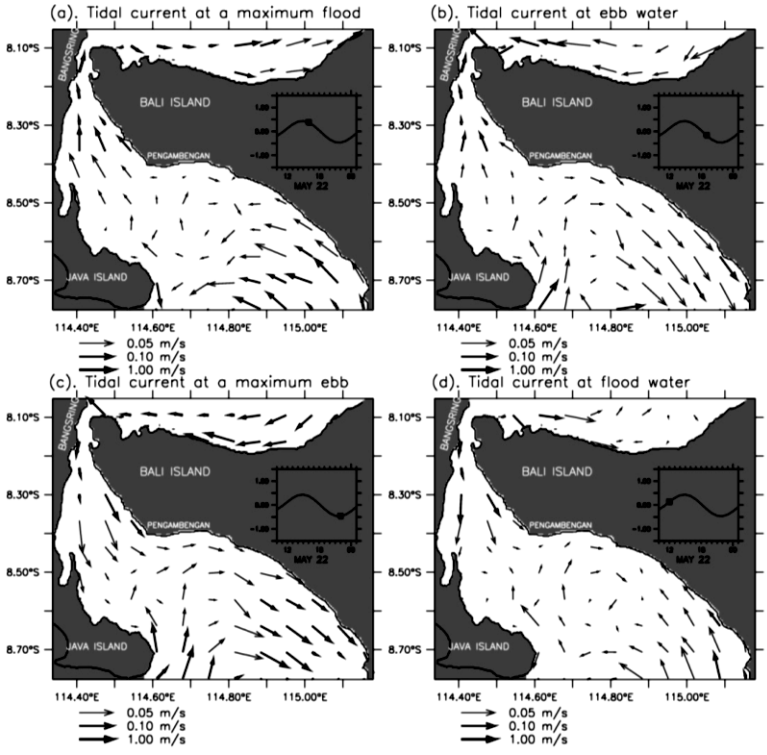

Fig. 1.12 Tidal current at the neap tide (May 22th, 2010) [30]

The time-series of surface elevation obtained from ORITIDE [31, 32] was verified using Pangembangan tide-gauge station for the period of May 1st to May 31st, 2010, as shown in **Fig. 1.13**. The root mean square error (RMSE) was 0.29 m, and the root-squares (r^2) is 0.813. Those values indicated that the model absolute fit with the data points.

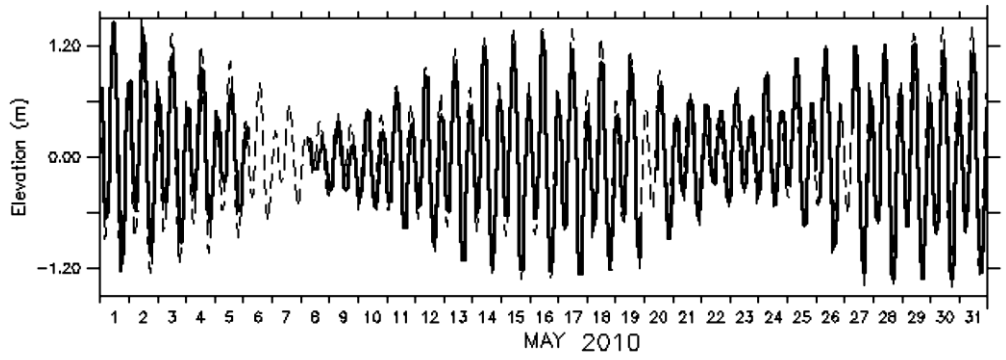

Fig. 1.13 Verification of surface elevation between ORITIDE (dash line) and observation (solid line) [30]

The current velocities from COHERENS were verified using ADCP measurement at Bangsring station for the period of February 18th to 19th, 2010. The current velocities were divided into two components, north and east components. COHERENS results showed a little larger velocities than the ADCP (as shown in **Fig 1.14**). Furthermore, there was a 3-h phase lag between the elevation and current velocities. It was explained in Yanagi (1999) that the 3-h phase lag indicated that tidal wave in the narrow passage of the Bali Strait is a standing wave type [33]. This current direction goes north-eastward at ebb tide and south-westward at flood tide.

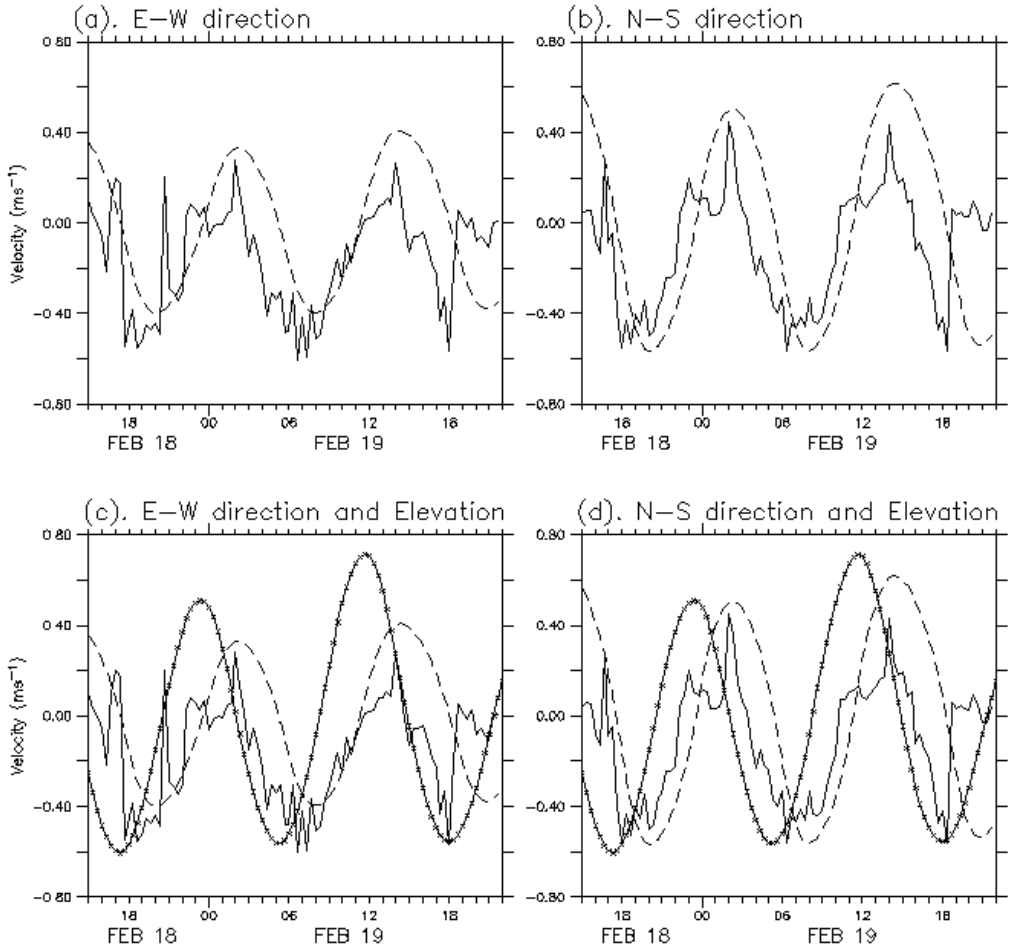

Fig. 1.14 East-west and north-south current direction of COHERENS (dash line) and ADCP (solid line) and sea surface elevation from Pengambengan tide-gauge station (point full line) [30]

1.4.2 Vertical profile of Tidal Current in the Bali Strait from Inverse Method of CAT

A tomography experiment was carried out in the Bali Strait from June 10-13, 2015, in Syamsudin *et al.* (2017) [25]. The tomography domain is in the northern part of the Bali Strait with channel widths of about 5 km which characterized by a strong tidal current (as shown in **Fig. 1.15**). The experiment purposes are measured in the range-averaged current and temperature vertical section structures at a 3 min interval.

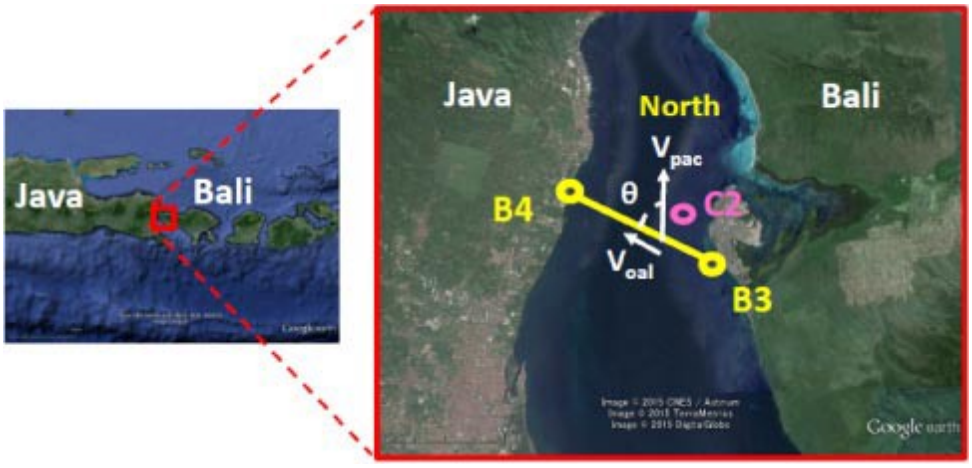

Fig. 1.15 The observation site and experiment design [25]

The B3 station sited at an abandoned platform of a natural gas pipeline, about 60 m offshore from the coast. While the B4 station placed at the edge of a jetty in a resort hotel. The distances between both station was 4,461 m which determined by GPS and CTD. A SonTek-CastAway sensor was used to record the temperature at C2 point (as shown in **Fig. 1.15**). The RMSE of current velocity was 0.106 ms^{-1}, for sound speed was 0.108 ms^{-1}, and for temperature was 0.046 ^{o}C. Those RMSE were in rough agreement with the one-digit error.

The results from the inverse method were five-layer structures of the hourly-mean current (as shown in **Fig. 1.16**). The hourly-mean current showed the generation of nonlinear internal tides with amplitudes of 1.0–1.5 ms^{-1} and periods of 6 h superimposed on semi-diurnal internal tides with amplitudes decreasing from the upper to lower layer. The current variations showed an out-of-phase relation between the upper and lower layers while the temperature data varied in-phase for all five layers.

The power spectral density showed the energy of 6-hours period is the second biggest energy after energy of 12-hours period (as shown in **Fig. 1.17**). Furthermore, the 3-h

energy is bigger than the 6-h energy in the lower layer (V1 and V2) as represented by green arrows in **Fig. 1.17**. Further study is required to expound on the nonlinear tide mechanism [25].

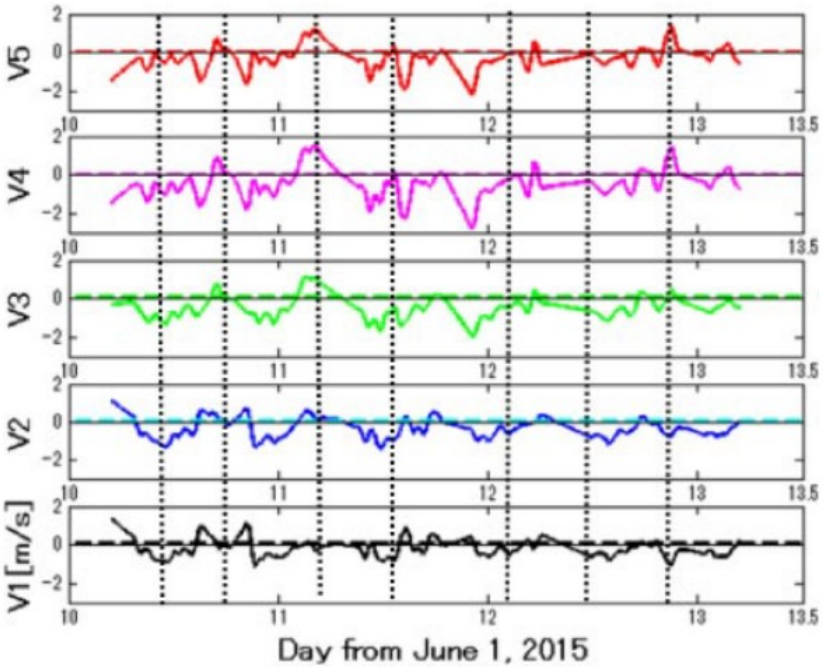

Fig. 1.16 Five-layer structures hourly-mean current [25]

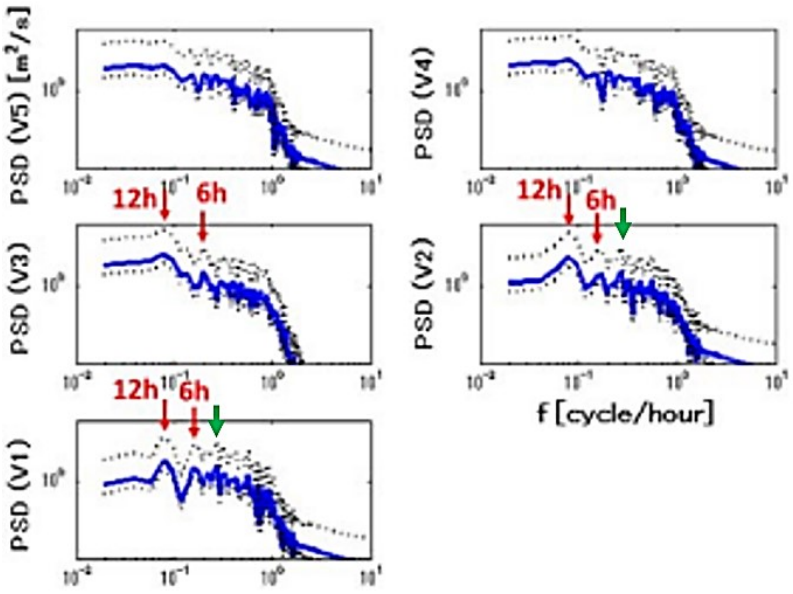

Fig. 1.17 Power Spectral Density of tomography experiment in Bali Strait 2015 [25]

1.5 Aim and Objectives

On March 4th, 2016, KMP. Rafelia 2, a ferry boat that operated as a sea-transportation between Ketapang Port (Java Island) and Gilimanuk Port (Bali Island), was tilted and sinking before arrived at Ketapang Port from Gilimanuk port [34]. The chronology of this accident started when the ferry boat sailed from the Gilimanuk Port with a speed around 6.5 knots or 3.3 $ms^{-1,}$ and the prow direction is 300 degrees (shown in **Fig. 1.18**). Only in 7 minutes after, the ferry boat already at the center of the strait. But the prow direction changed to 315 degrees (shown in **Fig. 1.19**), and the ferry boat crew realized that the ferry was tilted to the left. During those time, the ocean current direction flowed from north to south. It was the opposite with the ferry boat direction. The first cause of this accident was overcapacity. But, the strong current made the tilting process and water intrusion faster. This ferry boat sunk near the Ketapang port (shown in **Fig. 1.18**) and caused six people dead. Additionally, the newest accident has happened on June 29th, 2021. A ferry boat, KMP Yunicee, near Gilimanuk port, waited its turn to anchor the boat, suddenly hit by a strong current and drifted to the south. While it drifted, the ferry boat titled to the left, and only in 5 minutes, the ferry boat sunk. This accident caused seven people dead, and 11 people are missing [35].

It is important to observe and measure the tidal current distribution and its variation in the Bali Strait based on those events and accidents. As for the societal importance of predicting disastrous currents which probably occurred around the ferry route, the specific objectives of this study are focused on the followings:

1. Reconstruct vertical and horizontal tidal current distribution in the tomography domain.
2. Analyze and clarify the characteristics of the tidal current.

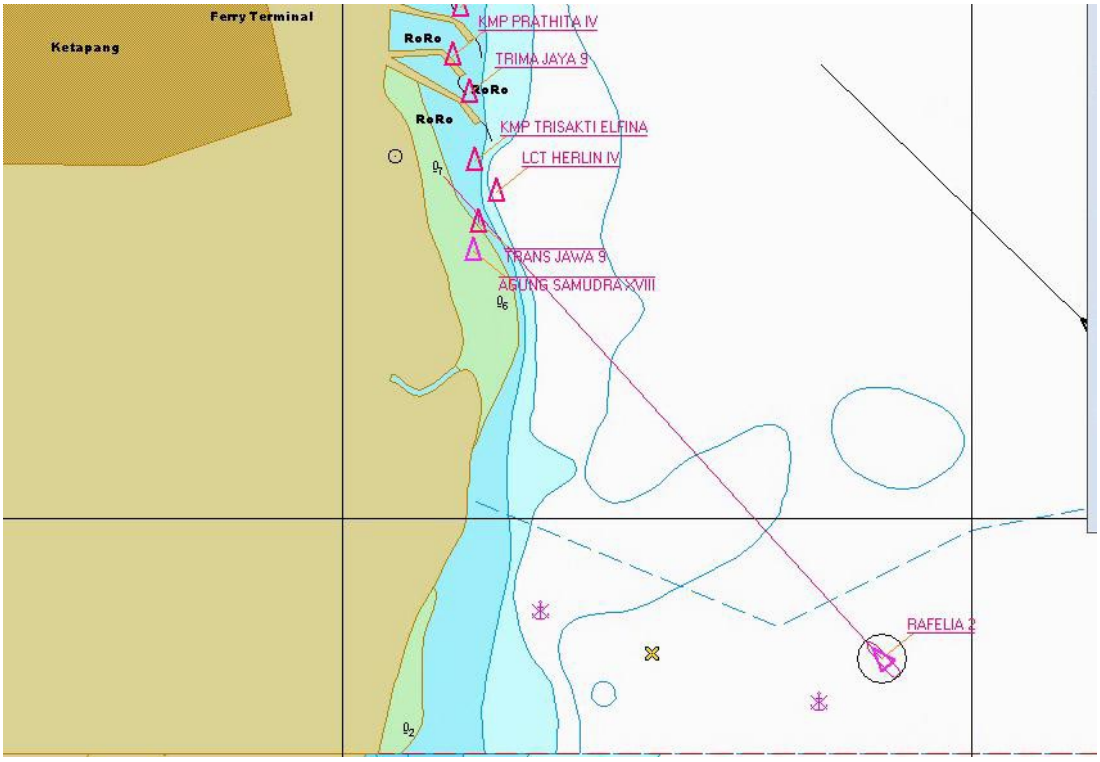

Fig. 1.18 The prow direction of KMP Rafelia 2 at initial condition [34]

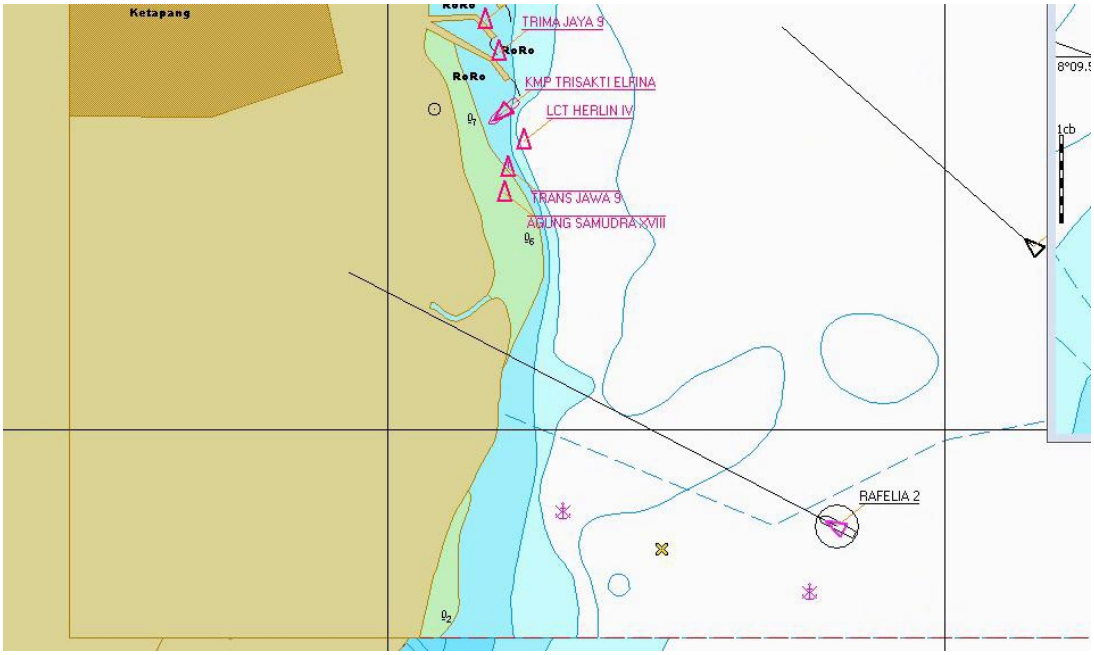

Fig. 1.19 The prow direction of KMP Rafelia 2 at the final moment before it sunk [34]

1.6 Structure of The Thesis

The thesis is structured as follows. Chapter 1 introduces and explains the oceanographic measurement for ocean current time by time, OAT preview, CAT background and its superiority over other conventional acoustic measurements. Some previous research related to the tidal current in the Bali Strait were explained. Hereafter, clarifies the objectives of the study and close this chapter by the structure of the thesis.

Chapter 2 explains how the methods and models that used in CAT to acquire the best results. Start from sound signals processing, how processed the sound signal raw data from the experiment. Next is the ray simulation used before the CAT experiment to estimate the best position and depth-deployment of the multi-acoustic stations. Therefore, after the experiment, travel times (time of flight) along the acoustic ray were obtained and processed into a range-averaged measurement. The range-averaged measurement is processed into horizontal profile by the inverse method. The horizontal-slice inversion was proposed to reconstruct ocean properties depth-averaged distribution on a horizontal plane in the experiment domain, such as tidal current distribution. Some errors are expected from station movements due to strong subsurface current, positioning acoustic station errors, and GPS clock errors. Henceforward, an error evaluation should be done for the validation by using CTD for positioning acoustic station correction and summation of travel time as for GPS clock correction.

In chapter 3, a CAT experiment was conducted at the northern part of Bali Strait in 2016. The experiment area is a very busy shipping route for the passanger ferry and logistic transportation. That area was the high priority concern of Indonesian government after a ferry sinking accident happened in 2015 due to strong and varying currents. An associated 3-h oscillation phenomenon was found by using range-averaged current method from CAT data measurement. Finally, it was suggested that the 3-h oscillation

is an internal seiche synchronized with the semidiurnal tides. These phenomenons were predicted as the cause of many ferry sinking accidents.

Thus, horizontal-slice inversions were done in chapter 4 to study more the tidal current distribution in the northern area of Bali Strait. The spatiotemporal current fields showed the maximum total current about two ms^{-1}. The north-south current is dominant and stronger than the east-west current, where the northward current is stronger than the southward current because of a strong influence of the Indian Ocean. Ocean current distribution formed a clockwise or counter-clockwise vortex on the Java side several times. Furthermore, several submarine cables exist at the bottom of the experiment site. Finally, all results and discussions are concluded in chapter 5, and the future works that should be taken are presented.

CHAPTER 2 METHODS AND MODELS

2.1 Signals Processing

2.1.1 Signal to Noise Ratio (SNR)

The wave pattern of the carrier modulated by M-sequence is formulated below (as shown in **Fig. 2.1**),

$$S(t) = M(t)\sin(\omega t) \qquad (2.1)$$

where M(t) is the wave pattern of the M-sequence and ω is the angular frequency of the carrier. For the CAT system, the phase of transmitting signals is coherently synchronized with GPS clock signals and thus, the CAT system is designed as a coherent sonar. The transmit signals are decayed with a damping rate of α through the underwater propagation and received at the time delay τ_0 by the counter station. By taking account of these two factors and ambient noise **n**, eq. (2.2) reduces the wave pattern for received data:

$$R(t) = \alpha M(t-\tau_0)\sin\{\omega(t-\tau_0)\} + n(t) \qquad (2.2)$$

To retrieve M-sequence signals alone from the received signal, the equation (2.2) is separated into two components, quadrature and in-phase. The resulting equations are composed of low and high-frequency components:

$$\hat{R}_{\mathrm{i}}(t) = \frac{1}{2}M(t-\tau_0)\cos(\omega\tau_0) - \frac{1}{2}M(t-\tau_0)\cos(2\omega t - \omega\tau_0) + n(t)\sin(\omega t) \qquad (2.3)$$

$$\hat{R}_{\mathrm{q}}(t) = \frac{1}{2}M(t-\tau_0)\sin(-\omega\tau_0) + \frac{1}{2}M(t-\tau_0)\sin(2\omega t - \omega\tau_0) + n(t)\cos(\omega t) \qquad (2.4)$$

The high-frequency components at the second and third terms on the right-hand side of equations (2.3) and (2.4) are removed through a low-pass filter (LPF). The

low-frequency component at the first term on the right-hand side, derived from the M-sequence signals, are retrieved through the LPF. The procedure of retrieving the M-sequence from received data is called complex demodulation and eq. (2.3) and (2.4) reduced become

$$R_{\mathrm{i}}(t) = \frac{1}{2} M(t-\tau_0)\cos(\omega\tau_0) \tag{2.5}$$

$$R_{\mathrm{q}}(t) = -\frac{1}{2} M(t-\tau_0)\sin(\omega\tau_0) \tag{2.6}$$

By taking a cross-correlation with one period of the M-sequence used in the transmission, eq. (2.5) and (2.6) becomes

$$C_{\mathrm{i}}[\tau] = \sum_k R_{\mathrm{i}}[t_k] M[t_k-\tau] = \sum_k \left\{ \frac{M[t_k-\tau_0]\cos(\omega\tau_0)}{2} \right\} M[t_k-\tau] \tag{2.7}$$

$$C_{\mathrm{q}}[\tau] = \sum_k R_{\mathrm{q}}[t_k] M[t_k-\tau] = \sum_k \left\{ -\frac{M[t_k-\tau_0]\sin(\omega\tau_0)}{2} \right\} M[t_k-\tau] \tag{2.8}$$

and the amplitude A_c and the phase Φ_c are calculated

$$A_{\mathrm{c}}[\tau] = \sqrt{C_{\mathrm{i}}[\tau]^2 + C_{\mathrm{q}}[\tau]^2} \tag{2.9}$$

$$\Phi_{\mathrm{c}}[\tau] = \tan^{-1}\left(\frac{C_{\mathrm{q}}[\tau]}{C_{\mathrm{i}}[\tau]} \right) \tag{2.10}$$

The amplitude A_c forms a steep peak at $\tau = \tau_0$, corresponding to a travel time because in the process of cross-correlation with M-sequence, ambient noises are remarkably diminished. In the coastal seas occupied with ship-derived noises, the precise measurement of travel time is impossible without taking the cross-correlation with M-sequence which is called a matched filter.

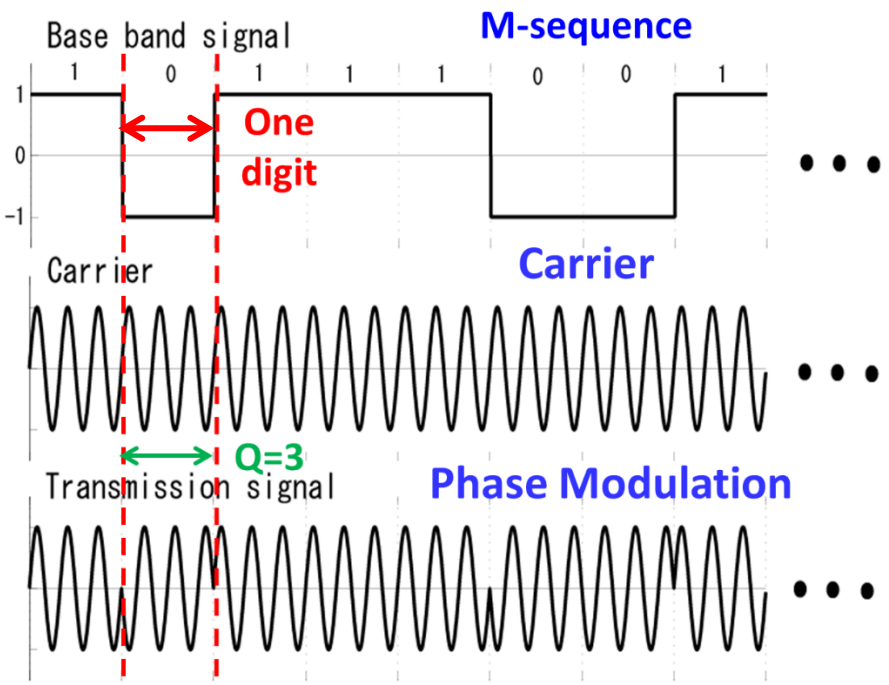

Fig. 2.1 Transmission signals using modulated M-sequences

Signal-to-noise ratios (SNRs) of the received data are primarily increased by the cross-correlation of received signals with the M-sequence used in the transmission (as shown in **Fig. 2.2**), obeying the following formula derived from central limit theorem in statistics:

$$\mathrm{SNR} = 20\log\sqrt{2^{\mathrm{M}} - 1} \qquad (2.11)$$

where M is the order of the M-sequence. Thus, SNR gains are 27.1 dB for M9, 30.1 dB for M10, 331. dB for M11 and 36.1 dB for M12. The M-sequence gain may surpass an increase of ambient-noise level caused by the broad frequency range of M-sequence.

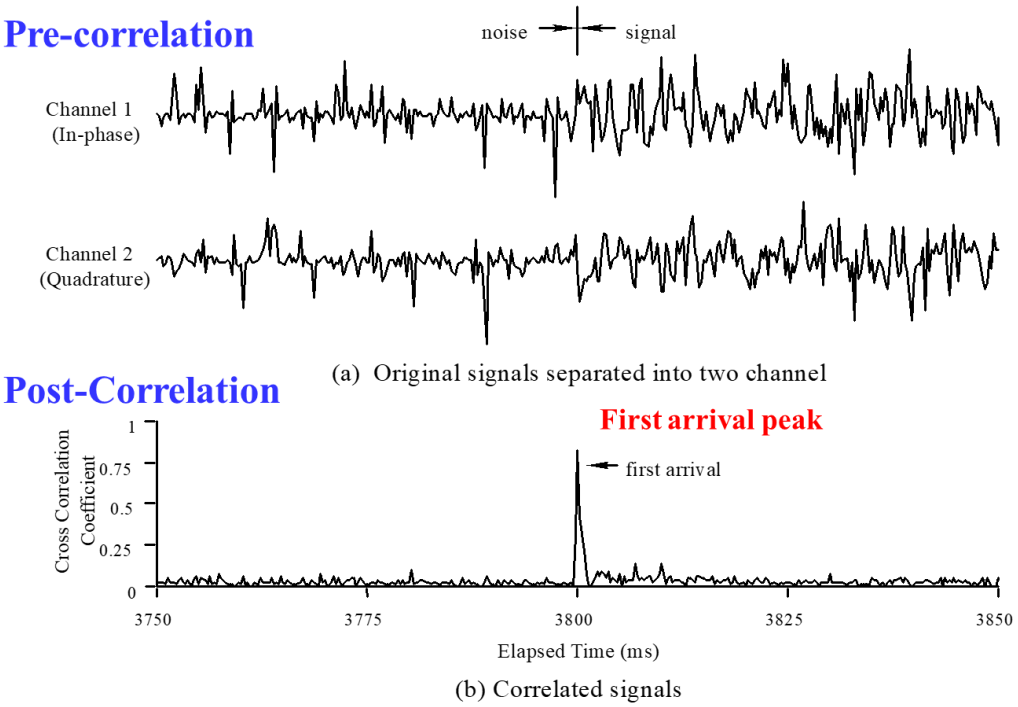

Fig. 2.2 Pre-cross correlation (raw data) and post-cross correlation of the received signals

2.1.2 Arrival Peak Identification

After the cross-correlation process of the received signal, the arrival peak could be obtained, which shows the arrival travel time for each transmission. The number of arrival peaks, resolved in received data, depends strongly on thermal structures, floor depth, and bottom topographies in the tomography site. In the coastal seas where mixing of water is generated due to strong tidal current and the resulting temporal variation of thermal structures exists, the correlation pattern of received data is featured with multi-arrival peaks, and a stable time-wise trace of the arrival peaks becomes difficult. The numbering of multi-arrival peaks is required to determine differential travel times, namely range-average currents for each arrival peak. Multi arrival peaks must be numbered following the correct order of arrival peaks. The inaccurate pairing of arrival peaks produces a significant error in range-average

currents. The identification and trace of multi-arrival peaks are easy works in the coastal seas with weak current and more minor thermal variations. The number of significant arrival peaks is usually only one, and then, the first arrival peak is always the largest arrival peak.

In another viewpoint, multi-arrival peak data are needed as data to enable tomographic inversion in a vertical slice. The inversion process starts by seeking multi-arrival peaks in correlated patterns of received data. Three kinds of methods are presented to identify the first arrival peak from multi-arrival peak data as shown in **Fig. 2.3**. The largest arrival peak method has been first applied in the history of CAT. However, it is not assured that the largest arrival peak is always the first arrival peak in individual experiments. The largest arrival peak in the first sound transmission may be found in the second arrival peak at the next transmission in the sea with strong thermal variability. The largest peak method is not a good method in the experiment when multi-arrival peaks exist in received data. In such a case, the upslope-point method is recommended as an alternative method to identify the first arrival signals as stable information. The first arrival peak is recognized as a point on the first upslope of the correlation pattern in which the level of received signals is over a SNR threshold. The second and third arrival peaks can be identified as peaks over the SNR threshold with time delays from the first arrival peak.

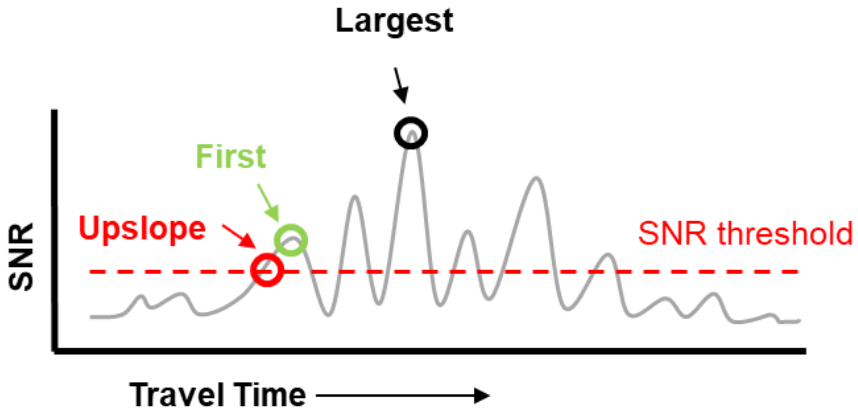

Fig. 2.3 Three kind methods to identify the arrival peak [13]

Two examples in which the largest arrival peak method produces significant errors are shown in **Fig. 2.4** with the stack plots. In **Fig. 2.4 (a)**, the largest peaks construct the first peaks in the first several data, and the first up-slope points over an SNR threshold are always on the upslope side of the first peak. However, the largest peaks are suddenly shifted to the second peaks in the remaining data, while the upslope points are persistently close to the first peaks. In **Fig. 2.4 (b)**, the largest peaks are divided into two groups of the first and the second arrivals.

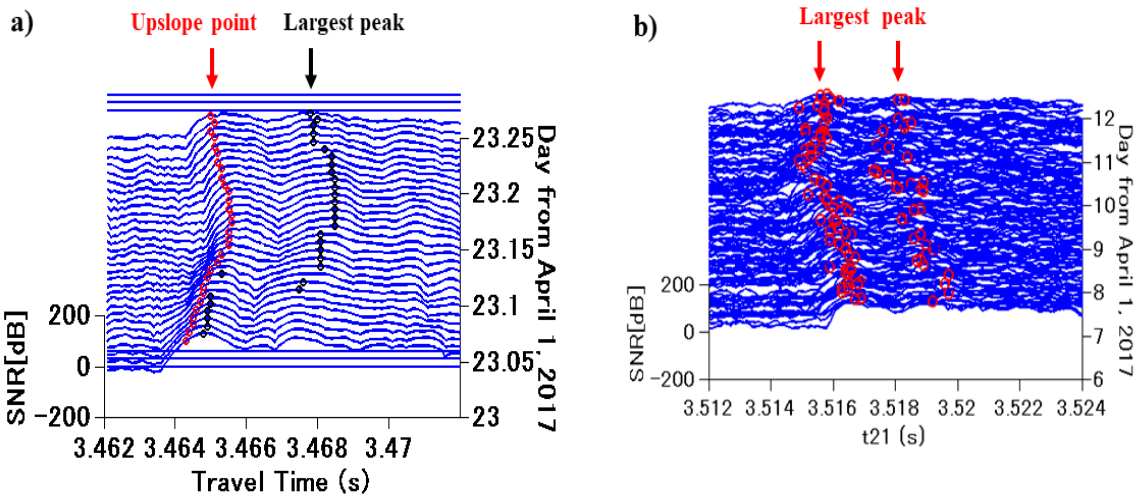

Fig. 2.4 Examples of stack diagram for multi-arrival peak

It is difficult to identify the first arrival peak by the largest arrival peak method while there are several significant arrival peaks. A method is presented here to identify the first arrival peak in the received data with multi arrival peaks [36]. The method consists of two steps. First, all received data are segmented into time spans of width 2 ms. All significant arrival peaks are identified in each time span and circled with colors corresponding to the individual time spans, as shown in **Fig. 2.5**. Second, a smooth time-wise sequence of arrival peaks is taken into consideration. When no arrival peak exists within a certain time span, the nearest arrival peak in the neighboring periods is found in the range of -1 to +1 ms from the present peak position. A smooth time-wise (vertical) sequence of arrival peaks is searched over a specific period and neighboring time spans and grouped with rearranged colors. Finally, the first and the second arrival peaks are dotted with red and green colors, respectively, as seen in **Fig. 2.6**.

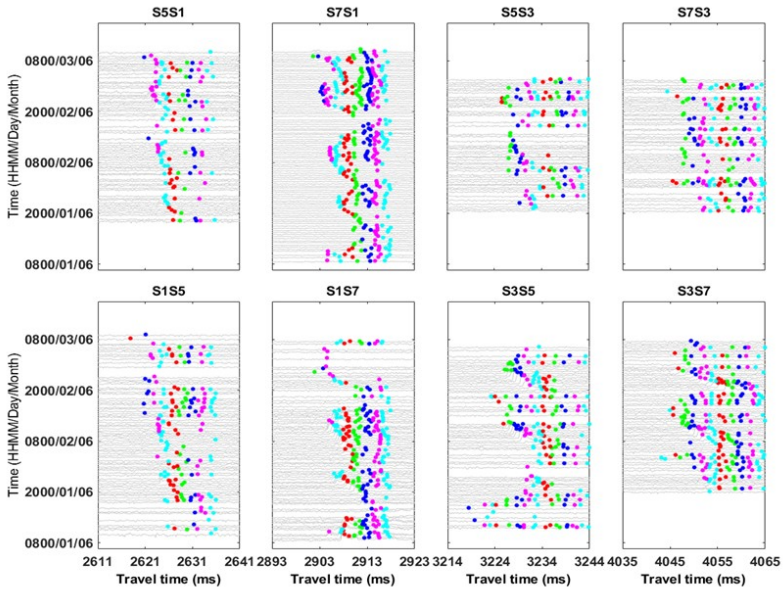

Fig. 2.5 Time plots for several significant arrival peaks [36]

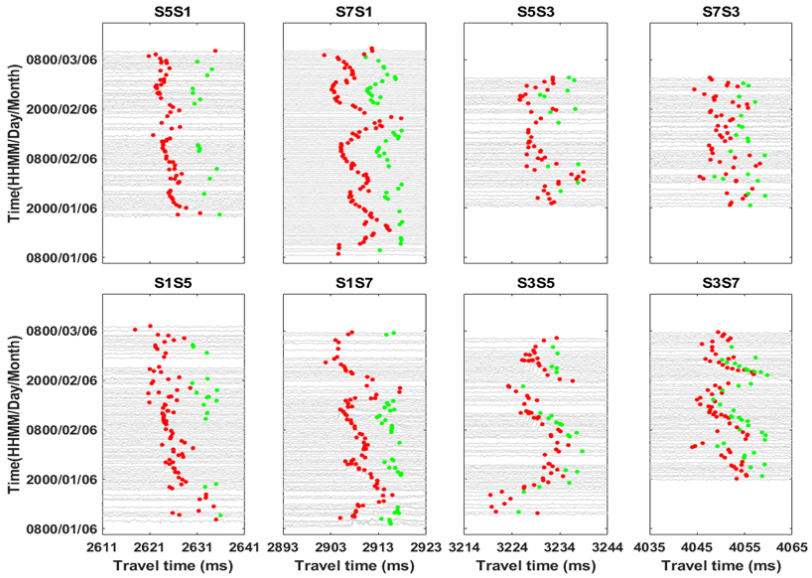

Fig. 2.6 Time plots for first (red dot) and second (green dot) arrival peaks [36]

2.2 Ray Simulation

Ray theory is based on the concept of wavefronts. In a motionless medium, the direction of the wavefront is perpendicular to the direction in which acoustic energy propagates. In a moving medium, the direction of wavefronts is not identical to that of energy propagation by anisotropy due to the presence of flow [37].

Sound propagation in the coastal seas is well approximated by the ray-tracing method that considers only sound refraction (Snell's law of refraction) except for quite shallow seas where modal simulation is a preferable method. Transmission losses and mirror reflections at the surface and seafloor can be considered in ray simulation.

Ray paths in a vertical slice are formulated with the following set of equations:

$$\frac{dx}{dt} = \{C(x,z) + \mathbf{u} \bullet \mathbf{n}\}\cos\theta$$

$$\frac{dz}{dt} = C(x,z)\sin\theta \qquad (2.12)$$

$$\frac{d\theta}{dt} = -\frac{\partial C(x,z)}{\partial z}\cos\theta$$

where $\boldsymbol{u}$ and C are the current and sound speed fields, respectively, in a (x, z) plane and θ is the angle of ray measured counter-clockwise from the horizontal. The initial condition is given at the source position (x=0, z = z_0)

$$x = 0, \qquad z = z_0, \qquad \theta = \theta_0 \tag{2.13}$$

The first order coupled ordinary differential equation (2.12) is numerically solved by a finite difference method such as the 4th order Runge-Kutta method.

The propagation of sound in the CAT experiment is satisfactorily approximated by range-independent ray simulation, which does not take account of the horizontal variation of sound speed fields. The range-independent ray simulation is performed using CTD data on the transmission line. An example of a range-independent ray simulation is shown in **Fig. 2.7**. In this case, a waveguide (surface duct) is constructed in the upper 20 m, so there are several rays passing through the waveguide without making a reflection at the surface and seafloor.

2.3 Travel Time Equation

In sound transmission between two acoustic stations T1 and T2 set in the sea, the reciprocal travel times $t_i^{\pm}$ for the i-th refracted ray traveling in a vertical slice between T1 and T2 may be estimated with the following integral equation along the reciprocal ray paths $\Gamma_i^{\pm}$ (**Fig. 2.8**)

$$t^{\pm} = \int_{\Gamma_i^{\pm}} \frac{ds}{C_0(z) + \delta C(x,\ z) + v(x,z)\cdot \boldsymbol{n}} \tag{2.14}$$

where $C_0(z)$ is the reference sound speed depending on z alone, $\delta C(x,z)$ is the sound speed deviation from $C_0(z)$, $\boldsymbol{v}(x,z)$ is the current vector at(x,z) and $\boldsymbol{\Gamma}_i^{\pm}$ is the i-th ray path for the reciprocal transmission between T1 and T2.

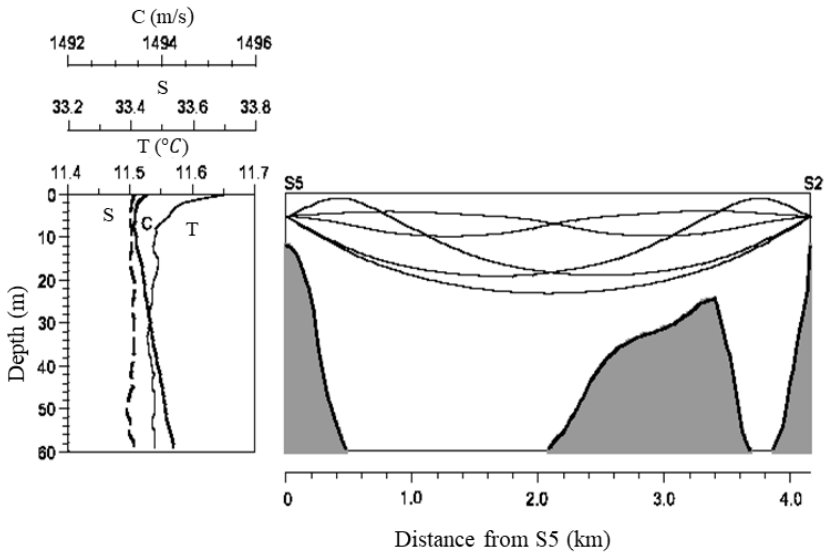

Fig. 2.7 Range-independent ray simulation using CTD data in Akinada of Seto Inland sea [13]

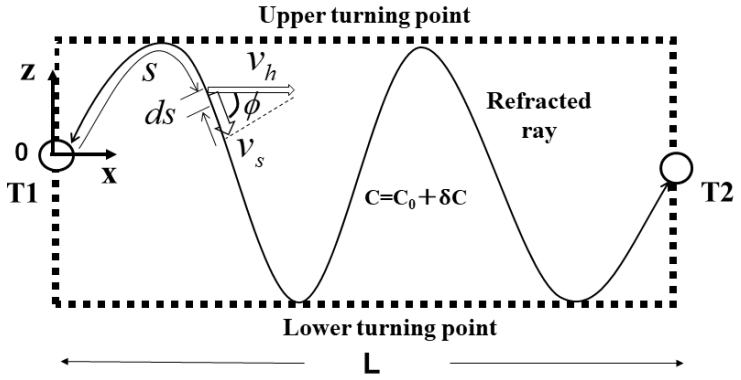

Fig. 2.8 A reciprocal ray that propagating and refracted in a vertical slice between acoustic station T1 and T2 [13]

The refracted ray $\Gamma_i^{\pm}$ is difficult to know in the sea. Instead, ray simulation is performed to know the reference ray path Γ_{0i} using the reference sound speed $C_0(z)$ and the reference travel times t_{0i} are calculated by

$$t_{0i} = \int_{\Gamma_{0i}} \frac{ds}{C_0(z)} \tag{2.15}$$

The past CTD data obtained in the observation site serve the range-independent ray simulation. The travel time deviation from t_0 is formulated with:

$$\tau_i = t^{\pm} - t_0 = \int_{\Gamma_i^{\pm}} \frac{ds}{C_0\left(1 + \dfrac{\delta C \pm \mathbf{v}\cdot\mathbf{n}}{C_0}\right)} - \int_{\Gamma_{0_i}} \frac{ds}{C_0} \tag{2.16}$$

By adopting the Taylor expansion under $\delta C << C_0$ and $u << C_0$ to the first term on the right-hand side of eq. (2.16), it reduces as follows:

$$\tau_i = \int_{\Gamma_i^{\pm}} \frac{ds}{C_0}\left(1 - \frac{\delta C \pm \mathbf{v}\cdot\mathbf{n}}{C_0} + \frac{(\delta C \pm \mathbf{v}\cdot\mathbf{n})^2}{{C_0}^2} - \cdots\right) - \int_{\Gamma_{0_i}} \frac{ds}{C_0} \tag{2.17}$$

Neglecting the terms higher than the second order in the integral, we obtain:

$$\tau_i \approx \int_{\Gamma_i^{\pm}} \frac{ds}{C_0}\left(1 - \frac{\delta C \pm \mathbf{v}\cdot\mathbf{n}}{C_0}\right) - \int_{\Gamma_{0_i}} \frac{ds}{C_0} \tag{2.18}$$

In consideration of $\Gamma_i^{\pm} \approx \Gamma_{0i}$, the second Taylor expansion is adopted around Γ_{0i} to obtain:

$$\tau_i = \int_{\Gamma_{0_i}^{\pm}} \frac{ds}{C_0}\left(1-\frac{\delta C \pm \mathbf{v}\cdot\mathbf{n}}{C_0}\right) + \int_{\Gamma_{0_i}^{\pm}} \frac{\Delta(ds)}{C_0}\left(1-\frac{\delta C \pm \mathbf{v}\cdot\mathbf{n}}{C_0}\right) - \int_{\Gamma_{0_i}} \frac{ds}{C_0}$$

$$= -\int_{\Gamma_{0_i}^{\pm}} \frac{(\delta C \pm \mathbf{v}\cdot\mathbf{n})ds}{C_0^{\,2}} + \int_{\Gamma_{0_i}^{\pm}} \frac{1}{C_0}\left(1-\frac{\delta C \pm \mathbf{v}\cdot\mathbf{n}}{C_0}\right)\Delta(ds) \qquad (2.19)$$

Note that in equation (2.19) the refracted ray paths $\Gamma_i^{\pm}$ are replaced by the simulated ray paths $\Gamma_{oi}^{\pm}$. Neglecting the terms higher than the second order again, we obtain

$$\tau_i \approx -\int_{\Gamma_{0_i}^{\pm}} \frac{(\delta C \pm \mathbf{v}\cdot\mathbf{n})}{C_0^{\,2}} ds \qquad (2.20)$$

The subtraction and summation of two travel time deviations in eq. (2.20) yield

$$\Delta\tau_i = \tau_i^{+} - \tau_i^{-} \approx -2\int_{\Gamma_{0_i}} \frac{v_s}{C_0^{\,2}} ds \qquad (2.21)$$

$$\delta\tau_i = \tau_i^{+} + \tau_i^{-} \approx -2\int_{\Gamma_{0_i}} \frac{\delta C}{C_0^{\,2}} ds \qquad (2.22)$$

where v_s is the current velocity along the ray. Note that current velocity and sound speed deviation fields are perfectly separated in the above two equations.

Next, $\Delta\tau_i$ and $\delta\tau_i$, given by path integrals along the i-th reference ray Γ_{0i}, are approximated by the summations of discrete values:

$$\Delta\tau_i = \sum_{j=1}^{N} E_{ij}\, v_{sj} \qquad (2.23)$$

$$\delta\tau_i = \sum_{j=1}^{N} E_{ij}\,\delta C_j \qquad (2.24)$$

where i and j are the suffices showing the order of the rays and grids, respectively, and $E_{ij} = -2l_{ij}/{C_{0j}}^2$. The v_{sj} and δC_j are the current velocity and sound speed deviation for the j-th grid, respectively, l_{ij} is the arc length of the i-th ray crossing the j-th grid, and C_{0j} is the reference sound speed for the j-th grid. It is reasonably assumed that vertical velocity is negligibly small in most regions of the sea. It leads to $v_s = v_h cos\phi$ (as shown in **Fig. 2.8**).The travel time vector y, the unknown variable vector x, the transform matrix E, and the travel time error vector n are related in the matrix form

$$\mathbf{y} = \mathbf{E}\mathbf{x} + \mathbf{n} \qquad (2.25)$$

where $\mathbf{y} = \{\Delta\tau_i\}$ or $\{\delta\tau_i\}$, $\mathbf{x} = \{v_{sj}\}$ or $\{\delta C_j\}$, $\boldsymbol{E} = \{E_{ij}\}$ and $\mathbf{n} = \{n_i\}$.

2.4 Range-Averaged Current

A CAT field experiment is conducted by reciprocal sound transmission among multi acoustic stations surrounding a tomography domain. As a minimum unit of the CAT system, we shall consider a reciprocal sound transmission in a vertical slice lying between acoustic stations T1 and T2, distanced by L (**Fig. 2.9**).

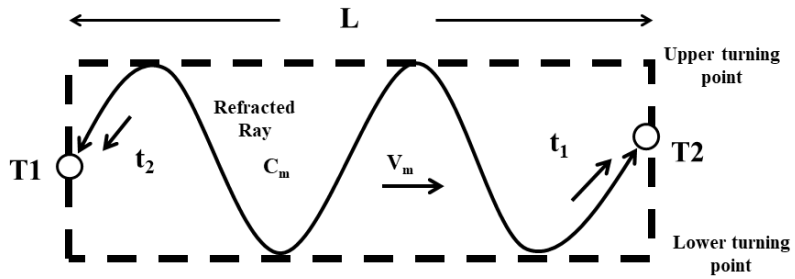

Fig. 2.9 Reciprocal sound transmission between T1 and T2 [13]

The t_1 and t_2 are travel times of sound propagating from T1 to T2 and from T2 to T1, respectively, and are calculated by taking a path integral. The path integral is approximated by a section average from the upper to lower turning point in the vertical slice:

$$t_1 = \int_{\Gamma^+} \frac{ds}{C+v} \approx \frac{L}{C_m + V_m} \qquad (2.26)$$

$$t_2 = \int_{\Gamma^-} \frac{ds}{C-v} \approx \frac{L}{C_m - V_m} \qquad (2.27)$$

Where v is the current velocity defined as a positive direction from T1 to T2 and C is the sound speed. Γ^+ and Γ^- are the ray paths toward T2 from T1 and toward T1 from T2, respectively and ds is the segmented arc length along the ray. V_m and C_m are the section-average current and sound speed and L is the station-to-station distance between T1 to T2.

By solving (2.26) and (2.27), V_m and C_m are determined

$$V_m = \frac{L}{2}\left(\frac{1}{t_1} - \frac{1}{t_2}\right) \approx \frac{C_0^{\,2}}{2L}\Delta t = \frac{L}{2t_0^{\,2}}\Delta t \qquad (2.28)$$

$$C_m = \frac{L}{2}\left(\frac{1}{t_1}+\frac{1}{t_2}\right) \approx \frac{L}{t_m} \qquad (2.29)$$

where $\Delta t = t_2 - t_1$, $t_1 \approx t_2 \approx t_m$ and $t_m = (t_1 + t_2)/2$. C_0 and $t_0 (= L/C_0)$ is the reference sound speed and travel time, respectively. Note that V_m makes little changes even if C_0 replaces C_m because of $C_0 \approx C_m$. As a result, V_m and C_m are independently determined by differential travel time Δt and mean travel time t_m.

Horizontal- Aruni Dinan Hanifa

2.5 Inversion

The reciprocal sound transmission shown in **Fig. 2.9**, expanded for multi-acoustic stations that consist of T1, T2, T3, and T4 stations. The transmission lines connecting each acoustic pair projected to the horizontal slice are shown in **Fig. 2.10** (the green line). The range-averaged in the vertical slice information between two stations from the upper turning point to bottom, is transferred to the projected ray on a horizontal slice.

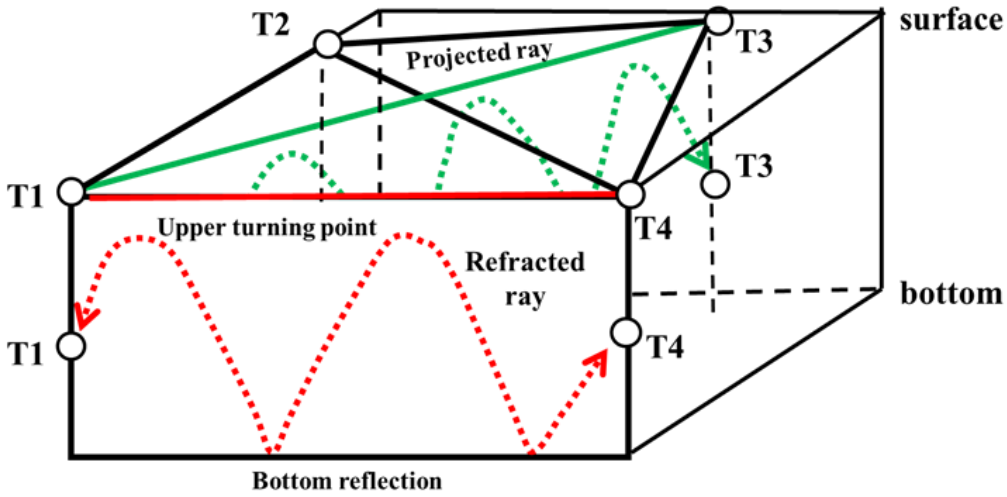

Fig. 2.10 The real rays projected onto a horizontal slice [13]

The tapered least-squares method accompanied by the L-curve method is presented as a method suitable for the function expansion method that does not require a smoothing process in the inverse method [38]. The smoothing of the solution is included implicitly in the process of function expansion. For a two-dimensional current field, the stream function is expanded into a series of functions instead of the current velocity field itself for simplicity. Sound speed deviation fields are also expanded into a series of functions as well as current velocity fields.

After the real (refracted) ray in a vertical slice is projected onto a horizontal slice, equations (2.21) and (2.22) in Subchapter 2.3 are re-written for the i-th ray as follows:

$$\Delta\tau_i = -2\int_0^{L_i} \frac{\left(u_j cos\theta_i + v_j sin\theta_i\right)}{{C_0}^2} d\xi \qquad (2.30)$$

$$\delta\tau_i = -2\int_0^{L_i} \frac{\delta C_j}{{C_0}^2 cos\phi_i} d\xi \qquad (2.31)$$

where $v_s = v_h cos\phi_i$, $d\xi = ds cos\phi_i$ and $v_h = u_j cos\theta_i + v_j sin\theta_i$ (see **Figs. 2.8** and **2.11**).

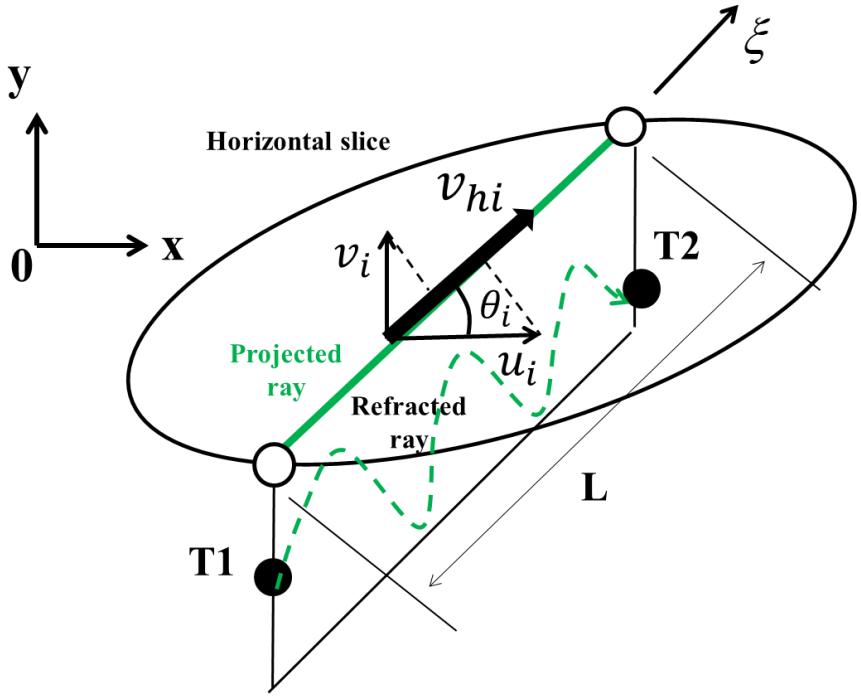

Fig. 2.11 The refracted ray on a vertical slice and its projection onto a horizontal slice [13]

Two-dimensional current velocity fields (u, v) are represented by stream function ψ:

$$u = -\frac{\partial \psi}{\partial y} \; ; \; v = \frac{\partial \psi}{\partial x} \qquad (2.32)$$

Substituting Eq. (2.32) into Eq. (2.30), we obtain

$$\Delta\tau_i = -2 \int_0^{L_i} \frac{\left(-\frac{\partial \psi}{\partial y} cos\theta_i + \frac{\partial \psi}{\partial x} sin\theta_i\right)}{{C_j}^2} \qquad (2.33)$$

Then, ψ is expanded into Fourier function series which is one of familiar function series:

$$\Psi(x,y) = ax + by + \sum_{k=0}^{N_x}\sum_{l=0}^{N_y}\left\{A_{k,l}\cos 2\pi\left(\frac{kx}{L_x}+\frac{ly}{L_y}\right) + B_{k,l}\sin 2\pi\left(\frac{kx}{L_x}+\frac{ly}{L_y}\right)\right\} \quad (2.34)$$

Also, ψ is decomposed into two parts of expansion functions and coefficients:

$$D = \{D_j\} = \left\{a, b, A_{00,}, B_{00}, A_{01}, B_{01}, \cdots\cdots\cdots\cdots, A_{N_xN_y}, B_{N_xN_y}\right\} \quad (2.35)$$

$$Q(x,y) = \{Q_j\} = \left\{x, y, 1, 0, \cos\frac{2\pi y}{L_y}, \sin\frac{2\pi y}{L_y}, \cdots\cdots\cdots, \cos 2\pi\left(\frac{N_x x}{L_x}+\frac{N_y y}{L_y}\right), \sin 2\pi\left(\frac{N_x x}{L_x}+\frac{N_y y}{L_y}\right)\right\} \quad (2.36)$$

By using Eq. (2.35) and Eq. (2.36), (2.33) is re-written

$$\Delta\tau_i = -\frac{2}{C_0^2}\sum_{j=1}^{(N_x+1)(N_y+1)} D_j \int_0^{L_i}\left(-\frac{\partial Q_j}{\partial y}\cos\theta_i + \frac{\partial Q_j}{\partial x}\sin\theta_i\right)d\xi \quad (2.37)$$

where, the function expansion coefficients become unknown variables instead of u_j and v_j. The number of unknown variables is 20 for N=2 and 36 for N=3.

Similarly, sound speed deviation fields are expanded into the Fourier function series:

$$\delta C(x,y) = a + \sum_{k=0}^{N_x}\sum_{l=0}^{N_y}\left\{A_{k,l}\cos 2\pi\left(\frac{kx}{L_x}+\frac{ly}{L_y}\right) + B_{k,l}\sin 2\pi\left(\frac{kx}{L_x}+\frac{ly}{L_y}\right)\right\} = \sum_{j=1}^{(N_x+1)(N_y+1)} F_j\, R_j(\mathrm{x}, \mathrm{y}) \quad (2.38)$$

$$\boldsymbol{F} = \{F_j\} = \left\{a, A_{00,}, B_{00}, A_{01}, B_{01}, \cdots\cdots\cdots\cdots, A_{N_xN_y}, B_{N_xN_y}\right\} \quad (2.39)$$

$$\boldsymbol{R}(x,y) = \{R_j\} = \left\{1,1,0, cos\frac{2\pi y}{L_y}, sin\frac{2\pi y}{L_y}, \cdots\cdots\cdots, cos2\pi\left(\frac{N_x x}{L_x} + \frac{N_y y}{L_y}\right), sin2\pi\left(\frac{N_x x}{L_x} + \frac{N_y y}{L_y}\right)\right\} \quad (2.40)$$

Substituting Eq. (2.38) into Eq. (2.31), we obtain

$$\delta\tau_i = -\frac{2}{C_0^2} \sum_{j=1}^{(N_x+1)(N_y+1)} F_j \int_0^{L_i} \frac{R_j}{cos\phi_i} d\xi \quad (2.41)$$

Equations (2.37) and (2.41) are re-written in the matrix form with travel time error vector $\boldsymbol{n}$:

$$\boldsymbol{y} = \boldsymbol{E}\boldsymbol{x} + \boldsymbol{n} \quad (2.42)$$

The Cartesian coordinate (x, y) is defined as shown in **Fig. 2.12** to solve the equation matrix (2.42). The size of the computational domain is taken twice that of the tomography domain. As a result, the unnatural periodicity of current and sound speed deviation provided in the tomography domain is broken by the first expansion function, of which the wavelength is equal to the width of the computational domain. In this case, the x-axis is taken in parallel to transmission line T4T5. The transmission line in parallel to the x-axis spoils the inverse calculation seriously on a horizontal slice. Then, the coordinate frame is rotated counter-clockwise by an angle such that the new x-axis is not parallel to any transmission lines within an offset smaller than approximately one degree. Without this rotation, no information on current perpendicular to T4T5 is given to transform matrix ***E,*** and then one row in ***E*** is occupied with the null space. Thus, the inverse calculation of E is overflowed infinitely.

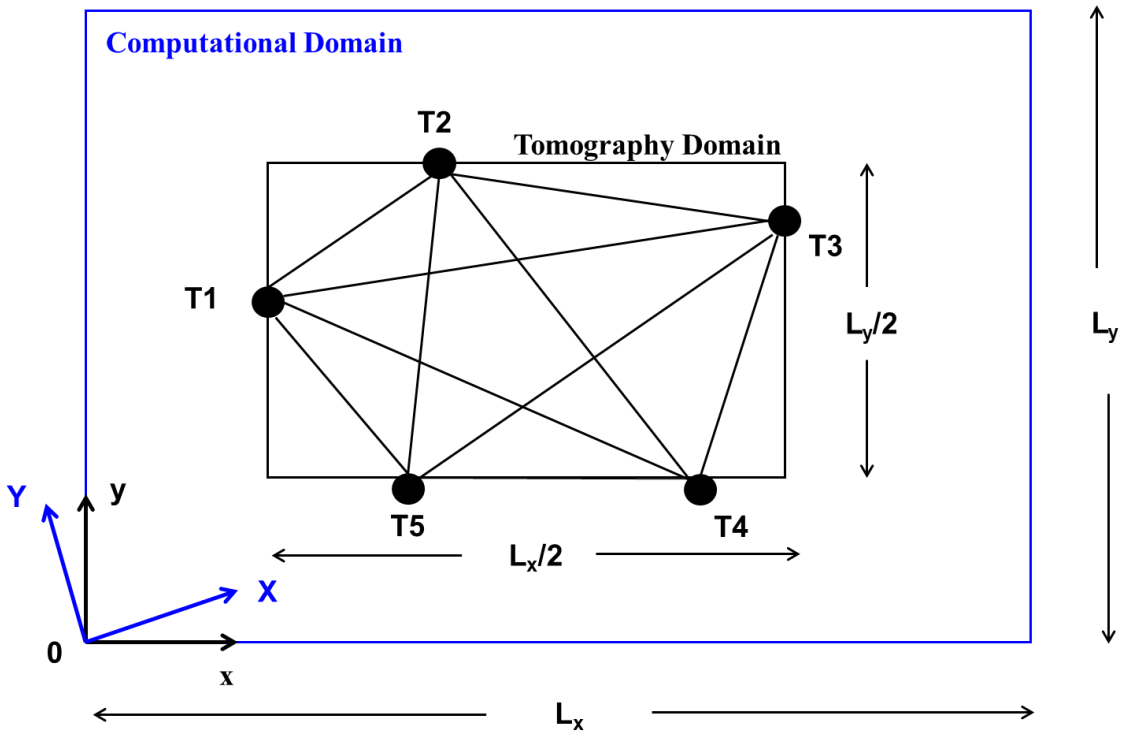

Fig. 2.12 The design of computational domain and tomography domain [13]

The tapered least square method is here adopted as the best-fitted method to solve equation matrix (2.42). Objective function $\boldsymbol{J}$ is given

$$\boldsymbol{J} = \boldsymbol{n}^T\boldsymbol{n} + \alpha^2\boldsymbol{x}^T\boldsymbol{x} = (\boldsymbol{y} - \boldsymbol{E}\boldsymbol{x})^T(\boldsymbol{y} - \boldsymbol{E}\boldsymbol{x}) + \alpha^2\boldsymbol{x}^T\boldsymbol{x} \qquad (2.43)$$

where α is the damping factor. For $\alpha = 0$, tapered least square method reduces generalized inverse. The expected solution of $\boldsymbol{x}$ is found by taking $\boldsymbol{x}$-derivative of $\boldsymbol{J}$ and putting the result into zero:

$$\hat{\boldsymbol{x}} = (\boldsymbol{E}^T\boldsymbol{E} + \alpha^2\boldsymbol{I})^{-1}\boldsymbol{E}^T\boldsymbol{y} \qquad (2.44)$$

By introducing singular value decomposition (SVD), $\boldsymbol{E}$ reduces

$$\mathbf{E} = \sum_{i=1}^{N_s} \lambda_i \, \boldsymbol{u}_i \boldsymbol{v}_i{}^T = \boldsymbol{U}\boldsymbol{\Lambda}\boldsymbol{V}^T \qquad (2.45)$$

where $\mathbf{U} = \left[\boldsymbol{u}_1 \; \boldsymbol{u}_2 \; \cdots\cdots \; \boldsymbol{u}_{N_s}\right]$, $\mathbf{V} = \left[\boldsymbol{v}_1 \; \boldsymbol{v}_2 \; \cdots\cdots \; \boldsymbol{v}_{N_s}\right]$ and $\Lambda = \begin{pmatrix} \lambda_1 & \cdots & 0 \\ \vdots & \ddots & \vdots \\ 0 & \cdots & \lambda_{N_s} \end{pmatrix}$

The N_s is the number of non-zero singular values.

By using Eq. (2.45), the Eq. (2.44) is re-written

$$\hat{\boldsymbol{x}} = \sum_{i=1}^{N_s} \frac{\lambda_i (\boldsymbol{u}_i{}^T \boldsymbol{y}) \boldsymbol{v}_i}{\lambda_i{}^2 + \alpha^2} \qquad (2.46)$$

From equations (2.44) and (2.46), the expected travel time error vector $\hat{\boldsymbol{n}}$ becomes

$$\hat{\boldsymbol{n}} = \boldsymbol{y} - \boldsymbol{E}\hat{\boldsymbol{x}} = \{\boldsymbol{I} - \boldsymbol{E}(\boldsymbol{E}^T\boldsymbol{E} + \alpha^2\boldsymbol{I})^{-1}\boldsymbol{E}^T\}\boldsymbol{y} \qquad (2.47)$$

Substituting Eq. (2.47) into $\boldsymbol{y}$ in Eq. (2.44), we obtain the error for the expected solution

$$\hat{\boldsymbol{x}}_{err} = (\boldsymbol{E}^T\boldsymbol{E} + \alpha^2\boldsymbol{I})^{-1}\boldsymbol{E}^T\hat{\boldsymbol{n}} \qquad (2.48)$$

The solution uncertainty, which is the variance of solution error, is given

$$\mathbf{P} = (\boldsymbol{E}^T\boldsymbol{E} + \alpha^2\boldsymbol{I})^{-1}\boldsymbol{E}^T\langle \boldsymbol{n}\boldsymbol{n}^T\rangle E(\boldsymbol{E}^T\boldsymbol{E} + \alpha^2\boldsymbol{I})^{-1} \quad (2.49)$$

where $\langle \boldsymbol{n}\boldsymbol{n}^T\rangle$ is the expected variance of travel time error.

The damping factor α is determined by L-curve method [39, 40] in which the square of expected solution ξ is plotted against the square of expected error ς, changing α as a parameter (**Fig. 2.13**). The ξ becomes

$$\xi = \hat{\boldsymbol{x}}^T\hat{\boldsymbol{x}} = \sum_{i=1}^{N_s} \frac{{\lambda_i}^2\beta^2}{\left({\lambda_i}^2 + \alpha^2\right)^2} \quad (2.50)$$

where $\beta = {\boldsymbol{u}_i}^T\boldsymbol{y}$. The ζ becomes

$$\varsigma = (y - E\hat{x})^T(y - E\hat{x}) = \sum_{i=1}^{N_s} \frac{\alpha^4\beta^2}{\left({\lambda_i}^2 + \alpha^2\right)^2} \quad (2.51)$$

The curvature κ of L-curve is calculated by

$$\kappa = \frac{\varsigma'\xi'' - \varsigma''\xi'}{\{(\varsigma')^2 + (\xi')^2\}^{3/2}} \quad (2.52)$$

The optimal α is determined at a point on L-curve with maximum curvature.

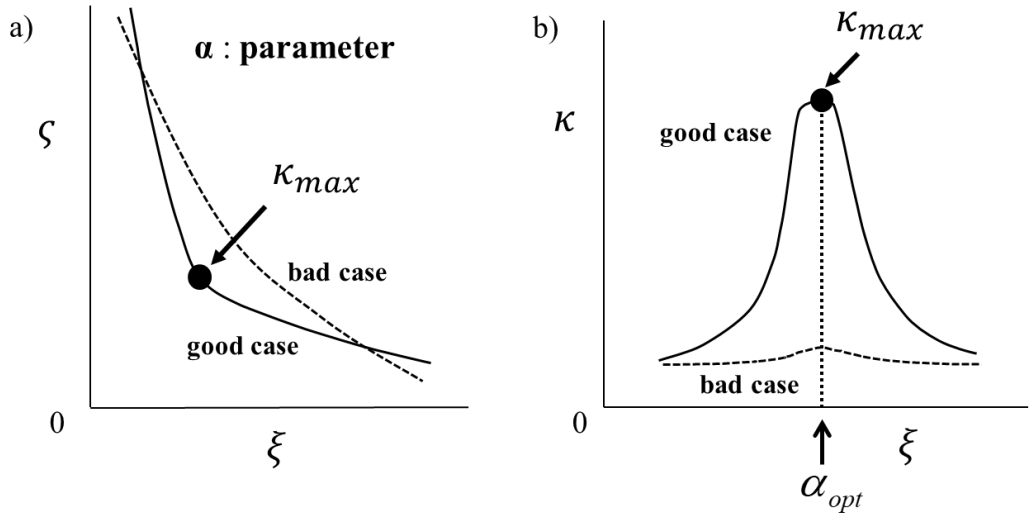

Fig. 2.13 The schematic diagrams for determining the maximum curvature κ_{max} and optimal damping α_{opt} [13]

It is a noticeable point that α is updated every sound transmission in the present method. As a result, this method provides flexibility to reconstruct rapidly-varying current fields in the coastal sea. Such flexibility may be considered lost in the Gauss-Markov method (stochastic inverse), which requires a variance of the expected solution prior to inverse analysis. In contrast to observation error variance estimated from CAT travel time data, it is difficult to estimate the variance of expected solution a priori because no past comprehensive data usually exists for current velocity fields.

A good inversion result is obtained when the L curve is folded at the maximum curvature point. Conversely, the quality of the inversion result is worse when the curve is flattened over the entire part of the curve. It occurs when incorrect travel-time data are included, or some singular (eigen) values are close to zero due to the worse geographical arrangement of acoustic stations such that station arrangement is symmetric or some of the transmission lines are nearly overlapped. The effect of the travel time data

corresponding to near-zero singular values is suppressed in the inversion result due to the damping factor α, but the spatial resolution is not improved by considering the worse travel-time data.

2.6 Error Evaluation

2.6.1 GPS Clock Correction

For land-type CAT, precise clock signals with an accuracy 0.6 μs are provided by GPS clock. However, GPS clock signals are impossible to be used for moored-type CAT which every portion of the system is located in the subsurface. In the early history of an atomic clock, its power consumption was significantly large, so continuous operation of the atomic clock was not acceptable for long-term mooring. Instead, a timing module composed of the quartz clock and Rubidium clock was equipped for maintaining a long-term accuracy of travel time measurement under acceptably small power consumption. The drift of the quartz clock operated continuously was measured by comparing oscillation frequencies of quartz and atomic clocks at a predetermined interval. This clock correction is needed, especially for current velocity measurement that requires strict clock accuracy. Special attention to clock correction is not needed to be paid in sound speed measurement by reciprocal transmission. Any clock drift owned by each subsurface station is canceled out in the process to calculate a mean travel time from reciprocal travel-time data, obtained every transmission between two acoustic stations.

Reciprocal sound transmission between acoustic stations T1 and T2 which have their own clock errors $\delta t_1$and δt_2, respectively is sketched in **Fig. 2.14**. Clock errors first appear in the transmission time $t_0 + \delta t_1$ for T1 and $t_0 + \delta t_2$ for T2. One-way travel time is $(t_{21} + \delta t_1)$-$(t_0 + \delta t_1)$ for T2 to T1 and $(t_{12} + \delta t_2)$-$(t_0 + \delta t_2)$ for

T1 to T2, including the clock errors. Averaging the two one-way travel times, we obtain mean travel time $[(t_{12} + t_{21})/2 - t_0]$ in which clock errors diminish. We can take $t_0 = 0$ without losing generality.

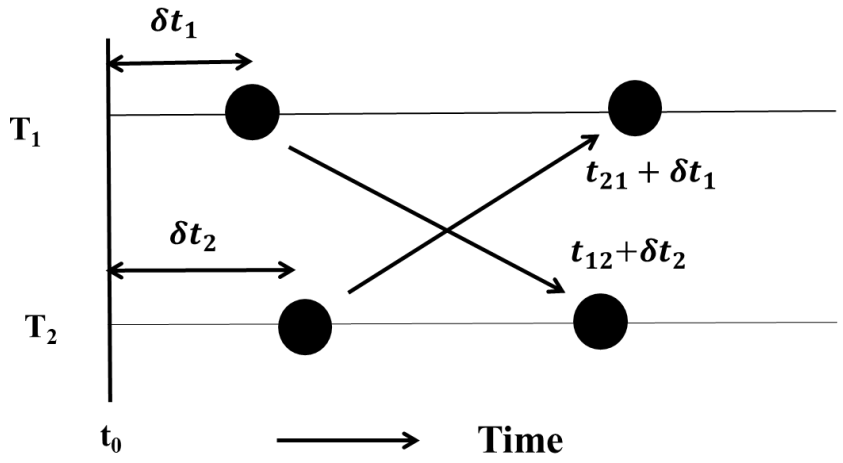

Fig. 2.14 Time chart of reciprocal sound transmission between T1 and T2 stations [13]

2.6.2 Station Movement Error

An error comes from the movement of acoustic stations deployed in the sea with currents. If the subsurface stations are fixed on a tower, this error does not arise. However, if the stations are placed on a subsurface mooring line as a possible way, the movement of the stations may produce errors in differential travel times [41].

Here let us consider the sound transmission between station S1 at $(x_1,0)$ and station S2 at $(x_2,0)$ in a (x, z) plane as shown in **Fig. 2.15**, where L is the original station-to-station distance, δx_1 and δx_2 are the displacements of the station from x_1, and x_2, respectively, $\delta L = \delta x_2 - \delta x_1$ is the displacement from L and u_1 and u_2 are the horizontal moving speeds of stations S1 and S2, respectively. Let t_{12} and t_{21} denote the travel times of the ray propagating from S1 to S2 and from S2 to S1,

respectively. Under an assumption that vertical current in the sea is negligible, the reciprocal along-ray travel times are calculated by

$$t_{12} = \frac{L + \delta L}{C_0 + \delta C_m + u_m - u_2} \approx \frac{(L + \delta L)}{C_0}\left\{1 - \frac{\delta C_m + u_m - u_2}{C_0}\right\} \quad (2.53)$$

$$t_{21} = \frac{L + \delta L}{C_0 + \delta C_m - (u_m - u_1)} \approx \frac{(L + \delta L)}{C_0}\left\{1 - \frac{\delta C_m - u_m + u_1}{C_0}\right\} \quad (2.54)$$

where u_m is the range-average current and δC_m is the range-average sound speed deviation from the reference sound speed C_0. Then, the differential travel time Δt_{12} is given

$$\Delta t_{12} = t_{21} - t_{12} = \frac{(L+\delta L)}{{C_0}^2}\{2u_m - (u_1 + u_2)\} \quad (2.55)$$

Note that the effect of sound speed deviation on the differential travel time is canceled in reciprocal transmission. At the first and second terms on the right-hand side, the term $2Lu_m/{C_0}^2$ with no relation to the movement of the subsurface stations, is removed and the remaining terms are defined as differential travel time error ${\Delta t_{12}}^{err}$:

$${\Delta t_{12}}^{err} = -\frac{L}{{C_0}^2}(u_1 + u_2) + \frac{2\delta L}{{C_0}^2}\left\{u_m - \frac{(u_1 + u_2)}{2}\right\} \quad (2.56)$$

In most cases, δL/L is smaller than 1/100 and thus the second term of (2.56) is vanishingly small even when the positioning errors of GPS is about 10 m. It is suggested that the effect of the movement of the subsurface station on differential travel time is negligibly small.

2.7 Methods and Models for Bali Strait case

2.7.1 Signal to Noise Ratio (SNR)

A 10^{th} order M-sequence was used for the sound transmission in the Bali Strait experiment. By applying the eq. (2.11), the SNR of the received signals could be calculated as

$$\mathrm{SNR} = 20\log\sqrt{2^{\mathrm{M}} - 1} = 20\log\sqrt{2^{10} - 1} = 30.1 \text{ dB}$$

Using a 10 min moving-averaged method, the high-frequency noise removed and the SNR of the received signals is increased by 10 dB. So, the SNR threshold is between 30-40 dB.

2.7.2 A 10-kHz Frequency of Transducer

The shortest distance in this experiment was 4,020 m (S1-S5), and the farthest distance was 6,210 m (S3-S7). The range-average current error depends on the time resolution, as follows:

$$V_e = \frac{{C_0}^2}{2L} t_r \qquad (2.57)$$

where the C_0, is the reference speed, L, is the distance between stations, *tr*, is time resolution. While the time resolution calculation affected by the cycles of M-sequences and the frequency of the transducer, as follows:

$$tr = \frac{Q}{f} \qquad (2.58)$$

A 5 kHz frequency could be used for this experiment, but we chose 10 kHz. The higher frequency produced better time resolution. The smaller value of time resolution means better resolution, because the error becomes smaller based on Eq. (2.57). As we applied, the *Q* value is three, and *f* is 10000. The *tr* is about 0.33 ms. So,

as we put the *tr* value to the Eq. (2.57), the current velocity error that could be obtained from the observation is about 0.08 ms^{-1}.

2.7.3 Arrival Peak Identification

Based on the SNR calculation for the received signals, the SNR threshold was set to 35 dB. There were several significant arrival peaks with SNRs of >35 dB. The largest peak and upslope methods do not fit to identify the first arrival peak. Chen et al. (2019) proposed the multi-arrival peak method to determine the first arrival peak among the multiple arrival peaks [36]. This method was adopted to identify the first arrival peak.

First, the largest arrival peak with SNR >35 was determined within each 2-ms-wide timespan and circled with different colors, as shown in **Fig. 2.5**. Second, the largest arrival peaks with a smooth timewise sequence were traced considering the neighboring timespans, and red colors were allocated to the sequential first arrival peaks, as shown in **Fig. 2.6**.

2.7.4 Ray Simulation

The 2014 CTD data was used for the range-independent ray simulation in the Bali Strait. In the simulation, the sea-surface roughness and the fine topography of the seafloor were not taken into account. Furthermore, absorption losses during the sound transmission and reflection losses at the sea surface and seafloor were not considered.

2.7.5 Range Averaged Current (RAC)

There were four acoustic pairs in the Bali Strait experiment. Those were S1S5, S1S7, S3S5, and S3S7. As for the RACs will be denoted as V15 (as for S1S5), V17 (as for S1S7), V35 (as for S3S5), and V37 (as for S3S7). The total 30-h data decomposed into two-period bands, A (6-h low pass filter/LPF), and B (10-min to 6-h band pass filter/BPF). Furthermore, the A-band was intended to retrieve the semidiurnal tidal current (M2 current), and the B-band was intended to retrieve the 3-h oscillation (M8 current). So, the total RAC to analyzes the tidal current characteristics is eight RACs.

2.7.6 North-East Current Components

The North-East current components (V_N, V_E) could calculated from two range-averaged currents. As refers to the previous research [42], according to CAT data obtained in the Bali Strait on June 2016, two range-average currents V_{15} and V_{37} are obtained along two transmission lines S1-S5 and S3-S7, crossing the strait (**Fig. 2.15**). These currents can be converted to the east-west and north-south current components (V_E, V_N) by following equations:

$$V_E = \frac{V_{15}cos\theta_{37} - V_{37}cos\theta_{15}}{sin\theta_{15}cos\theta_{37} - cos\theta_{15}sin\theta_{37}} \quad (2.59)$$

$$V_N = \frac{-V_{15}sin\theta_{37} + V_{37}sin\theta_{15}}{sin\theta_{15}cos\theta_{37} - cos\theta_{15}sin\theta_{37}} \quad (2.60)$$

where θ_{15} = 96.4 ° and θ_{37} =147.9°are the angles of S1-S5 and S3-S7, respectively, measured clockwise from north. VE and VN for two more transmision line pairs S1S5-S1S7 and S1S5-S3S5 are also formulated through a similar procedure, using θ_{17}= 117.8°and θ_{35}=137.4°.

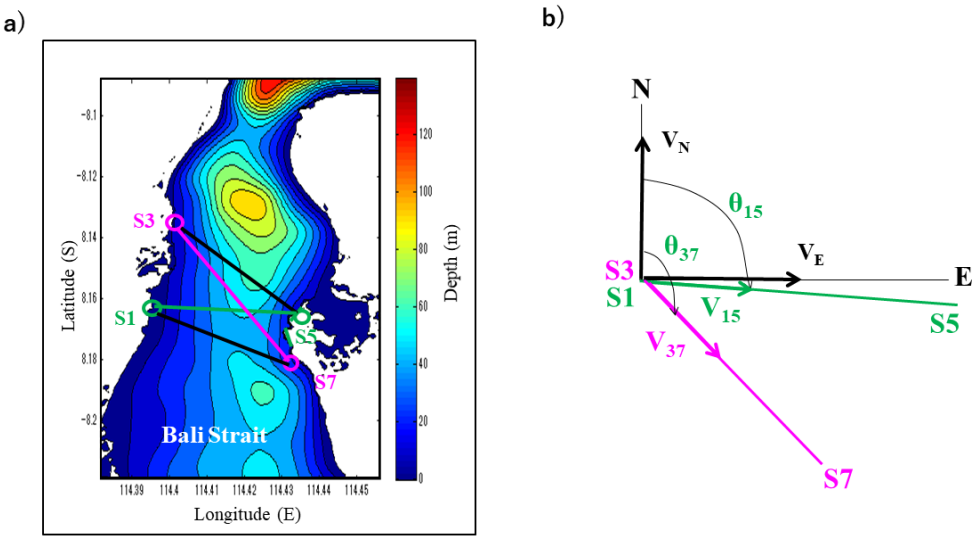

Fig. 2.15 North-East current component conversion for Bali Strait experiment

2.7.7 Horizontal-slice Inversion

As from the total 30-h period of total raw data from CAT, the first half day of June 2nd, 2016, (00:00-13:00) was the focus period for the horizontal-slice inversion or spatiotemporal current fields. As shown in **Fig. 2.15**, the coastline of the east side of Java Island and the west side of Bali Island was complicated. A complicated coastline could be traced by adding virtual acoustic stations located at the protruded point of the coastline and added the artificial straight coast connecting the virtual stations [13], as shown in **Fig. 2.16**. The differential travel times of the artificial straight coast set to zero meant that no real sound transmissions were received. The nonslip conditions were applied for the coastlines. This condition does not inhibit currents perpendicular to the coasts, in contrast to the actual coasts [13].

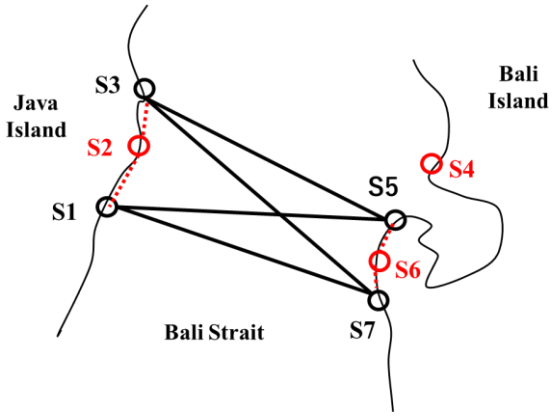

Fig. 2.16 Artificial stations and coasts added as the red circles and dash lines [13]

By applying Eq. (2.34) truncated the Fourier function series to two order (N=2) for the Bali Strait case. So, the unknown coefficients become 20. And to solve Eq. (2.42) in the Cartesian coordinate, the x-axis is taken in parallel to transmission line S1S7. By rotating the coordinate frame 8.16 degrees counter-clockwise, it will delete the null space in the transform matrix **E** in Eq. (2. 42).

CHAPTER 3 TOMOGRAPHIC MEASUREMENT OF TIDAL CURRENT AND ASSOCIATED 3-HOUR OSCILLATION IN BALI STRAIT

3.1 Introduction

Coastal acoustic tomography (CAT) has been developed as a coastal sea application of ocean acoustic tomography [10, 11]. The instrumentation and methodology of ocean acoustic tomography have been employed for CAT studies, with a focus on current velocity rather than sound speed. CAT has been successfully applied to coastal seas with various dynamic characteristics in Japan [26, 19, 43, 20, 44, 21, 45], China [27, 22, 46, 47, 48], and Taiwan [49]. Among these CAT studies, two studies were typical examples to verify the accuracy of CAT data [27, 50]. The accuracy of the original CAT data, such as the range-average current (RAC) along transmission paths, was validated against vessel-mounted acoustic Doppler current profilers (ADCPs) data at specific times and spaces during the experiment. In Zhu *et al*. (2012), with 21 ADCP transects registered along a CAT transmission path the root-mean-square difference (RMSD) between the RACs for both the data was 0.04 ms^{-1} which was approximately 8 % of the mean amplitude of the measured oscillatory current. Zhu *et al*. (2015) reported a RMSD of 0.03–0.04 ms^{-1} (approximately 8–10 % of the mean amplitude of the measured tidal current) between the CAT and ADCP data for the four transmission paths.

The Bali Strait is located between the islands of Java and Bali (**Fig. 3.1**). It is approximately 80 km long and connects the Indian Ocean in the south to the Java Sea in the north. The strait is funnel-shaped, with a wide side (60 km wide and a mean depth of 365 m) in the south that gradually narrows toward the north (2 km wide and 50 m deep). At the observation site, 7 km from the northern end, the strait width is approximately 5 km; tidal waves entering the strait from the Indian Ocean are remarkably amplified

within the strait. Strong and highly variable currents at the observation site disrupt scheduled ferry operations. Long-term measurements of currents with a vessel-mounted ADCP at a high temporal frequency across the strait are impossible and unsafe due to the strength and variability of currents in time and space.

Additionally, in strong currents, ADCP mooring is difficult even for bottom-moored systems. A ferry-sinking accident occurred in 2016. Despite the societal importance of predicting these strong, rapidly varying currents, previous efforts have been mainly restricted to a model study of tides and tidal currents [30]. One-point ADCP data obtained at the northern end of the strait were used with some observational evidences of higher-frequency oscillation. However, no further observations have been performed, except for a CAT experiment limited to one transmission path [25].

In well-mixed conditions, the mid-frequency sound pulses emitted by CAT traverse the entire cross-section confined between both sides of a strait, providing section-averaged current with no geometrical calibration needed [51, 52, 42, 50, 53, 25, 23]. The CAT is an observational method suited to current-field measurements in the Bali Strait with strong and highly variable currents.

3.2 Experiment Design

A CAT experiment was conducted at the northern part of the Bali Strait with the highest priority of Indonesian government after the ferry sinking accident in 2016 due to strong and highly variable currents. The method inherently involves deploying the acoustic nodes on both side of a strait, so four CAT acoustic nodes were deployed in the Bali Strait, as shown in **Fig. 3.1**. Reciprocal sound transmissions were performed among the stations over June 1–3 2016, local time (GMT+8).

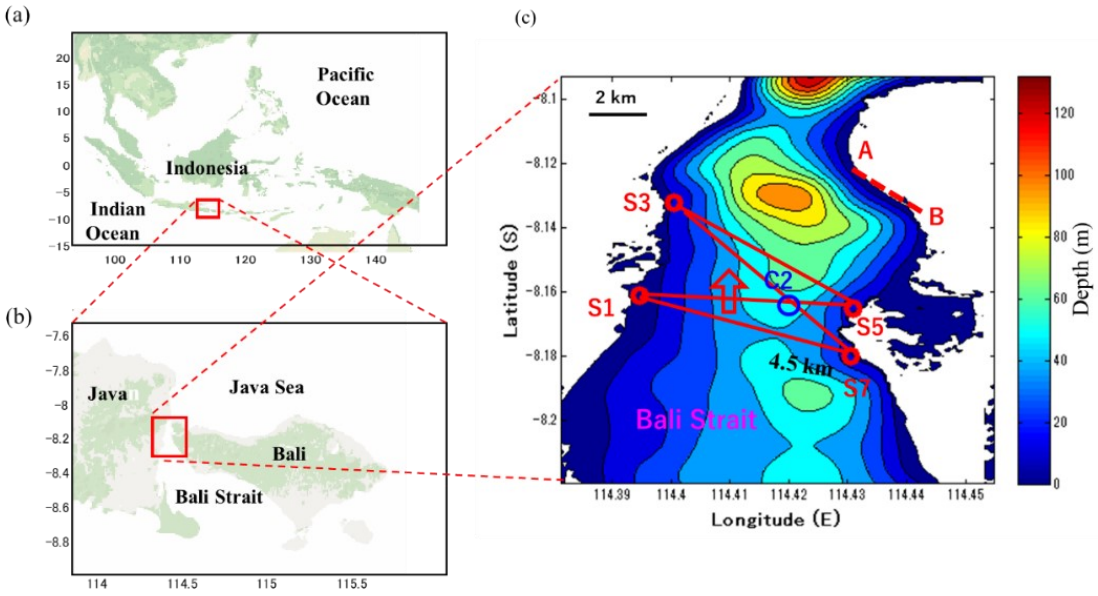

Fig. 3.1 Bali Strait location [24]

The observation length was limited by the time we were allowed to use private facilities, such as wharves, jetties, and towers, for temporary installation of CAT, apart from vandalism issues. At each of the stations, a broadband monostatic ITC3013 transducer with a source-level of 192 dB re one μPa at 1 m at a 10-kHz central frequency was positioned. The transducer was set 5 m above the seafloor at all the stations, except for S1, where it was set to the middle of the water depth (4 m). All the transducers were disk-type, with omnidirectional directivity in the horizontal plane, and the lower semi-spherical directivity and the upper excess directivity of 30° from the horizontal in the vertical plane. When the disk surface was directed downward in water, sound transmission and reception were performed using the lower semi-spherical directivity and the upper excess directivity of 30°. The transducers could swing freely with currents because they did not touch the seafloor. The swing of the transducer was particularly large at S3 with the strongest current.

The mean water depths at each station and the distances for the corresponding transmission paths, as determined using a global positioning system (GPS) with the positioning accuracy of approximately 10 m, are presented in **Table 3.1**. Bathymetric data were obtained from the Marine Geoscience Data System (MGDS). A pressure sensor was attached above the acoustic transducer on the suspension line to measure the variations in the sea-surface height (SSH) at S7. The SSH data were used to determine the amplitude and phase of the tides. Additionally, the conductivity-temperature-depth (CTD) data obtained from the surface to the seafloor at station C2 in March 2014 were used in this experiment to calculate the sound-speed profile. At the observation site, the temperature profile for June 2015 was approximately the same as that for March 2014 [25], indicating that seasonal variations of the temperature were slight at the tomography site, which was located in the tropical sea. Thus, we assume that the 2014 data approximated the temperature profile on June 2016.

Table 3.1 Summary of the mean water depths and station-to-station distances. [24]

Station Name	S1	S3	S5	S7
Mean Depth (m)	4	10	14	27
Transmission Path	S1S5	S1S7	S3S5	S3S7
Distance	4031	4457	4944	6199

A 10-kHz carrier modulated by three periods (1023 digits x 3 cycles = 0.921 s) of a 10^{th}-order M sequence was transmitted coherently with different codes every minute from all transducers at a time synchronized with 1-Hz and 10-MHz clock signals from

the GPS. The parameters for the sound transmission are presented in **Table 3.2**. By cross-correlating the received signals with one period of the M sequence used in the transmission, the signal-to-noise ratio (SNR) of the received signals was significantly increased (by 10log (2^{10}-1) = 30.1 dB), in accordance with the error theory based on the central limit theorem in statistics . A detailed explanation of the M sequence can be found in previous papers [54, 18].

Table 3.2 Summary of the sound transmission parameters. [24]

Carrier frequency	10 kHz
Cycle/digit	3
Order of M sequence	10
Code of M sequence	1-5 for stations S1-S5, respectively.
Number of repetition of M sequence	3
Repetition rate	1 min
Pulse length	0.921 s
Sound source level	192 dB re 1 μPa at 1 m

Using moving average data were resampled at 10-min intervals to remove high-frequency noise and further increase the SNR of the received signals by 10log(10)=10 dB. After the conversion of differential travel times into RACs, the 10-min interval current data were decomposed into two-period bands using a 6-h low-pass filter (LPF) and a 10-min–6-h bandpass filter (BPF). The currents retrieved by the LPF are

hereinafter denoted as the M2-band currents (with a period of approximately 12 h), and the 3-h oscillation retrieved by the BPF is hereinafter denoted as the M8-band current (with a period of approximately 3 h).

3.3 Methods

3.3.1 Ray Simulation

Fig. 3.2 shows a range-independent ray simulation results based on the one-point sound-speed profile computed using 2014 CTD data. In the simulation, the sea-surface roughness and the fine topography of the seafloor were not taken into account. Furthermore, absorption losses during the sound transmission and reflection losses at the sea surface and seafloor were not considered.

The simulated rays were bundled in groups with average arrival times closest to the observed arrival times, as shown in **Fig. 3.2**. In each group, the first arrival is marked by red ink. Although the observed first arrival times were delayed by several milliseconds to the simulated ones, no distance correction was performed in this study. The shift of the arrival times did not produce a significant error in the current measurement because it was canceled in calculating differential travel times from the reciprocal transmission data.

3.3.2 Multi-Arrival Peak Identification

In the received data, there were several significant arrival peaks with SNRs of > 35 dB. We focused on the first arrival peak, which corresponded to a ray with multiple reflections at the surface and bottom. A method proposed by Chen et al. (2019) was adopted to identify the first arrival peak among the multiple arrival peaks.

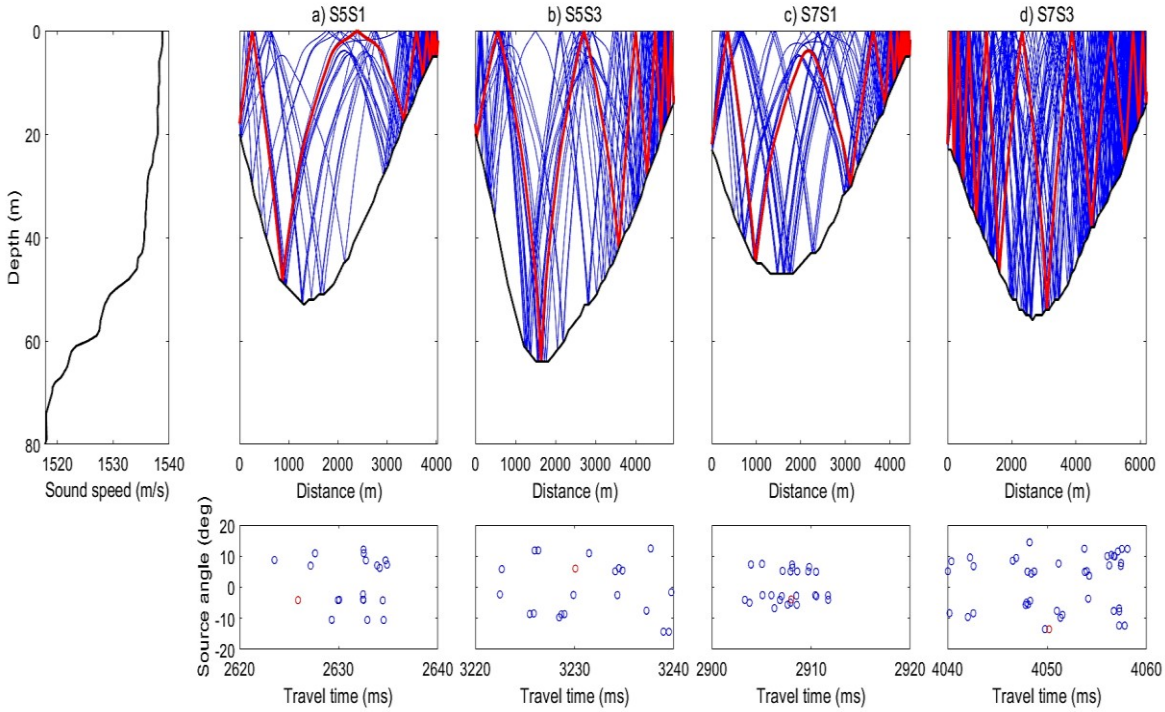

Fig. 3.2 Results of the range-independent ray simulation using 2014 CTD data [24]

First, the largest arrival peak with SNR >35 was determined within each 2-ms-wide timespan and circled with different colors, as shown in **Fig. 3.3(a)**. Second, the largest arrival peaks with a smooth timewise sequence were traced considering the neighboring timespans, and red colors were allocated to the sequential first arrival peaks, as shown in **Fig. 3.3(b)**.

Semidiurnal fluctuations were visible for the southernmost transmission paths S1S7 and S7S1. The semidiurnal fluctuations for the other six transmission paths were significantly disturbed, indicating the generation of a localized dynamic phenomenon in the region north of transmission path S1S7.

The length of the acquired data was the smallest for the S3-related data because the strong current tilted the transducer. Nevertheless, it was possible to obtain 30-h data along all four transmission paths, including the entire day of June 2nd, 2016.

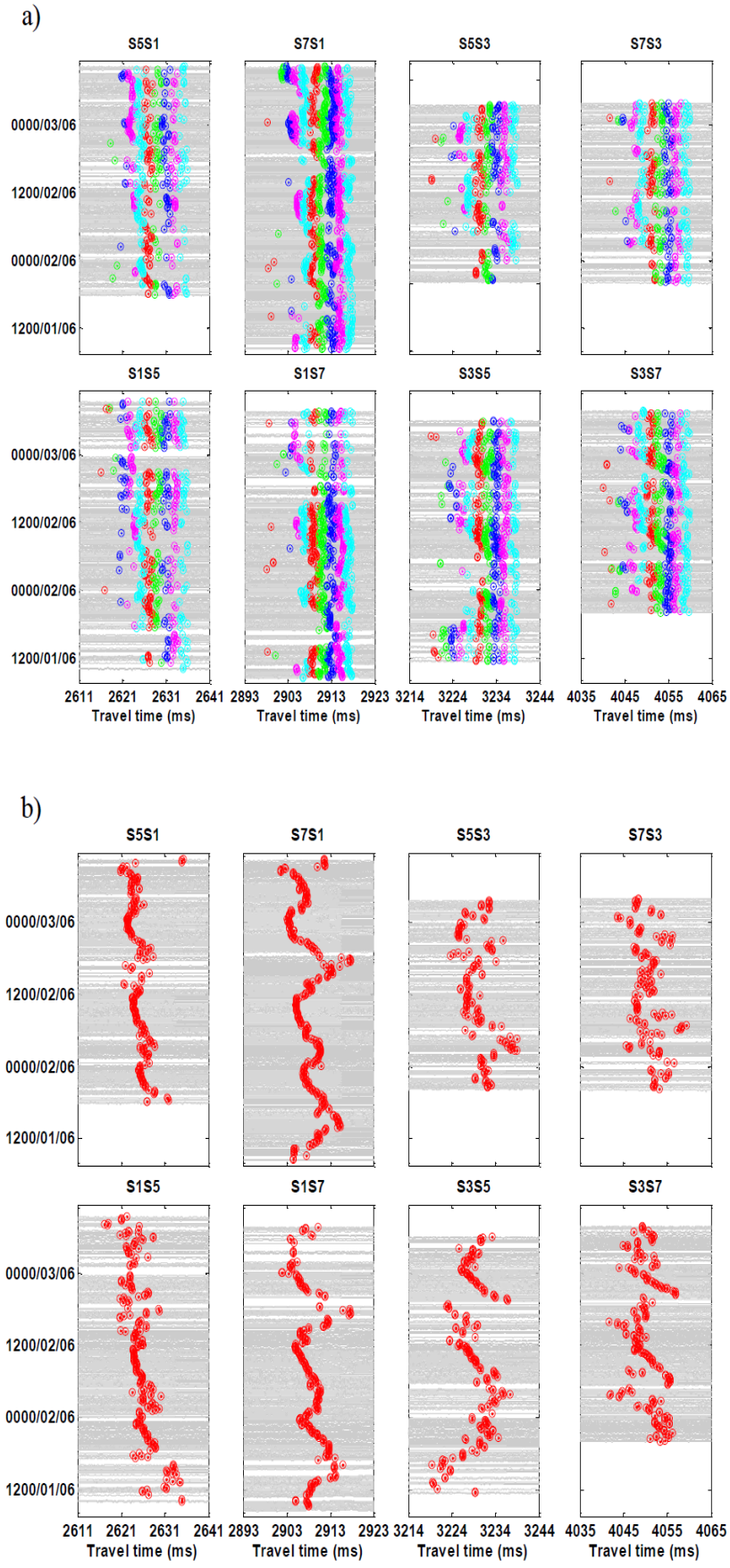

Fig. 3.3 (a) Multi-arrival peak; (b) Result of multi-arrival peak identification [24]

3.3.3 RAC and associated errors

The positive current for V_{12} is taken from T1 to T2, i.e., from the station with the smaller number to the station with the larger number. This rule is also adopted for the RACs along other transmission paths, i.e., S1S7, S3S5, and S3S7. When C_m is removed from the coupled Eqs. (2.26) and (2.27), the calculation of V_{12} is using the equation (2.28).

The errors for the differential travel times Δt_{err} were calculated using the standard deviation of the travel-time variations in a high-frequency band of 1–10 min, and Δt_{err} was 0.15, 0.34, and 0.43 ms for S1S7, S3S5, and S3S7, respectively. When Δt_{err} was substituted into Δt of equation (2.28), the velocity error V_{err} was obtained for each of the four transmission lines. It ranged from 0.04 ms-1 for S1S7 to 0.08 ms-1 for S3S5 and S3S7, and the average error was 0.07 ms-1.

3.3.4 North-east currents

The east and north current components (V_E and V_N) were calculated using RACs V15 and V37 obtained for the two transmission lines S1S5 and S3S7. The east current component (V_E) could be calculated using the equation (2.57) and the north current component (V_N) using the equation (2.58). As for the other two transmission-line pairs, S1S5/S1S7 (V15 and V17) and S1S5/S3S5 (V15 and V17) were calculated with similar procedure using different angle.

3.4 Results

The SSH data at S7 and RACs V15, V17, V35 and V37 along the four transmission lines S1S5, S1S7, S3S5 and S3S7, respectively, are plotted in **Fig. 3.4** with respect to

time. The SSH data exhibited a variation pattern combined with the semidiurnal and diurnal tides. In the M2 band, V17, V35 and V37 oscillated with periods of about 12 hours except for V15. V15 was lower than the other three RACs, indicating that the M2 tidal currents oscillated north-to-south, particularly in the first half (00:00–12:00) of June 2. V37 had a positive peak of 0.56 ms^{-1} at the first low water in the SSH variation, as indicated with Arrow-①. This SSH-current phase relation was broken at the first high water (Arrow-②). The amplitude of V37 damped in the second half (12:00–24:00) of the day. The phase of V35 had a similarity to that of V37 at the first half of the day, but both the currents constructed different variations at the second half of the day.

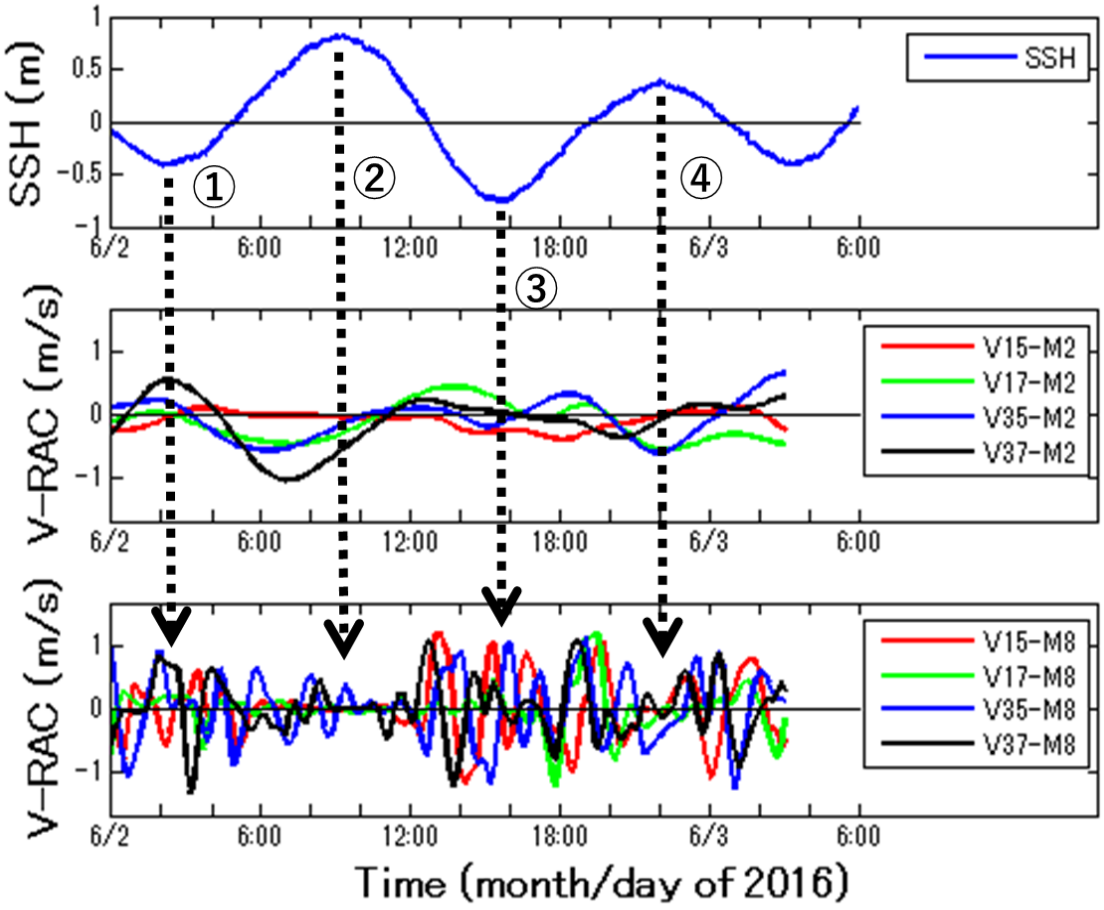

Fig. 3.4 SSH and RAC for all stations with both period-ranges time series [24]

In the M8 band, V15, V35, and V37 exhibited a pattern featuring an oscillation with a period of approximately 3 h embedded in a semidiurnal envelope oscillation. V17 was weak, particularly in the first half of the day. The semidiurnal envelope oscillated in the range of –1.2 to +1.4 ms^{-1} and peaked at the first low water (Arrow-①) and the second low water (Arrow-③). The envelope became approximately zero at the first and second high waters (Arrow-② and Arrow-④, respectively).

The averages of the eastward and northward currents, (V_E and V_N) calculated from three pairs of RACs (V15/V17, V15/V37 and V15/V35) are plotted in **Fig. 3.5** with respect to time for the M2 and M8 bands. SSH data obtained at S7 by the pressure sensor are also plotted in the top panel of the same figure. For the M2 band, the V_N current (with an amplitude of approximately 1.0 ms^{-1}) was significantly stronger than the V_E current (with an amplitude of approximately 0.3 ms^{-1}), implying that the current oscillation direction was close to north-to-south. The V_N current was close to zero at the first low water (Arrow-①) and peaked at the second high water (Arrow-④), implying a transition of the M2 tidal waves from the standing-wave to progressive-wave type. In both the V_E and V_N currents for the M8 band, the 3-h oscillation, which was embedded in the semidiurnal envelope oscillation, peaked at approximately low water (Arrow-① and Arrow-③) and diminished at high water (Arrow-② and Arrow-④). The amplitude of the 3-h oscillation was comparable for the V_E and V_N currents. Furthermore, the V_E current for the 3-h oscillation exceeded that for the M2 current particularly in the second half of the day. The V_N current for the 3-h oscillation was comparable to that for the M2 current.

3.5 Unique Current Oscillation in the Strait

Significant 3-h oscillation was observed at the northern part of the Bali Strait. It was embedded in a semidiurnal envelope oscillation which indicating that it was synchronized with the semidiurnal tides. However, the envelope oscillation transferred no energy and was featured by the gradual change of the amplitude of the 3-h oscillation, indicating that the M2 energy was filtered out in the M8 band.

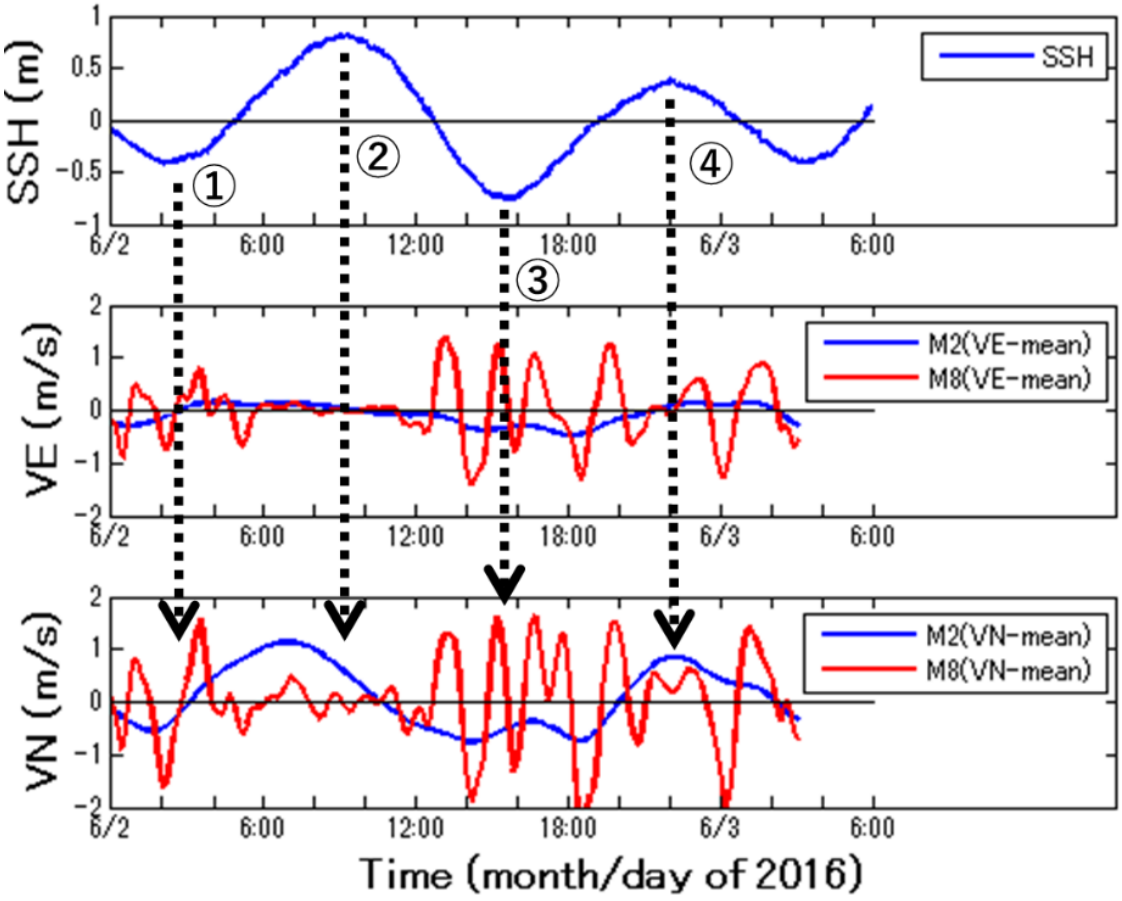

Fig. 3.5 SSH and the average of all station of east and north current component for both period-ranges time series [24]

The M8 nonlinear tide with a period of 3.10 h was a plausible candidate for the 3-h oscillation. However, the other nonlinear tides M3, M4, M6 with periods of 8.28, 6.21,

and 4.14 h, respectively, which are more significant phenomena in shelf seas, did not exist in the observed data. These nonlinear tides are usually weaker than M2 tides, as previously reported [55, 56, 46]. Furthermore, little evidence of the 3-h oscillation was observed in the SSH data obtained at S7. This suggests that the 3-h oscillation was an internal-mode phenomenon.

Internal seiches or surges generated in the region between the east and west coasts around the observation site were also candidates for explaining the 3-h oscillation. They are usually observed in the lake within an enclosed region [57]. The 3-h oscillation was pronounced in the RAC for S1S5 perpendicular to the coasts extending north-to-south on both sides of the strait, suggesting a generation of seiches. The reflection of the tidal waves by the bending coast (line A-B in **Figure 3.1 (c)**) northeast of the observation site may have played a critical role in the generation of cross-strait internal seiche modes. The period of the n^{th} mode internal seiches generated in a strait of width L is calculated as follows

$$T_i^{(n)} = \frac{2L/n}{c_i} \qquad (3.1)$$

where $T_i^{(n)}$, represents the period of the internal seiche with the i^{th}, internal mode, and n^{th}, seiche mode, and c_i, represents the phase speed of the i^{th} internal mode.

The phase speed of the 1st internal mode was estimated as c_1=0.56 ms^{-1} via dynamic mode analysis using CTD data obtained at C2 in 2014. For the channel width of L = 6 km, the wavelengths of the seiches were $\lambda_1 = 2L$ = 12 km for the 1st seiche mode and $\lambda_2 = L$ = 6 km for the 2nd seiche mode. Thus, the period was $T_1^{(1)} = \lambda_1/c_1$ = 6.0 h for the 1st seiche mode and $T_1^{(2)} = \lambda_2/c_1$ = 3.0 h for the 2nd seiche mode. This result provides evidence that the 3-h oscillation generated at the northern part of the Bali Strait

was the internal seiche with the 1st internal mode and the 2nd seiche mode. The slight sea surface undulation caused by interfacial movements in the internal seiche is consistent with the lack of evidence of the 3-h oscillation in the SSH data obtained at the observation site. However, the foregoing internal-seiche theory assumes parallel coastlines on both sides of the strait and a flat bottom. Thus, the seiche periods and modes may be modified when actual coastline shapes and bottom topographies are taken into consideration in a simulation. Modeling works are needed to simulate the generation of the internal seiches better.

3.6 Conclusions

A strong 3-h oscillation was observed at the northern part of the Bali Strait. The 3-h oscillation was synchronized with the M2 tides such that it peaked around low water and diminished at high water. The 3-h oscillations were dominant at the three transmission paths S1S5, S3S5 and S3S7 southwest of the coast A-B, and not extended to S1S7 at the southernmost site. This suggest that the 3-h oscillation was generated in the region north of S1S5 by the reflection of the M2 tidal waves at the coast A-B.

In the M2 band, the V_N current was significantly greater than the V_E current, implying the north-south oscillation of the tidal currents. SSH and current phase relation showed a transition from the standing-wave to progressive-wave type during the observation day. In the M8 band, the amplitude of oscillation was comparable to that of the M2 tidal current. The V_E-current amplitude was close to the V_N-current amplitude. The error velocity V_{err} calculated from the differential travel-time variations in the high-frequency band (10 min–1 h) was 0.07 ms^{-1}. The error was significantly smaller than the amplitudes

of both the M2 tidal current and the 3-h oscillation, showing the reliability of the data obtained in the present observations.

The strong and highly variable 3-h oscillation, which occurs in the northern part of the Bali Strait and causes problems with ferry operation, was measured for the first time using a CAT array. Although the generation of the 3-h oscillation was discussed in relation to nonlinear tides and internal seiches, it was not possible to elucidate its dynamic generation.

CHAPTER 4 SPATIOTEMPORAL MEASUREMENT FOR STRONG CURRENT FIELDS IN A FERRY ROUTE USING COASTAL ACOUSTIC TOMOGRAPHY

4.1 Introduction

The shipping industry has always been supporting global and local trades, as well as transportation. The growth of shipping activities enhanced the concern of ship accidents due to those destructive impacts corresponding to fatalities, economic losses, various environmental damages and contaminations. Many ship accidents caused by severe sea states such as varying strong current. The spatiotemporal wave-current fields on the busy shipping routes including ferry routes could be useful to reduce the ship accidents.

Since it is always prohibited to operate shipboard and moored ADCPs around ferry routes, a new approach is required to measure the temporal variation of current fields. Coastal acoustic tomography (CAT) system which has been proposed as a coastal-sea application of ocean acoustic tomography (OAT) is a prosperous candidate of the new method. Current structures in the coastal seas can be measured continuously around ports, bays, straits, and inland seas without disturbing the shipping activities, ferry boat transportation, fishery activities, and marine aquaculture industries [58, 26, 27].The accuracy of CAT data has already been adequately validated with ADCP and CTD data which attempted in coastal seas around Japan [19, 20, 21] and China [48].

This study focuses on Bali Strait located between Java and Bali islands in Indonesia, which faces to the Flores Sea and the Madura Strait through a very narrow channel of width 2 km at the northern end, and broaden southward, forming a funnel shape, towards an exit of width 60 km to the Indian Ocean as shown in **Fig 4.1**. The ferry route across the experiment site located at the north side of Bali Strait, which has essential roles to connect Java and Bali Islands as the main lane for transportation, logistic distribution

between both islands and as an access to enter the Nusa Tenggara islands. Some ferry routes are so busy, for example, Ketapang port to Java Island, Gilimanuk port to Bali Island, as we could see in the **Fig. 4.2**. Ship accidents sometimes occur at a typical narrow channel of width 5 km in the northern part of the Bali Strait.

This study proposes and examines a spatiotemporal mapping technique to visualize strong current fields in a ferry route using the CAT to reduce ship accidents and to enables for realizing real-time monitoring of varying strong current fields.

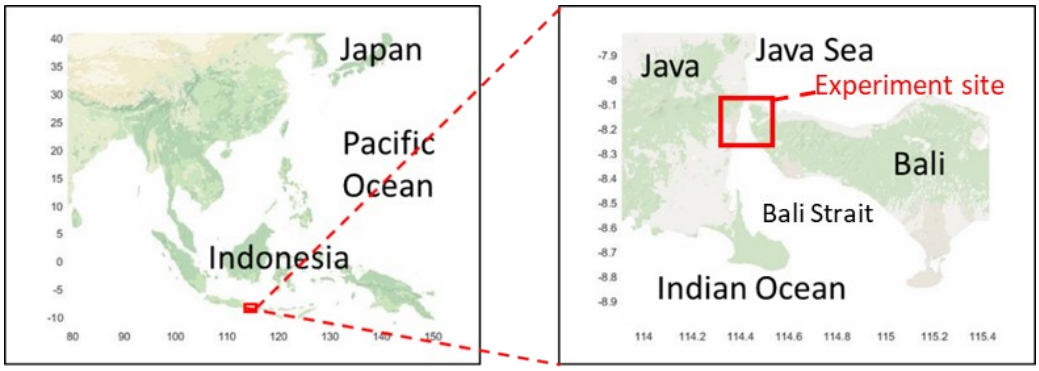

Fig. 4.1 Tomography site, the Bali Strait in Indonesia [59]

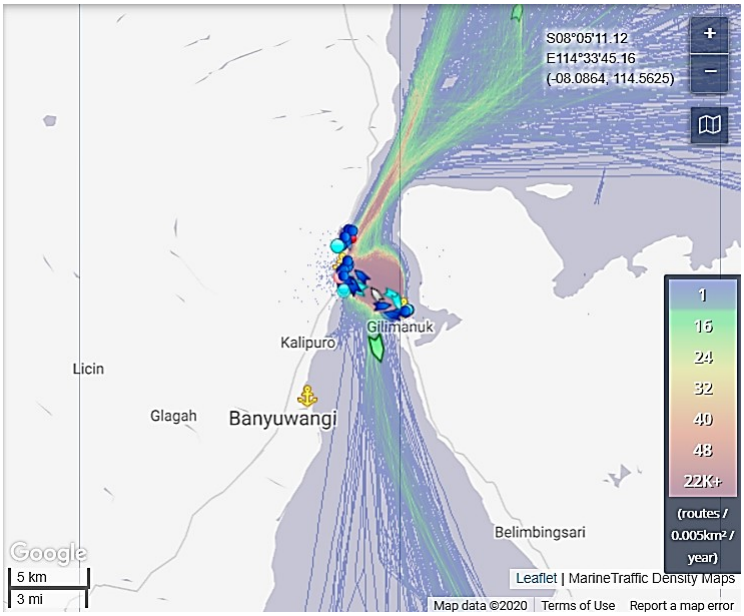

Fig. 4.2 Density map of shipping traffic around the northern Bali Strait in 2016

(Source: www.marinetraffic.com)

4.2 Experiment Design

A CAT experiment was carried out during June 1-3, 2016, at northern part of the Bali Strait around the ferry route, which connects Java and Bali Islands. Four land-based CAT systems were deployed on both sides of the strait, two stations near Java Island (S1 and S3) and the other two stations near Bali Island (S5 and S7), as shown in **Fig. 4.3**. The S1 station was set at the edge of the jetty in a resort hotel and S3 station at the edge of the wharf in a port. The S5 station was at the offshore tower of submarine electric cable and S7 station was at the abandoned offshore platform of the natural gas pipeline. Station-to-station distances were 4,031 m for S1-S5, 4457 m for S1-S7, 4944 m for S3-S5, and 6199 m for S3-S7, determined from the GPS positions.

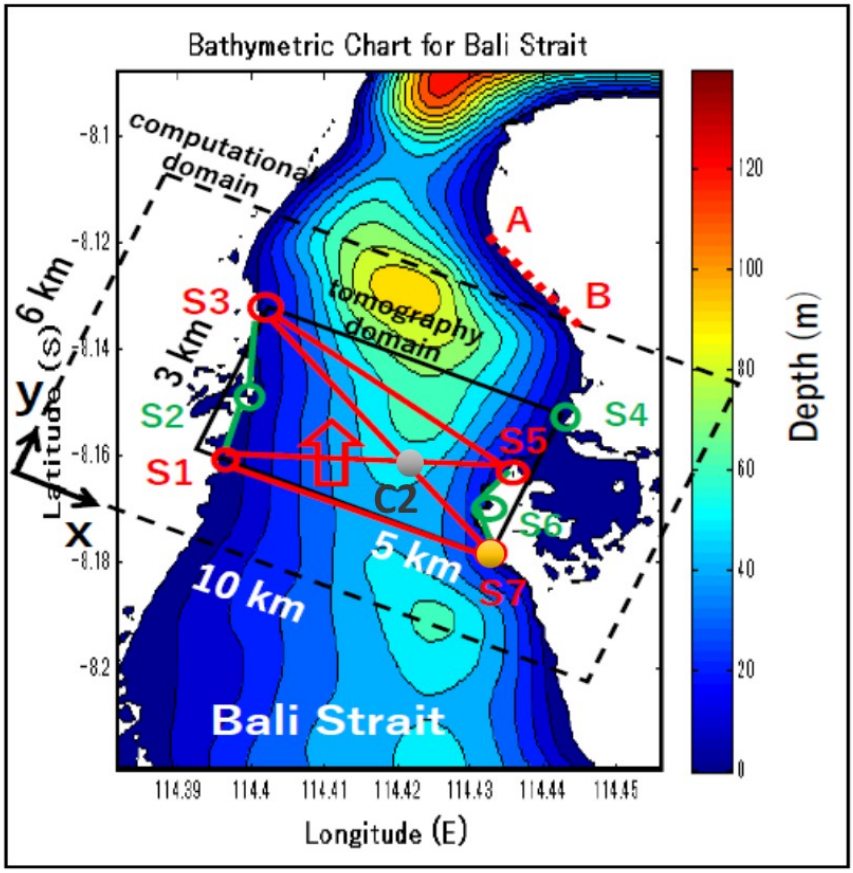

Fig. 4.3 Experimental design [60]

Tidal waves entered the tomography site from the south in the direction perpendicular roughly to S1-S5, as shown as a red arrow in **Fig. 4.3**. A pressure sensor was attached to the suspension rope near the transducer at S7 station for measuring the variation of sea surface height (SSH) (as a yellow dot in **Fig. 4.3**). The CTD data were obtained at the gray dot of **Fig. 4.3** in March 2014. The tomography domain is shown as a solid rectangle of 5 km x 3 km in **Fig. 4.3**. The red circles and straight lines in the tomography domain show the acoustic stations and sound-transmission lines, respectively. Green circles and lines are the virtual stations and artificial straight coasts, respectively. The computational domain is shown as a dash-rectangle of 10 km x 6 km in **Fig. 4.3**. The dash red-line at the northwest coast of Bali Island is highlighted to pay attention to the reflection of tidal waves. A red arrow perpendicular to S1S7 shows the propagation direction of tidal waves. Bathymetric data were obtained from the Marine Geoscience Data System (MGDS). The maximum depth of the basin was approximately 90m in the big scouring hole near the east side of S3 station.

4.3 Methods

4.3.1 Range Average Current

The travel time equation as written in Eq. (2.14) could be simplified as the real ray path projected to the horizontal plane as shown in **Fig. 2.11**, those are Eqs. (2.26) and (2.27). Moreover, the current velocity and sound speed could be calculated using the Eqs. (2.28) and (2.29), respectively.

4.3.2 Northward and Eastward Current

According to Adityawarman, *et al*. (2012), the north-east current components (V_N, V_E) of RAC are calculated from RACs obtained independently along a pair of transmission path. In this study, three pairs of north-east current components could be obtained. Those are V15-V17, V15-V37, and V15-V35 are acquired as sketched in **Fig. 4.4**. The north-east current components from V15-V37 (S1S5-S3S7) are formulated as Eqs. (2.57) and (2.58). As for the pairs V_{15}-V_{17} and V_{15}-V_{35}, the V_{37} change to V_{17} and V_{35}; θ_{37} change to θ_{17} and $\theta_{35,}$ respectively.

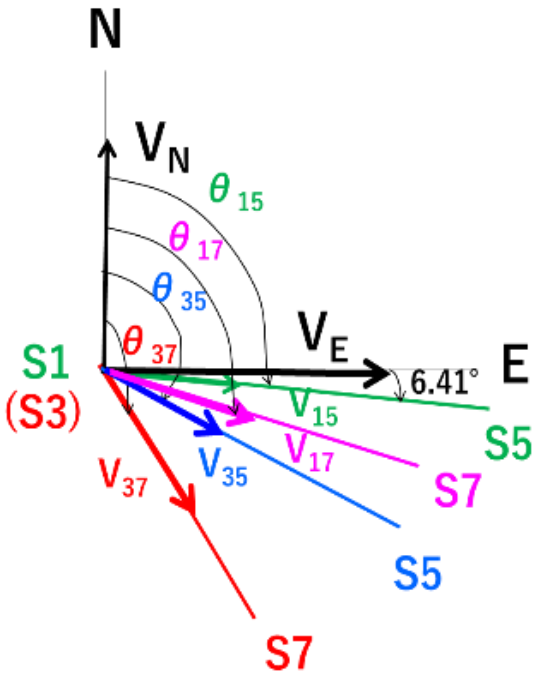

Fig. 4.4 Skecth to determine the angle (θ) for all transmission-line pairs to calculate the east-north current components [60]

4.3.3 Horizontal-slice Inversion

The differential travel time for the projected rays on a horizontal plane is written as Eq. (2.30). The inverse analysis method is to determine the unknown depth-averaged current fields on a horizontal plane or spatiotemporal current fields of $\mathbf{u}(x,y)$ from the differential travel time data. The two-dimensional current fields are related to the stream function, $\Psi(x,y)$, with $u=-\partial\Psi/\partial y$ and $v=\partial\Psi/\partial x$. Then, Ψ is expanded into a truncated Fourier function series, as written in Eq. (2.34), as two order Fourier function. The unknown coefficients, or the unknown current velocities that should be solved is 20 terms based on Eq. (2.37).

By using the differential travel time vector $\boldsymbol{y} = \{\Delta t_i\}$, the unknown coefficient vector $\boldsymbol{x}=\{Dj\}$, the transform matrix $\boldsymbol{E}=\{Eij\}$ and the travel time error vector $\boldsymbol{n}=\{nj\}$, Eq. (2.37) re-written into the matrix form as Eq. (2.42). The tapered least-squares method accompanied by the L-curve method is applied to obtain the solution [38, 19]. Three virtual stations S2, S4, and S6 are here introduced at the coast to increase data used in inversion as shown in Fig. 5. Non-slip conditions along artificial straight coasts S1S2, S2S3, S5S6 and S6S7 are newly proposed in the present paper with zero differential travel time ($y=\{\Delta t_i\}=0$) along the coasts. The conditions that no current crosses the artificial coasts S1S2, S2S3, S4S5, S5S6 and S6S7 were not applied because of less effectiveness [20]. As a result, four data are added in the column vector y on the left side of Eq. (2.42).

4.4 Results

4.4.1 Power Density

The power spectral density diagrams for the 10-min interval RAC data are shown in **Fig. 4.5** for V_{15}, V_{17}, V_{35} and V_{37}. The significant semidiurnal spectral peaks were constructed at 14.2 h for V_{17} and V_{35}; 10.7 h for V_{37}; and diminished at V_{15} perpendicular to the northward propagating M2 current. The significant spectral peaks around 3-h appeared at 3.3-h for V_{15} and 2.7 h for V_{35}. Other less prominent spectral peaks were visible at 8.5 h and 5.3 h for V_{15}, 4.7 h for V_{17}, 14.2 h and 7.1 h for V_{35}, and 5.3 h and 3.56 h for V_{37}.

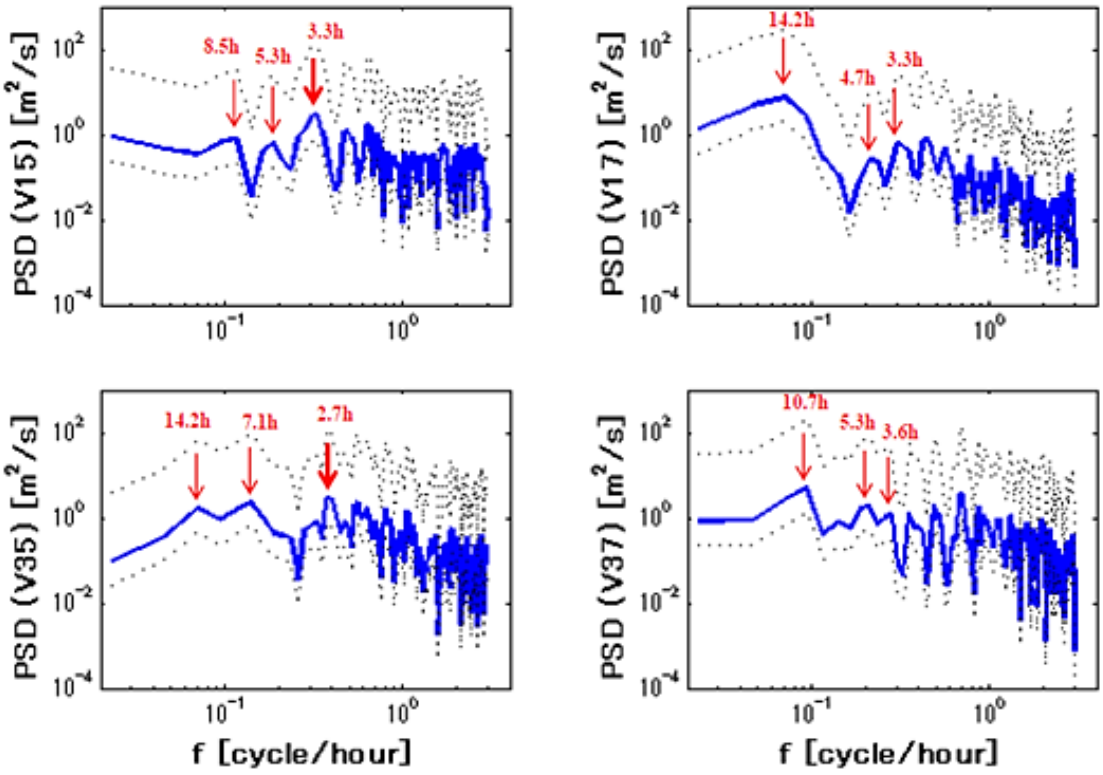

Fig. 4.5 Power spectral density diagrams for the 10-min interval RAC data [60]

4.4.2 Spatiotemporal Current Fields

The spatiotemporal of currents calculated at the different tidal phases are shown in **Figs. 4.6-4.14**, together with the sea surface height (SSH) data (upper panel). For the M2 band (middle panels), the spatiotemporal current fields are plotted at a 3-h interval from 03:00 to 12:00 on June 2. The currents at the central part of the strait were reversed from the southeast to northwest at a 6-h interval, forming a clockwise vortex (03:00, 12:00) or a counter-clockwise vortex (06:00, 09:00) on the Java side of the strait.

For the M8 band (lower panels), the inverted current fields are plotted at an hourly interval from 02:00 to 05:00 on June 2, transition phase of the SSH from the low water to mean water. The strong southeastward current at 02:00 suddenly change direction to the strong northwestward current at 03:00. This strong northwestward current was reversed southeastward one hour later (04:00). The maximum southeastward and northwestward currents reached 1.2 m/s and 0.8 m/s, respectively. The southeastward/northwestward currents induced the clockwise/counter-clockwise vortex on the Java side of the strait. The counter-clockwise vortex was also induced on the Bali side by the strong southeastward current at 02:00.

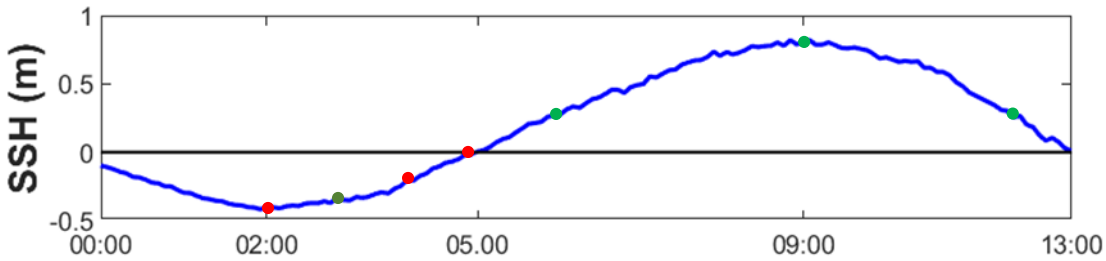

Fig. 4.6 SSH time series on June 2nd, 2016, for the first half day

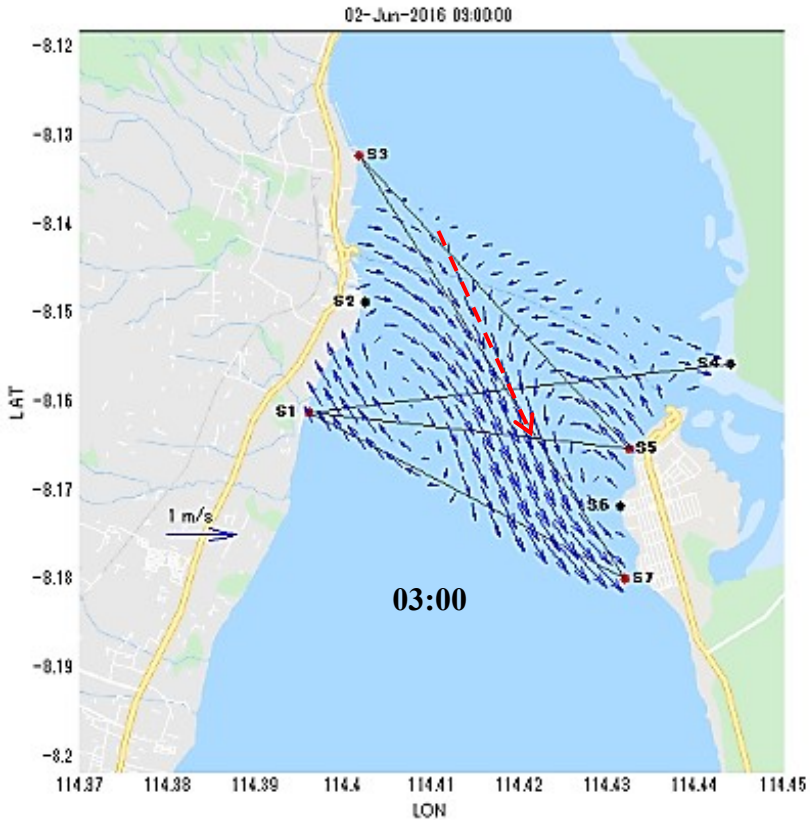

Fig. 4.7 Spatiotemporal mapping M2-band at 03:00

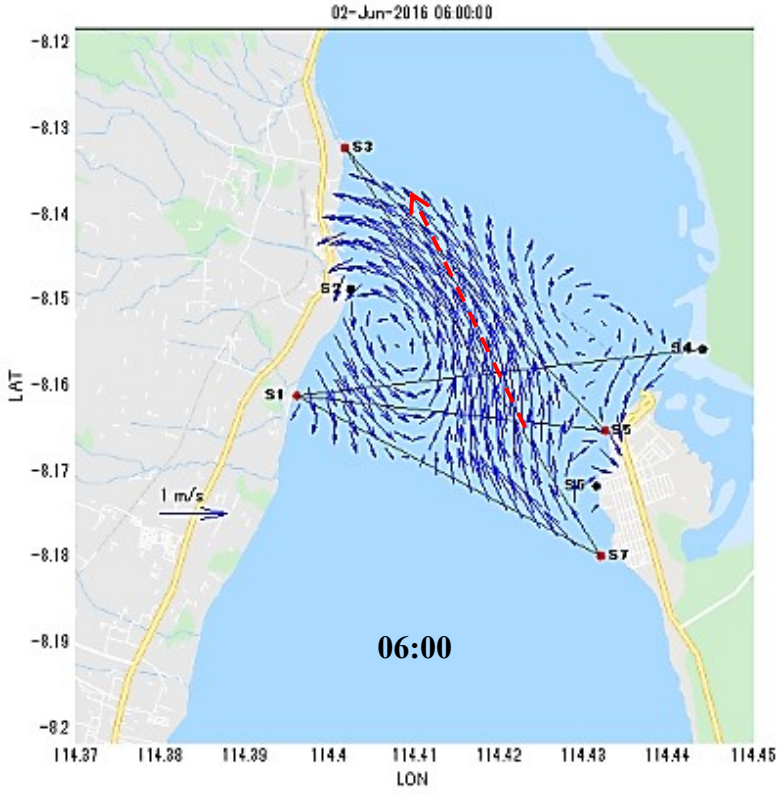

Fig. 4.8 Spatiotemporal mapping M2-band at 06:00

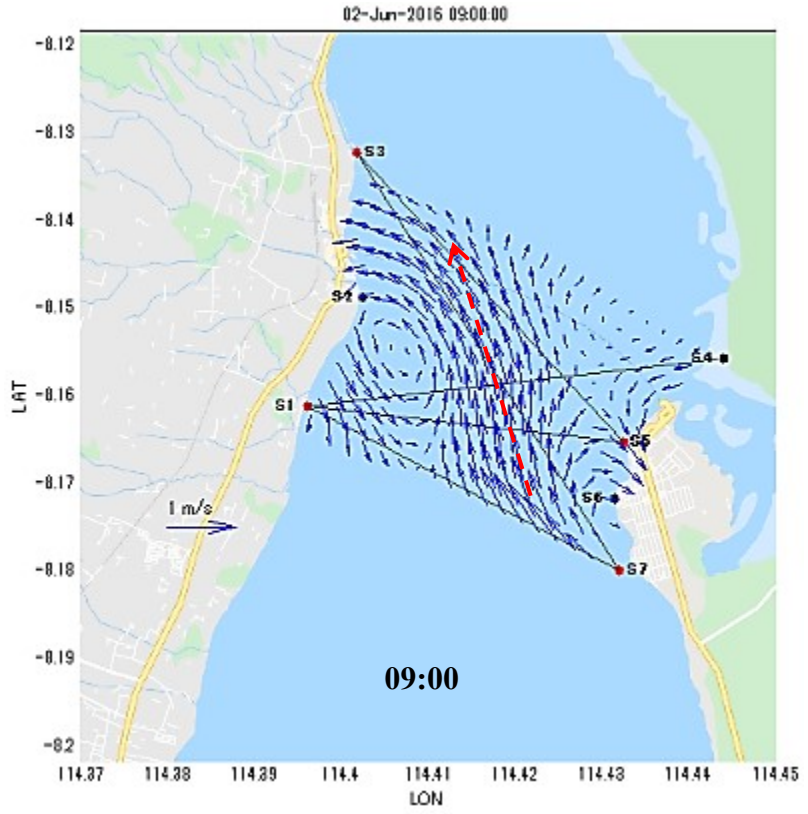

Fig. 4.9 Spatiotemporal mapping M2-band at 09:00

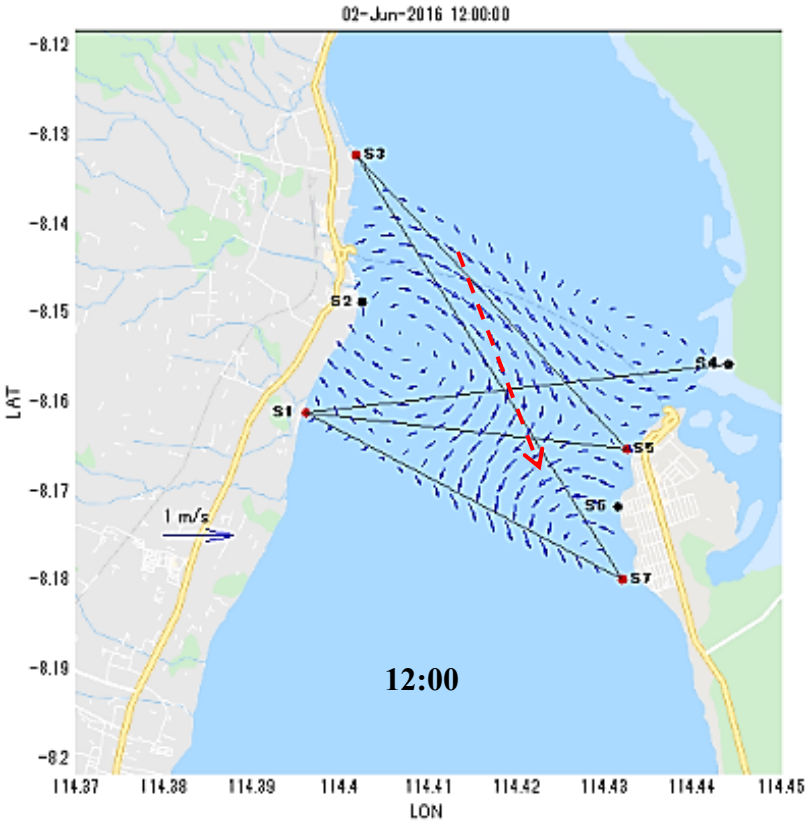

Fig. 4.10 Spatiotemporal mapping M2-band at 12:00

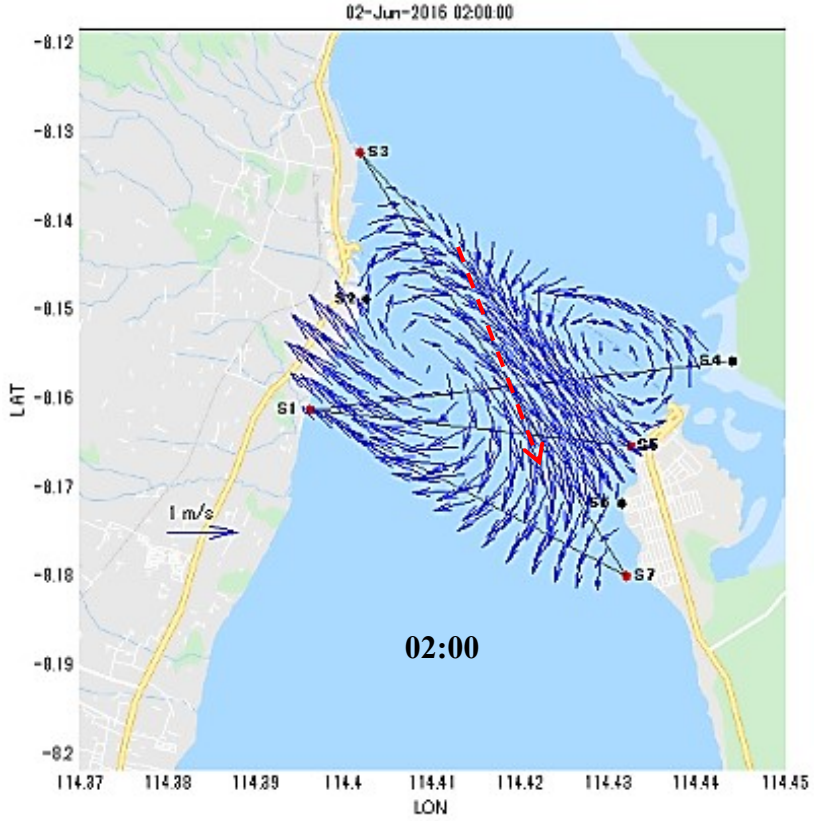

Fig. 4.11 Spatiotemporal mapping M8-band at 02:00

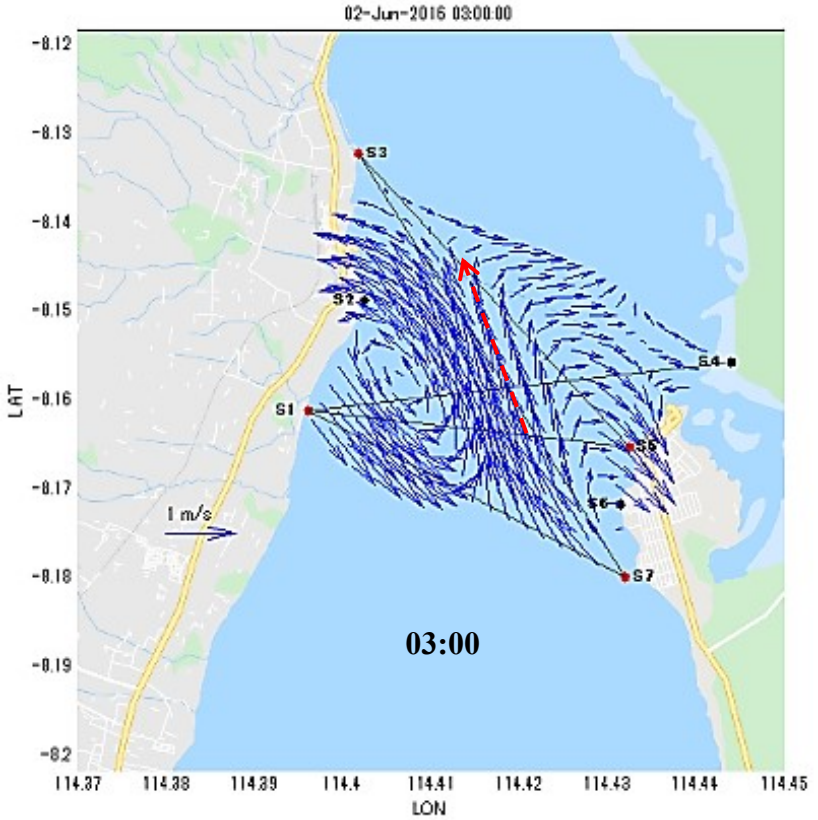

Fig. 4.12 Spatiotemporal mapping M8-band at 03:00

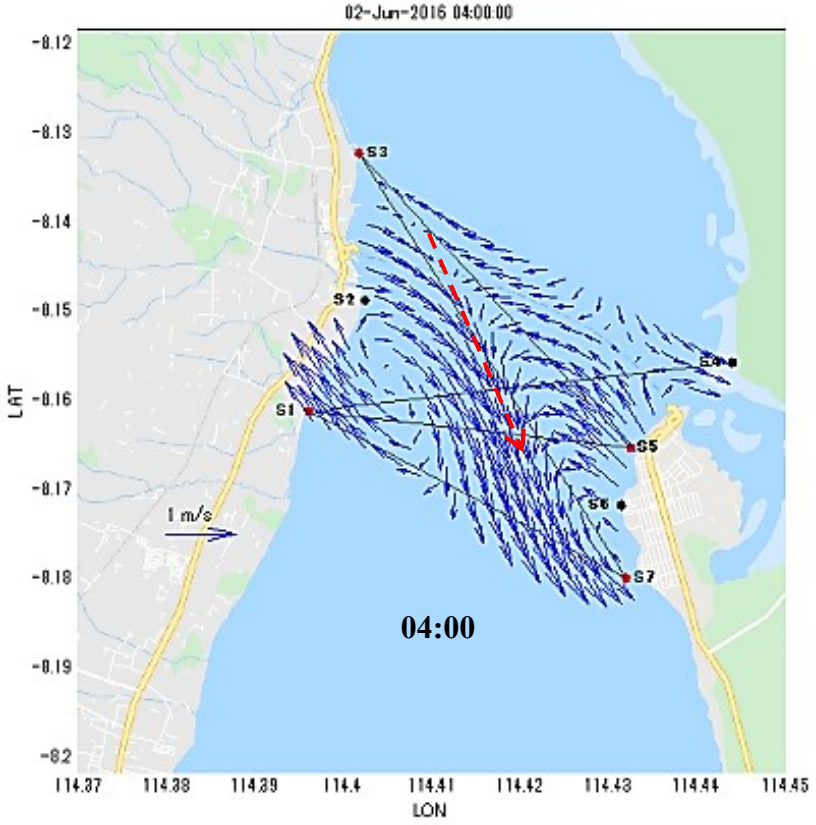

Fig. 4.13 Spatiotemporal mapping M8-band at 04:00

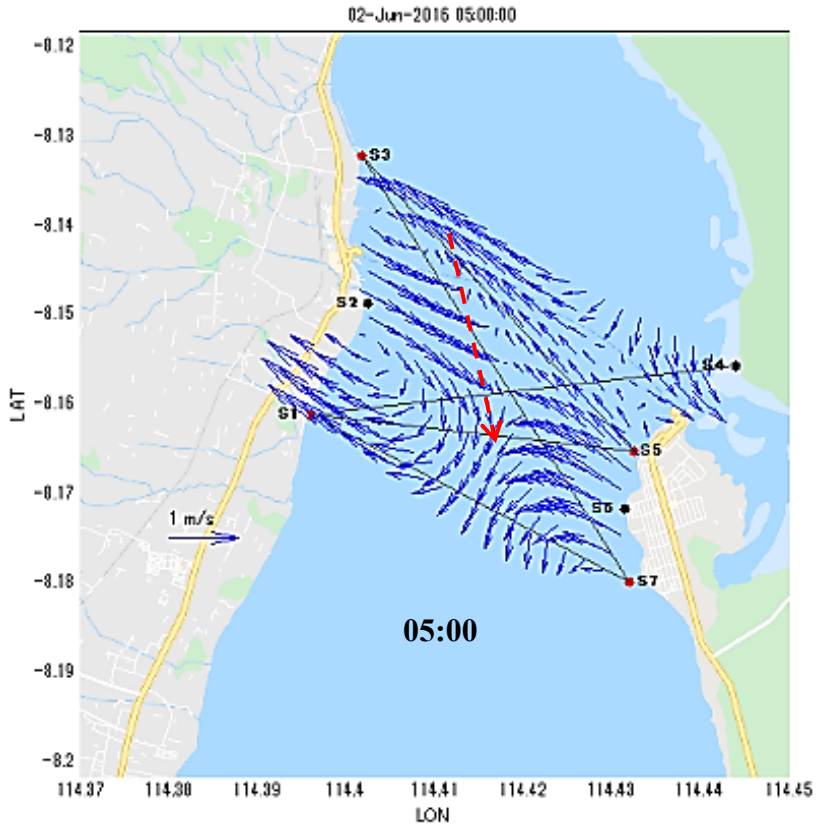

Fig. 4.14 Spatiotemporal mapping M8-band at 05:00

4.5 Discussion

4.5.1 Comparing The Pre and Post-Inversion Results

Validation of the inverted results by a repeat survey of shipboard ADCP was not realized due to strong, highly variable currents. The one validation method that possible to be done is calculating the Root-Mean-Square Differences (RMSD) for the observed and inverted RACs for all transmission lines. The range-average currents (RACs) V17, V15, V37 and V35 for transmission lines S1-S7, S1-S5, S3-S7 and S3-S5 calculated from the inverted current fields are compared with the observed range-average currents in **Figs.** (**4.15-4.22**). Root mean squares difference (RMSD) for the inverted and observed RACs is here used as an index to know inversion errors and plotted together with V_{err}, calculated from Eq. (2.48) in these figures.

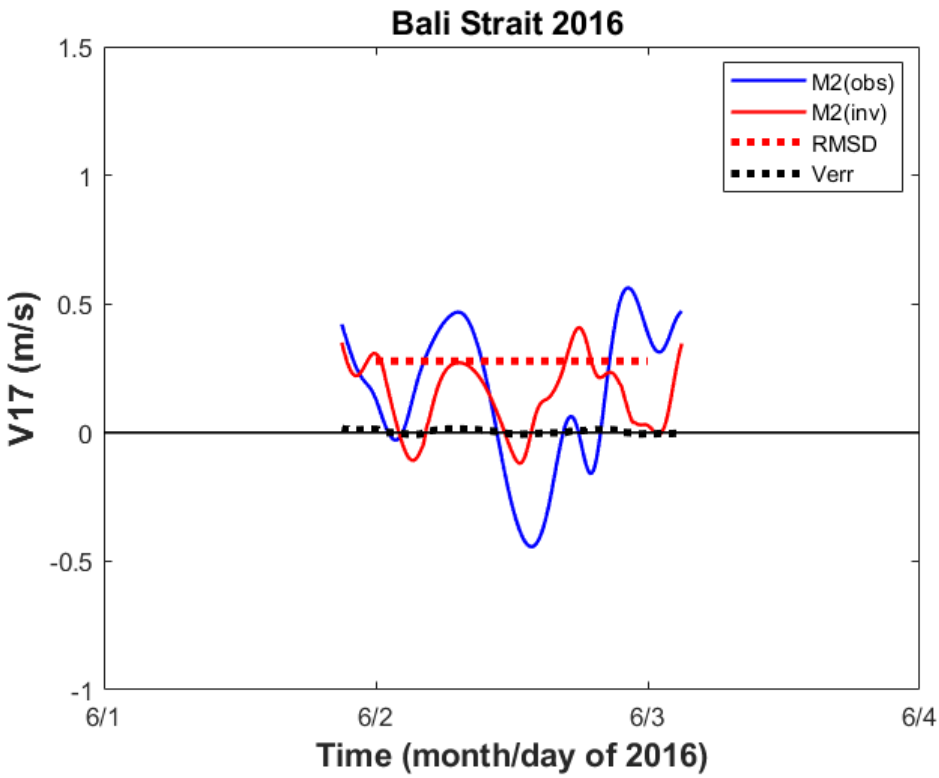

Fig. 4.15 RMSD for observed (blue line) and inverted (red line) for V17-M2 band

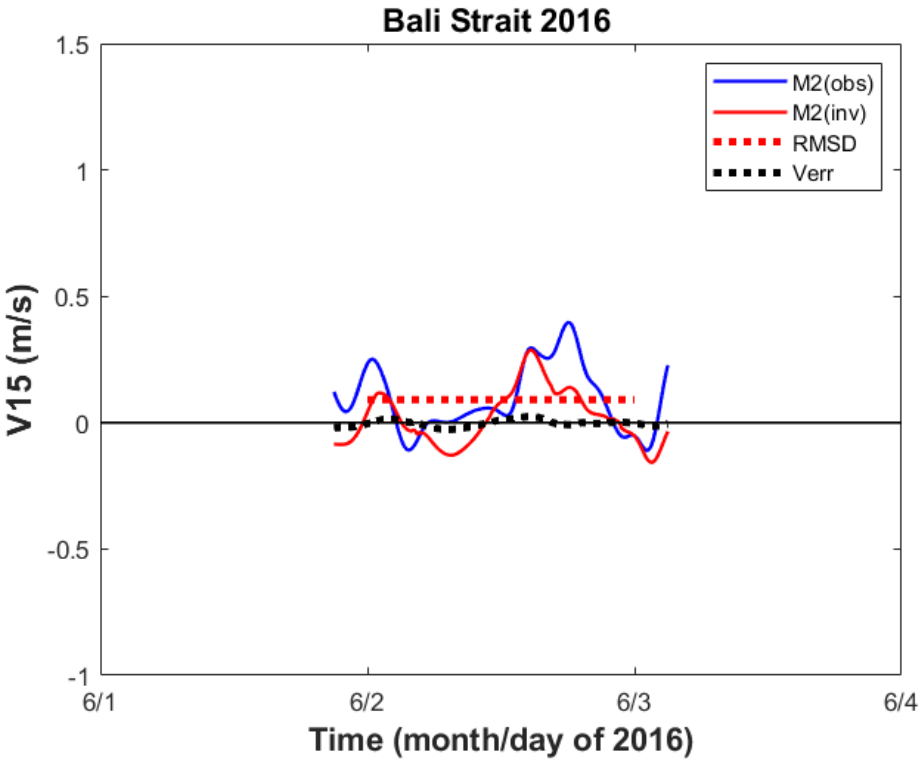

Fig. 4.16 RMSD for observed (blue line) and inverted (red line) for V15-M2 band

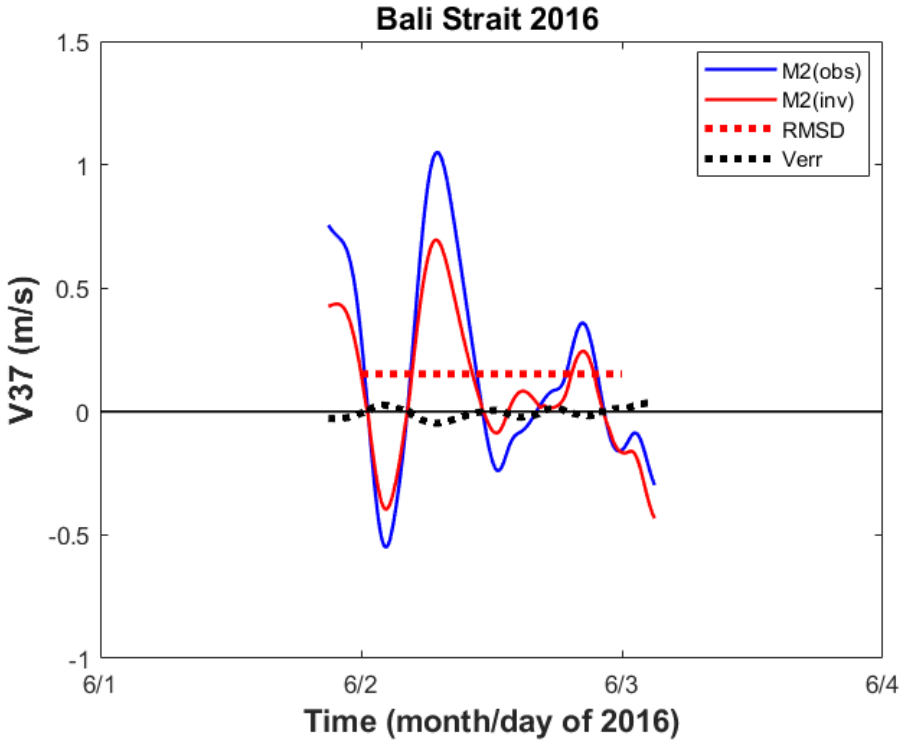

Fig. 4.17 RMSD for observed (blue line) and inverted (red line) for V37-M2 band

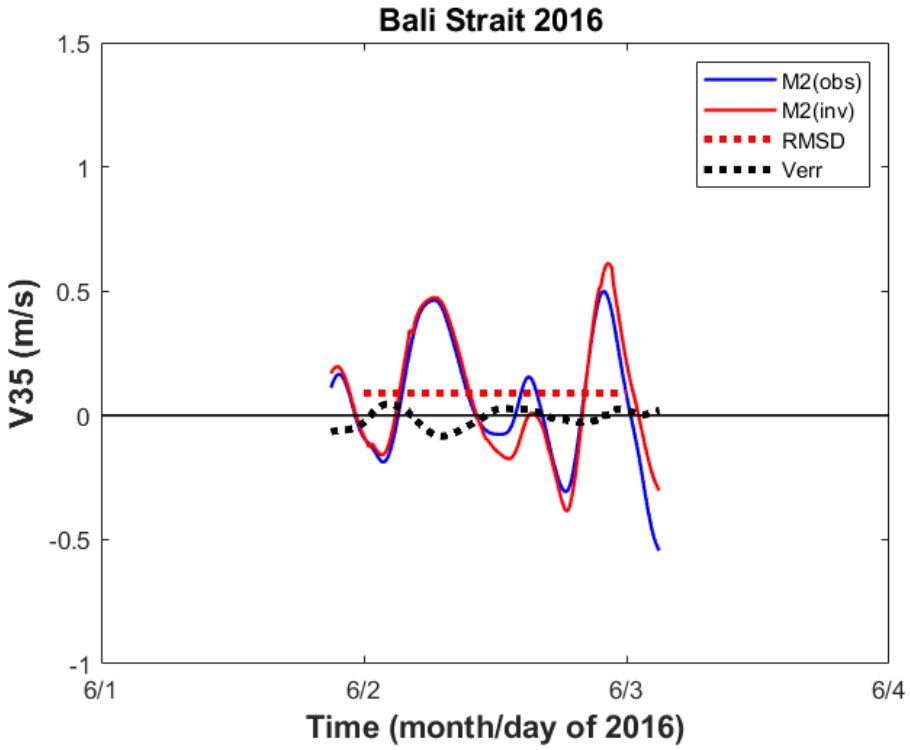

Fig. 4.18 RMSD for observed (blue line) and inverted (red line) for V35-M2 band

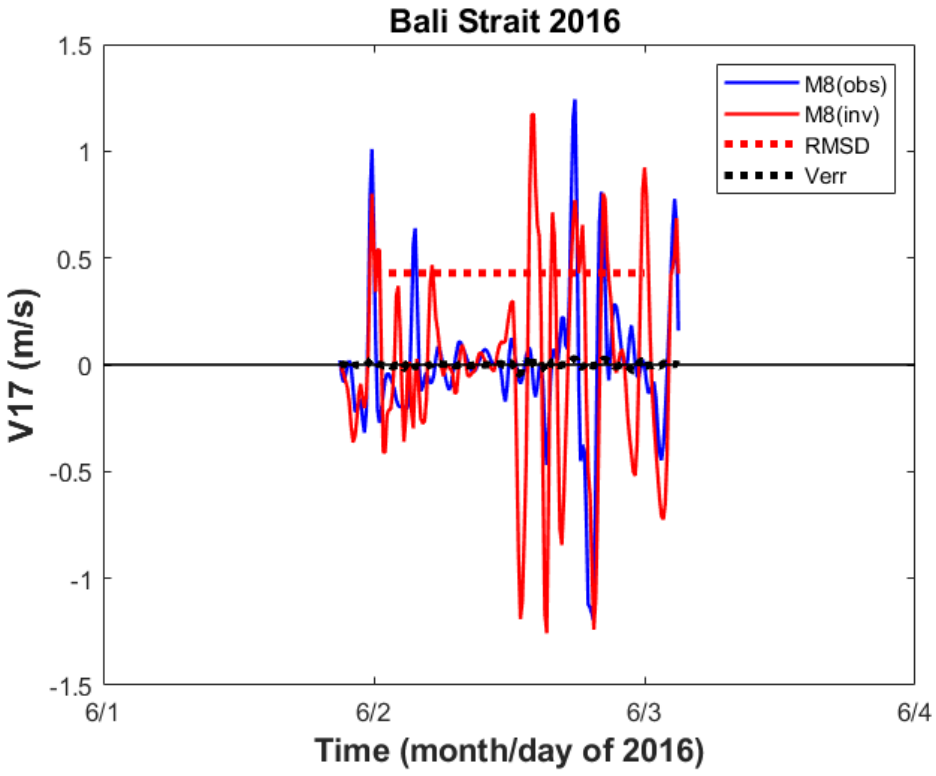

Fig. 4.19 RMSD for observed (blue line) and inverted (red line) for V17-M8 band

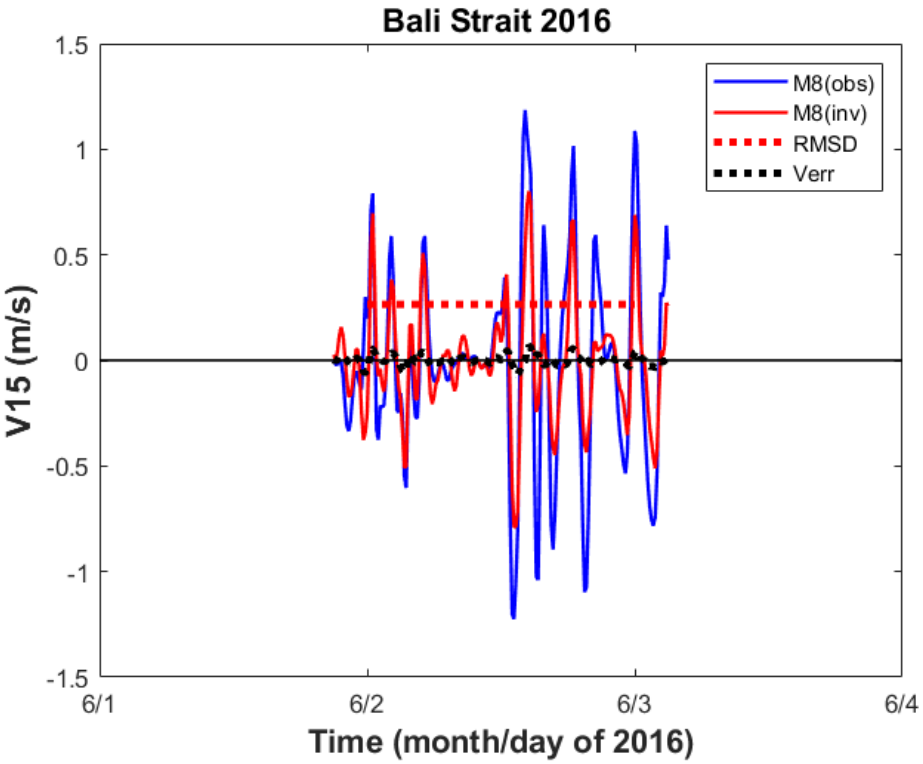

Fig. 4.20 RMSD for observed (blue line) and inverted (red line) for V15-M8 band

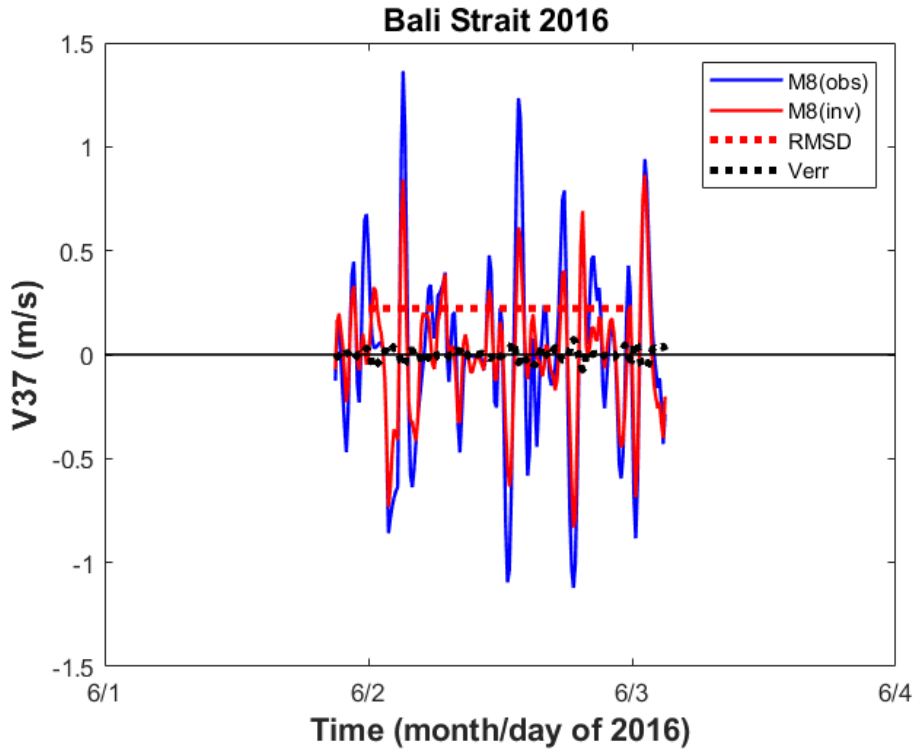

Fig. 4.21 RMSD for observed (blue line) and inverted (red line) for V37-M2 band

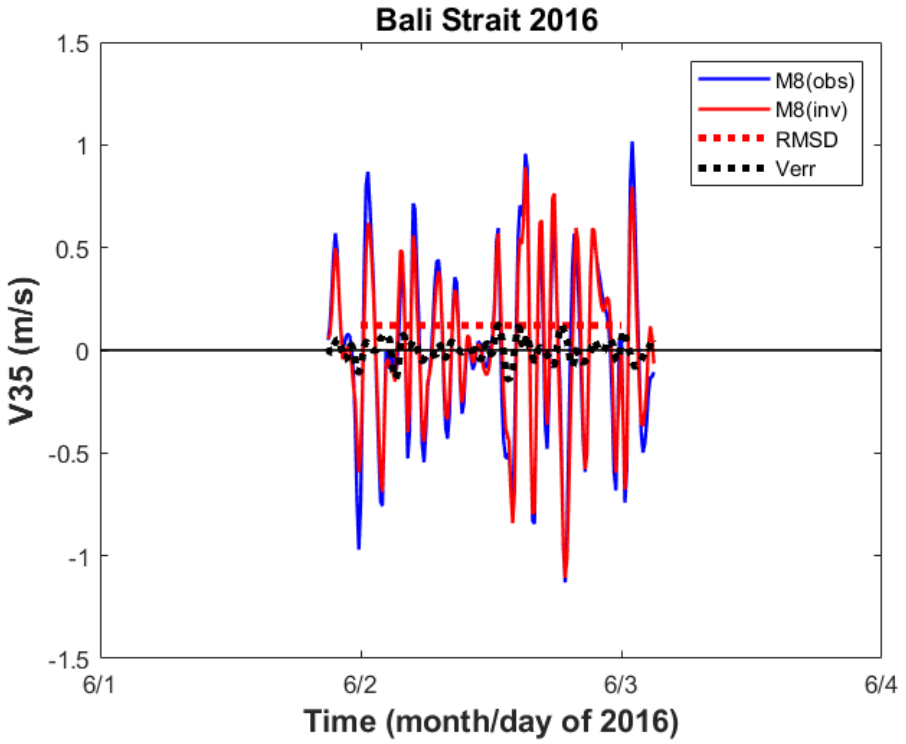

Fig. 4.22 RMSD for observed (blue line) and inverted (red line) for V35-M8 band

The Verr of all transmission lines showed less than 0.01ms^{-1} of current amplitude. It means that the error from inverse method is good and acceptable. Furthermore, RMSDs for the four transmission lines and two period bands 6h-LPF (M2 band) and 10min-6h BPF (M8 band) are presented in **Table 4.1.** RMSDs are 0.28 ms^{-1} and 0.43 ms^{-1} at maximum for the M2 and M8 bands for V17, respectively. On the other hand, RMSDs are at minimum for V35 and the minimum value is 0.09 ms^{-1} for M2 band and 0.12 ms^{-1} for M8 band. Although the phase of range-average current is in a good agreement between the observed and inverted data, a difference between the peak heights is significant, especially for V17. These big differences was suspected caused by the 3-h oscillation phenomena and the V17 transmission was perpendicular to the tidal wave direction. As the RACs results from Chapter 3, the V17 currents for

the M8 band was almost diminished for the spatiotemporal period of time (the first half-day of June 2nd).

Compared to the maximum of observation current amplitude (observed RAC amplitude), the inverted RACs showed about 40% weaker. This underestimation was happened because of the optimal solution process in the inverse method. The dumping factor and SVD process made the current velocity from each RAC balanced distribute for the all-over computation domain. Fortunately, 40% underestimation is a satisfactory result.

Table 4.1 RMSDs for the observed and inverted RACs, obtained on the four transmission lines.

		Transmission line			
		S1S7	S1S5	S3S7	S3S5
RMSD of RAC (ms^{-1})	M2 band	0.28	0.09	0.15	0.09
	M8 band	0.43	0.27	0.22	0.12

4.5.2 Characteristic of Strong Current Fields

The time series of spatiotemporal current fields in the experiment site are shown in **Figs. 4.7-4.14**. The strong current fields mostly occurred in the central of the strait with southward or northward direction for both bands. The eastward and westward current has an insignificant magnitude compared to the northward and southward current. At 03:00 near low water of SSH, the strong southward current fields

will occur in the center of the strait for both bands, and the magnitude of total currents could be over 2.0 m/s. And at 06:00, near the high water of SSH, the strong northward current will occur in the center of the strait for M2 current. The magnitude of northward current is higher than the magnitude of the southward current, which indicated a strong influence of the Indian Ocean tidal system. Furthermore, the clockwise and counter-clockwise vortex are formed on the lateral side of Java Islands. The current magnitude that generated the eddies about 0.3 m/s.

4.5.3 Relationship between Ferry Route and Strong Current

The ferry route to connect Java Island (Ketapang port) and Bali Island (Gilimanuk port) is essential as the commercial sea transportation and logistics for both islands and the Nusa Tenggara islands. As to fulfill the sea transportation role, the chosen ferry route must guarantee the high level of safety for passengers, cabin crews, and logistics (including the passenger's vehicles). As shown in **Figs. 4.6-4.14** and the analysis result from the previous subsection, the center of the spatiotemporal mapping area has strong southward and northward current. This area should be avoided by the ferry or any other ships. Because the northward current is stronger than the southward current, the ferry route should be selected at the southern side of the experiment site.

The disastrous M8 current occurred around the region surrounded by S1S5 and S3S5 as shown in **Figs. 4.11-4.12**. Furthermore, the ships connecting Ketapang Port (Java Island) and Gilimanuk Port (Bali Island) are operated in this special region with the disastrous M8 current. The ferry route is important to fulfil the sea transportation from Java Island toward Bali Island and Nusa Tenggara islands further

east. The regular operation of the ferry is severely disrupted by the strong and rapidly varying currents.

Moreover, there are several submarine cables in the Bali Strait near both ports. The purple dash lines indicate the submarine cables in **Fig. 4.23**. The chosen ferry route can ensure not to harm the submarine cables. And other symbols in **Fig. 4.23** is crossed-anchor symbols. Those mean could not put anchor around that area. In some emergencies, a ferry needs to put down its anchor. Thus, a ferry route should avoid the field with those symbols too.

The recent ferry routes are shown as a red line in **Fig. 4.23** and a blue dash line in **Fig. 4.24**. The route is inside the experiment site, between S1S5 and S3S5 transmission lines. The report informed a ferry sunk accident occurred in March 2016 [34] and newest accident in June 2021 [35]. The suggestion for a better and safe ferry route is the shifted southward by 10 km. The risk of ferry traffic is expected to be much reduced outside the region with the M8 current. However, further study is needed to get the exact best and safe ferry route.

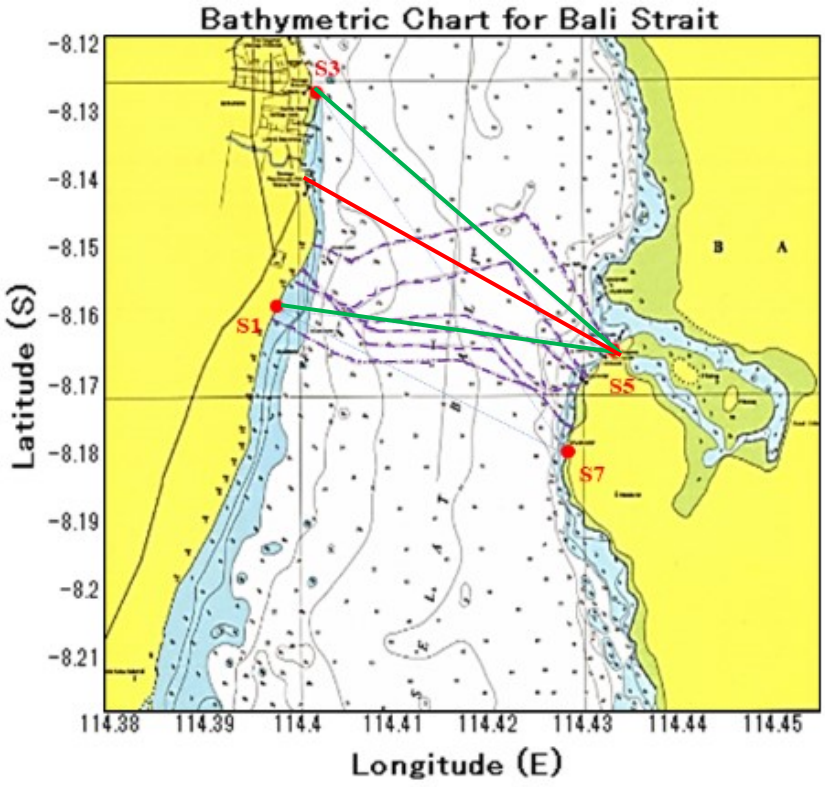

Fig. 4.23 Bathymetric map and submarine cable from Hydro-Oceanography Agency of Indonesia (PUSHIDROSAL)

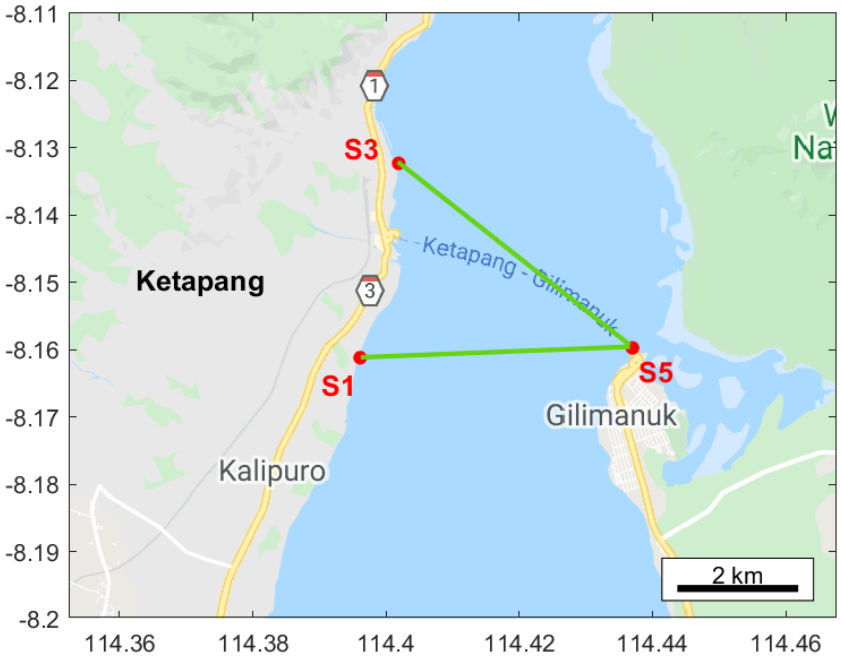

Fig. 4.24 Ketapang-Gilimanuk ferry route from google and the safest route from the spatiotemporal mapping result

4.6 Conclusions

Strong and varying current fields were observed at the northern of the Bali Strait. Power spectral density analysis showed two wave-periods are dominant, 12-h period or M2 current, and 3.7-h period or M8 current. The differential travel times data were filtered into those period bands. For the M2 current, V_N with the amplitude of approximately -1.05 ms^{-1} was much greater than V_E with the amplitude of approximately 0.3 ms^{-1}. For the M8 current, the V_E amplitude of 1.2 ms^{-1} is close to the V_N current amplitude of 2 ms^{-1}.

The RMSD and current velocity error (Verr) were done to validate the inversion accuracy. The Verr showed less than 0.01 ms^{-1} and the RMSD showed 40% underestimation. This is a satisfactory result means the spatiotemporal current field results could interpreted the tidal current distribution in the Bali Strait well.

The spatiotemporal current fields showed the maximum of total current about 2 ms^{-1}. The north-south current is dominant and stronger than the east-west current. This is because of strong influence of the Indian Ocean. A clockwise or counter-clockwise vortex was formed on the Java side. Several submarine cables exist at the bottom of the experiment site. The suggestion for a better ferry route to prevent and reduce ship accidents is shifted 10 km to the southern side of the experiment site.

CHAPTER 5 CONCLUSIONS AND FUTURE WORKS

5.1 Conclusions

A ferry boat was tilted and sunk on March 4th, 2016, while crossing Bali Strait from Gilimanuk port to the Ketapang port. A study on tidal current distribution in the Bali Strait is needed to prevent more disastrous events caused by the strong currents. Compared with other current-field measurement conventional methods, CAT is an observational method suited to use in the Bali Strait with strong and highly variable currents. By reconstructing the vertical and horizontal tidal current distribution, analysis and clarification of the tidal current characteristic could be done. Those results could be helpful to estimate a better and safe ferry route to avoid the disastrous currents.

Through all of the researches on this study, the main conclusions can be summarized as follows:

1. A CAT measurement with four acoustic stations was attempted during June 1-3, 2016 at the northern part of the Bali Strait, where a vital route of ferries is severely disturbed by a strong current varying rapidly in one hour. In chapter 2, the models and methods used for the Bali Strait case are mentioned. Those are ray simulation, range-average current, north-east current component, and horizontal-slice inversion. The ray simulation was done by using the one-point 2014 CTD data. After that, the first arrival peak could be identified to calculate the differential and summation of travel time by using the ray simulation result. Furthermore, by using those travel time data, the range-average current, the north-east current component could be calculated. Finally, the horizontal-slice inversion could be done by using tapered least-square accompanied with the L-

curve method to solve the 2nd order of Fourier Function method of the current velocities.

2. In Chapter 3, the range-average current results for every transmission line showed the characteristic of a tidal wave in Bali Strait is mix semidiurnal tides. The M2 and M8 oscillations peaked at the low water of SSH data and diminished around the high water. And the phase relation between SSH and current showed that potential energy from SSH variation served to generate not only M2 current, but also M8 current. Furthermore, the M8 oscillation is embedded in the envelope oscillation of the semidiurnal period. It provides a big possibility that the nonlinear interaction of semidiurnal and diurnal tides generated the M8 oscillation. However, the reason why the M8 component rather than M3, M4, and M6 was dominated is not found yet. Generally, the M8 overtide of period 3.17-hours is usually much weaker than M2 tide. The strong and highly variable 3-h oscillation, which occurs in the northern part of the Bali Strait and causes problems with ferry operation, was measured for the first time using a CAT array.

3. The characteristic of the strong current in the north of Bali Strait is mentioned in Chapter 4. The northward current more dominant, and clockwise and counter-clockwise vortex formed at the lateral side of Java Island when the northward current is strong in the central strait. The suggestion for a better ferry route to prevent and reduce ship accidents is shifted 10 km to the southern side of the experiment site.

5.2 Future Works

5.2.1 Three-dimensional Inversion

The more comprehensive inverse method of CAT could be done for further works is three-dimensional inversion. This inversion is combining horizontal-slice inversion with vertical-slice inversion [13]. The ray simulation result in Chapter 3 could be used for the vertical-slice inversion by applying Eq. (2.42), where the **E** matrix is filled with rays information. After the vertical-slice inversion are reconstructed for every transmission line, the Bali Strait case is four transmission lines. Every RACs result of the vertical-slice inversion is used to reconstruct the horizontal-slice inversion for every depth of the vertical-slice inversion layer. The inverted results from all the horizontal-slice inversions are pilled up to construct a 3D structure of current. The three-dimensional structure results could better understand the generation of the 3-hour oscillation in the tomography domain.

5.2.2 Data Assimilation

Kalman Filter was initially proposed by Kalman (1960) to simplify the Bayesian estimate for the linear model [61]. It is an efficient data assimilation (DA) method that can explicitly account for the dynamic propagation of errors in the linear model. The ensemble Kalman filter (EnKF) is a sequential data assimilation scheme that integrates observation data into a dynamical system obeying Kalman filter theory and Monte Carlo method [62, 63, 64, 65, 66]. This technique is the extended Kalman filter scheme which enables an application to nonlinear systems.

The differential travel time and the travel time summation that could be obtained using Eqs. (2.21) and (2.22), proportional to range-average current and sound speed, are CAT observation data to be assimilated into an ocean model. As a result,

the spatial resolution, which is a weak point in CAT measurement, is primarily improved through a dynamic interpolation for grids between the transmission lines. The DA could do forecasting the tidal current distribution in the ferry route of the Bali Strait. This forecasting model is useful for better ferry routes and schedules to avoid the disastrous current.

REFERENCES

[1] C. Wunsch, The Ocean Circulation Inverse Problem, Cambridge, New York: Cambridge University Press, 1996.

[2] H. Sagen, B. D. Dushaw, E. K. Skarsoulis, D. Dumont, M. A. Dzieciuch and A. Beszczynska-Moller, "Time series of temperature in Fram Strait determined from the 2008-2009 DAMOCLES acoustic tomography measurements and an ocean model," *Journal Geophysical Research,* vol. 121, pp. 4601-4617, 2016.

[3] L. H. Kantha and C. A. Clayson, Numerical Models of Oceans and Oceanic Processes, San Diego: Academic Press, 2000.

[4] G. Wust, "The major deep–sea expeditions and research vessels 1873–1960," *Progress in Oceanography,* vol. 2, pp. 3-52, 1964.

[5] R. H. Stewart, Introduction to Physical Oceanography, Tallahassee: Theorangegrove, 2008.

[6] A. O. D. Centre, "Oceanographic Instrumentation," Australian Oceanographic Data Centre , Potts Point N. S. W. , 2011.

[7] M. Tomzack and J. S. Godfrey, Regional Oceanography: An Introduction, Portland: Daya Publising House, 2003.

[8] AANDERAA, *Buoy Applications,* Bergen: Aanderaa Data Instruments, 2007.

[9] K. Aki and P. G. Richards, Quantitative Seismology: Theory and Methods, Freeman, 1980.

[10] W. Munk, P. Worcester and C. Wunsch, Ocean Acoustic Tomography, Cambridge, U.K.: Cambridge Univ. Press, 1995.

[11] W. Munk and C. Wunsch, "Ocean acoustic tomography: a scheme for large scale monitoring," *Deep Sea Research,* vol. 26A, pp. 123-161, 1979.

[12] T. O. T. Group, "A demonstration of ocean acoustic tomography," *Nature,* vol. 299, pp. 121-125, 1982.

[13] A. Kaneko, X.-H. Zhu and J. Lin, Coastal Acoustic Tomography, Cambridge: Elsevier, 2020.

[14] H. Sagen, B. D. Dushaw, E. K. Skarsoulis, D. Dumont, M. A. Dzieciuch and A. Beszczynka-Moller, "Time series of temperature in Fram Strait determined from the 2008-2009 DAMOCLES acoustic tomography measurements and an ocean model," *Journal of Geophysical Research,* vol. 121, pp. 4601-4617, 2016.

[15] B. D. Dushaw, H. Sagen and A. Beszczynska-Moller, "On the effects of small-scale variability on acoustic propagation in Fram Strait: The tomography forward problem," *Journal of Acoustic Society of America,* vol. 140, pp. 1286-1299, 2016.

[16] B. D. Dushaw and H. Sagen, "A comparative study of the properties of moored/point and acoustic tomography/integral observations of Fram Strait using objective mapping techniques," *Journal of Atmospheric and Oceanic Technology,* vol. 33, pp. 2079-2093, 2016.

[17] B. D. Dushaw, F. Gaillard and T. Terre, "Acoustic tomography in the Canary Basin: Meddies and tides," *Journal of Geophysical Research: Oceans,* vol. 122, pp. 8983-9003, 2017.

[18] H. Zheng, N. Gohda, H. Noguchi, T. Ito, H. Yamaoka, T. Tamura, Y. Takasugi and A. Kaneko, "Reciprocal sound transmission experiment for current measurement in the Seto Inland Sea," *Journal Oceanography,* vol. 53, pp. 117-127, 1997.

[19] H. Yamaoka, A. Kaneko, J.-H. Park, H. Zheng and N. Gohda, "Coastal acoustic tomography system and its field application," *IEEE Journal Oceanic Engineering,* vol. 27, no. 2, pp. 283-295, 2002.

[20] K. Yamaguchi, J. Lin, A. Kaneko, T. Yamamoto, N. Gohda and H.-Q. Nguyen, "A continuous mapping of tidal current structures in the Kanmon Strait," *Journal Oceanography,* vol. 61, no. 2, pp. 283-294, 2005.

[21] C.-Z. Zhang, A. Kaneko, X.-Z. Zhu and N. Gohda, "Tomographic mapping of a coastal upwelling and the associated diurnal internal tides in Hiroshima Bay, Japan," *Journal Geophysical Research,* vol. 120, no. 6, pp. 4288-4305, 2015.

[22] X.-H. Zhu, A. Kaneko, Q. Wu, C.-Z. Zhang, N. Taniguchi and N. Gohda, "Mapping tidal current structures in Zhitouyang Bay, China, using coastal acoustic tomography," *IEEE Journal Oceanic Engineering,* vol. 38, no. 2, pp. 285-296, 2013.

[23] F. Syamsudin, N. Taniguchi, C.-Z. Zhang, A. D. Hanifa, G. Li, M. Chen, H. Mutsuda, Z.-N. Zhu, X.-Z. Zhu, T. Nagai and A. Kaneko, "Observing internal solitary waves in

the Lombok Strait by coastal acoustic tomography," *Geophysical Research Letters,* 2019.

[24] A. D. Hanifa, F. Syamsudin, .. Zhang, H. Mutsuda, M. Chen, X.-H. Zhu, A. Kaneko, N. Taniguchi, G. Li, Z.-N. Zhu and N. Gohda, "Tomographic measurement of tidal current and associated 3-h oscillation in," *Estuarine, Coastal and Shelf Sciences,* vol. 236, 2020.

[25] F. Syamsudin, M. Chen, A. Kaneko, Y. Adityawarman, H. Zheng, H. Mutsuda, A. D. Hanifa, C.-Z. Zhang, G. Auger, J. C. Wells and X.-H. Zhu, "Profiling measurement of internal tides in Bali Strait by reciprocal sound transmission," *Acoustic Sciences and Technology,* vol. 38, no. 5, pp. 246-253, 2017.

[26] J. H. Park and A. Kaneko, "Assimilation of coastal acoustic tomography data into a barotropic ocean model," *Geophysical Research Letters,* vol. 27, pp. 3373-3376, 2000.

[27] X. H. Zhu, C. Z. Zhang, Q. S. Wu, A. Kaneko, X. P. Fan and B. Li, "Measuring discharge in a river with tidal bores by use of the coastal acoustic tomography system," *Estuarine, Coastal and Shelf Science,* Vols. 104-105, pp. 54-65, 2012.

[28] Y. Adityawarman, A. Kaneko, K. Nakano, N. Taniguchi, K. Komai, X. Guo and N. Gohda, "Reciprocal sound transmission experiment of mean current and temperature variations in the central part (Aki-nada) of the Seto Inland Sea, Japan," *Journal Oceanography,* vol. 67, no. 2, pp. 173-182, 2011.

[29] K. Kawanishi, A. Kaneko, S. Nigo, M. Soltani and M. F. Maghrebi, "New acoustic system for continuous measurement of river discharge and water temperature," *Water Science and Engineering,* vol. 3, no. 1, pp. 47-55, 2010.

[30] D. Berlianty and T. Yanagi, "Tide and tidal current in the Bali Strait, Indonesia," *Marine Research Indonesia,* vol. 36, no. 2, pp. 25-36, 2011.

[31] K. Matsumoto, M. Ooe and T. Sato, "Ocean tide model obtained from TOPEX/POSEIDON," *Journal of Geophysical Research,* vol. 100, pp. 25,319-25330, 1995.

[32] K. Matsumoto, T. Takanizawa and M. Ooe, "Ocean tide model developed by assimilating TOPEX/POSEIDON altimeter data into hydrodynamical model: A global model and a regional model around Japan," *Journal of Oceanography,* pp. 567-581, 2000.

[33] T. Yanagi, Coastal Oceanography, Tokyo: Terra Scientific Publishing Company, 1999.

[34] KNKT, "Laporan Investigasi Kecelakaan Pelayaran Tenggelamnya KMP. Rafelia 2," in *KNKT.16.03.02.03 (written in Indonesian Language)*, Jakarta, Indonesia, 2016.

[35] I. Rosidin, *5 Kasus Kecelakaan Kapal di Selat Bali, dari Rafelia 2 Tenggelam hingga Kapal Perang Terbakar (in Indonesian Language),* Banyuwangi, Indonesia: Kompas, 2021.

[36] M. Chen, F. Syamsudin, A. Kaneko, N. Gohda, B. M. Howe, H. Mutsuda, A. D. Hanifa, H. Zheng, C.-F. Huang, N. Taniguchi, X.-H. Zhu, Y. Adityawarman, C.-Z. Zhang and J. Lin, "Real-Time Offshore Coastal Acoustic Tomography Enabled With Mirror-Transpond Functionality," *IEEE Journal of Ocean Engineering,* vol. 45, no. 2, pp. 645-655, 2019.

[37] A. Pierce, Acoustics-An Introduction to Its Physical Principles and Application, New York: Acoustical Society of America, 1989.

[38] J.-H. Park and A. Kaneko, "Computer Simulation of Coastal Acoustic Tomography by a Two-Dimensional Vortex Model," *Journal of Oceanography,* vol. 57, pp. 593-602, 2001.

[39] P. C. Hansen, "Analysis of discrete ill-posed problems of the L-curve," *SIAM Review,* vol. 34, no. 4, pp. 561-580, 1992.

[40] P. C. Hansen and D. P. O'leary, "The use of the L-curve in the regularization of discrete ill-posed problems," *SIAM Journal Science Computation,* vol. 14, pp. 1487-1503, 1993.

[41] K. Yamaguchi, J. Lin, A. Kaneko, T. Yamamoto, N. Gohda, H.-Q. Nguyen and H. Zheng, "A continuous mapping of tidal current structures in the Kanmon Strait," *Journal of Oceanography,* vol. 61, no. 2, pp. 283-295, 2005.

[42] Y. Adityawarman and A. Kaneko, "Tidal current measurement in the Kurushima Strait by the reciprocal sound transmission method," *Acoustic Science and Technology,* vol. 33, pp. 45-51, 2012.

[43] A. Kaneko, K. Yamaguchi, T. Yamamoto, G. N., H. Zheng, F. Syamsudin, J. Lin, H.-Q. Nguyen, M. Matsuyama, H. Hachiya and N. Hashimoto, "A coastal acoustic tomography experiment in Tokyo Bay," *Acta Oceanologica Sinica,* vol. 24, pp. 86-94, 2005.

[44] J. Lin, A. Kaneko, N. Gohda and K. Yamaguchi, "Accurate imaging and prediction of Kanmon Strait tidal current structures by coastal acoustic tomography data," *Geophysical Research Letter,* vol. 32, p. LI4607, 2005.

[45] M. Chen, A. Kaneko, J. Lin and C. Zhang, "Mapping of a typhoon-driven coastal upwelling by assimilating coastal acoustic tomography data," *Journal of Geophysical Research Oceans,* vol. 122, pp. 7822-2837, 2017.

[46] Z.-N. Zhu, X.-Z. Zhu and X. Guo, "Coastal tomographic mapping of nonlinear tidal currents and residual currents," *Continental Shelf Research,* vol. 143, pp. 219-227, 2016.

[47] Z.-N. Zhu, X.-H. Zhu, X. Guo, X. Fan and C. Zhang, "Assimilation of coastal acoustic," *Journal of Geophysical Research Oceans ,* vol. 122, pp. 7013-7030, 2017.

[48] C. Zhang, X.-Z. Zhu, Z.-N. Zhu, W. Liu, Z.-Z. Zhang, X.-P. Fan, R.-X. Zhao, M.-H. Dong and M. Wang, "High-precision measurement of tidal current structures using coastal acoustic tomography," *Estuarine, Coastal and Shelf Science,* vol. 193, pp. 12-24, 2017.

[49] C.-F. Huang, Y.-W. Li and N. Taniguchi, "Mapping of ocean currents in shallow water using moving ship acoustic tomography," *Journal of the Acoustic Society of America,* vol. 145, no. 2, pp. 858-868, 2019.

[50] X.-H. Zhu, Z.-N. Zhu, X. Guo, Y.-L. Ma, X. Fan, M.-H. Dong and C. Zhang, "Measurement of tidal and residual currents and volume transport through the Qiongshou Strait using coastal acoustic tomography," *Continental Shelf Research,* vol. 108, pp. 65-75, 2015.

[51] U. Send, P. Worcester, B. Cornuelle, C. Tiemann and B. Bashcek, "Integral measurement of mass transport and heat content in the Strait of Gibraltar from acoustic transmission," *Deep-Sea Research Part II,* vol. 49, pp. 4069-4095, 2002.

[52] N. Taniguchi, A. Kaneko, Y. Yuan, N. Gohda, H. Chen, G. Liao, C. Yang, M. MInamidate, A. Yudi, X.-H. Zhu and J. Lin, "Long-term acoustic tomography measurement of ocean currents at the northern part of the Luzon Strait," *Geophysical Research Letter,* vol. 37, p. L07601, 2010.

[53] C. Zhang, A. Kaneko, X.-H. Zhu, B. M. Howe and N. Gohda, "Acoustic measurement of the net transport through the Seto Inland Sea," *Acoustic Science and Technology,* vol. 37, no. 1, pp. 10-20, 2016.

[54] M. K. Simon, J. K. Omura, R. A. Scholtz and B. K. Levin, Spread Spectrum Communications Handbook, McGraw-Hill, New York: New York Publisher, 1994.

[55] O. B. Andersen and G. D. Egbert, "Mapping nonlinear shallow-water tides: a look at the past and future," *Ocean Dynamics,* vol. 56, pp. 416-429, 2006.

[56] J. O. Blanton, G. Lin and S. A. Elston, "Tidal current asymmetry in shallow estuaries and tidal creeks," *Continental Shelf Research,* vol. 22, pp. 1731-1743, 2002.

[57] S. A. Thorpe, The Turbulent Ocean, Cambridge: Cambridge Univ. Press, 2005.

[58] A. Kaneko, G. Yuan, N. Gohda and I. Nakano, "Optimum design of the ocean acoustic tomography system for the Sea of Japan," *Journal of Oceanography,* vol. 50, pp. 281-293, 1994.

[59] A. D. Hanifa, H. Mutsuda, F. Syamsudin, M. Chen, Y. Doi and A. Kaneko, "Mapping tidal current fields around ferry route area in the Bali Strait by Coastal Acoustic Tomography," in *Proceeding of Workshop on Environmental Technologies in Naval Architecture and Ocean Engineering*, Hiroshima, 2018.

[60] A. D. Hanifa, H. Mutsuda, F. Syamsudin, N. Taniguchi, T. Nakashima, Y. Doi and A. Kaneko, "Spatiotemporal Measurement for Strong Current Fields in a Ferry Route Using Coastal Acoustic Tomography," in *Proceedings of the Thirtieth (2020) International Ocean and Polar Engineering Conference*, Shanghai, 2020.

[61] R. E. Kalman, "A new approach to linear filter and prediction problems," *Journal of Basic Engineering ,* vol. 32, pp. 32-45, 1960.

[62] G. Evensen, "Sequential data assimilation with a nonlinear quasi-geostrophic model using Monte Carlo methods to forecast error statistics," *Journal of Geophysical Research,* vol. 99, no. C5, pp. 10143-10-162, 1994.

[63] G. Evensen, "The ensemble Kalman filter: Theoretical formulation and practical implementation," *Ocean Dynamics,* vol. 53, no. 4, pp. 343-367, 2003.

[64] G. Evensen, "Sampling strategies and square root analysis schemes for the EnKF," *Ocean Dynamics,* vol. 54, pp. 539-560, 2004.

[65] G. Evensen, "The ensemble Kalman filter for combined state and parameter estimation," *IEEE Control Systems Magazine,* vol. 9, pp. 83-104, 2009.

[66] G. Evensen, Data Assimilation-The Ensemble Kalman Filter, Berlin: Springer, 2009.

ACKNOWLEDGMENT

I would like to express my best gratitude to my advisor, Prof. Hidemi Mutsuda who have been helping me in academic and also in settling down for Japan life in Hiroshima University. With his inspiration, curiosity, and enthusiasm, he provided valuable advice, ideas, and guidance for my research and helped me in the writing of this doctoral thesis. It is my honor being his student. I also wish to express my gratitude to Prof. Arata Kaneko as the developer of Coastal Acoustic Tomography (CAT), who provided the experiment, always patiently answered all my questions and taught me CAT, step by step. I also wish to express my gratitude to Dr. Fadli Syamsudin, Indonesian as the Agency for the Assessment and Application of Technology (BPPT), Indonesian government as the intermediator that I could study in Hiroshima University and helped me in my research.

I would like to express my gratitude to Prof. Iwashita as my second advisor for his valuable advice, sincere comments, and encouragement which help me a lot to finish this study. I also wish to express my gratitude to Asc. Prof. Yuji Sakuno as my third advisor for his valuable advice and sincere comments which help me a lot in this study. I would like to express my gratitude to Ast. Prof. Takuji Nakashima for his many advice, suggestions, and insightful discussions in my study.

My gratitude also extends to Dr. Naokazu Taniguchi, who gives me advice and insights for my research, and gave me a very big help for my experiment. And my appreciation to Iis Rochmawati as my senior lab, Ede M. Wardhana from Institut Teknologi Sepuluh Nopember (ITS) Surabaya, Sinrose Du, and other members of Fluid Dynamics for Vehicle and Environmental Systems Laboratory, Hiroshima University for their genuine help, support, and advice during my study. I am also thankful to all my Indonesian friends in Hiroshima for their support and contribution in my study and daily life in Japan. Finally, I warmly thank and appreciate my family, Ibu Wina, Abah Ferdy, my siblings, Salman, Fasya, Maryam, Angeliek Muller, Sofiatun Anisah, and many more closest friends that I could not mention for their great encouragement and support for me in pursuing the doctor's degree.